

Layered Surface Acoustic Wave Based Gas Sensors
Utilising
Nanostructured Indium Oxide Thin Layer

A thesis submitted in fulfilment of the requirements for the degree of
Doctor of Philosophy

Alexandru C. Fechete
B. Eng. (Hons)

School of Electrical and Computer Engineering
Science, Engineering and Technology Portfolio
RMIT University

May 2009

[This page has intentionally been left blank.]

Declaration

I certify that except where due acknowledgement has been made, the work is that of the author alone; the work has not been submitted previously, in whole or in part, to qualify for any other academic award; the content of the thesis is the result of work which has been carried out since the official commencement date of the approved research program; and, any editorial work, paid or unpaid, carried out by a third party is acknowledged.

Alexandru C. Fechete

07th May, 2009,

[This page has intentionally been left blank.]

“Man – strive and has faith - unfaltering faith.

“Ember, küzdj és bízva bizzál!”

(From the greatest Hungarian drama: “*The Tragedy of Man*” by Imre Madách)

[This page has intentionally been left blank.]

Acknowledgements

The most important person I would like to thank is my Mother who until the end of her life encouraged me to pursue further study and thought me never to give up.

I would like to thank also my senior supervisor Professor Wojtek Wlodarski for providing me with the opportunity to conduct this research work in the Sensor Technology Laboratory at RMIT University. His encouragement for me to pursue this research was pertinent to its completion. I would like especially thank my second supervisor Dr. Anthony Holland. His ever positive attitude and continuous support were most beneficial. He provided me with not only a lot of support and motivation during my research program but also genuine friendship.

I would like also to thank to Dr. Adrian Trinchì for his support during my studies. I would like also to show my appreciation to Dr. Kourosh Kalantar-zadeh and Dr. Kosmas Galatsis for their help and advice.

In particular I am extremely grateful for four of my former colleagues from the Sensor Technology Laboratory: Dr. Glenn I. Matthews for his help with the ozone generator, Dr. David A. Powell for his help with the simulation, Dr. Samuel J. Ippolito and Dr. Sasikaran Kandasamy for his help and advice.

Other colleagues I would like also to thank are Ms. Lilin Li, Ms. Rashidah Arsat, Ms. Joy Tan, Mr. Vijay Sivan, Dr. Bin Rong and Dr. Abu Z. Sadek for providing their feedback and friendship.

I would like to take this opportunity to thank several people, who provided me help during my studies. I am very grateful to Dr. Saulius Kaciulis and Dr. Luca Pandolfi of the CNR, Rome, Italy, for their extensive assistance in XPS analysis, to Dr. Jarek Antoszewski from University of Western Australia, Dr. Huang Hui and Professor Tim White from Nanyang University of Technology of Singapore and Dr. Anurat Wisitsorat from NECTEC, Thailand for the deposition of thin films for some of my samples.

I would like to thank the Cooperative Research Centre (CRC) for Microtechnology, Australia and for the School of Electrical and Computer Engineering of RMIT University for awarding me postgraduate scholarship.

My thanks extend to the academic and administrative members of the School of Electrical and Computer Engineering, headed by Professor Ian Burnett , former Head of School Professor Irena Cosic and Discipline Director Professor Alireza Baghai - Wadji, at RMIT University.

I am especially grateful to Microelectronic and Material Technology Centre staff of the school for their help. Special thanks to Mrs. Chi-Ping Wu, Mr. Paul Jones, and Mr. Yuxan Cao for their help in Clean Room fabrication procedures, to Mr. David Welch, Mr. Bob Kealy for their assistance with the ozone generator and gas chamber.

I would also like to take this opportunity to thank all my close friends who have supported me and helped me during my studies.

Alexandru C. Fechete

[This page has intentionally been left blank.]

Contents

Chapter 1.....	1
Introduction	1
1.1 Motivation.....	1
1.1.1 Layered SAW based Device for Gas Sensing Applications	8
1.2 Thesis Objectives	11
1.3 Author's Achievements	12
1.4 Thesis Organisation	16
Chapter 2.....	20
Literature Review and Research Rationale.....	20
2.1 Literature Review of SAW Based Devices.....	21
2.2 Literature Review of Semiconductor Metal Oxide Thin Films Pertaining to this Research.....	28
2.2.1 Literature Review of Indium Oxide Thin Films for Gas Sensing....	30
2.2.2 Literature Review of Tin Oxide Thin Films for Gas Sensing.....	31
2.3 Proposed Layered SAW Gas Sensor Structure.....	32
2.4 Summary	34
Chapter 3.....	35
Layered SAW Gas Sensor	35
3.1 Operation Principle of SAW Based Sensors.....	36
3.2 SAW Based Gas Sensors	37
3.2.1 Layered SAW Sensors	45
3.2.1.1 Determination of the Optimum Intermediate Layer Thickness.....	45
3.2.1.2 Gas Sensitive Layer Thickness and its Effect on the K^2 of the SAW Structure	51
3.3 SMO Gas Sensing Mechanism	57
3.4 Gas Sensitive Layer Morphology	63
3.4.1 Compact Layer.....	64

3.4.2 Porous Layer	65
3.5 Grain Size Effect on the Sensitivity of SMO Gas Sensors	66
3.5.1 Grain Size Effect on the Sensitivity of an Indium Oxide based Gas Sensor	69
3.6 Summary	71
Chapter 4.....	73
Layered SAW Gas Sensor Fabrication	73
4.1 SAW Transducer Fabrication Procedure	74
4.1.1 Sample Preparation	74
4.1.2 Thin Film Metal Evaporation	75
4.1.3 Photolithography	75
4.1.4 Chemical Etching	76
4.2 Intermediate and Sensitive Layers Deposition	78
4.2.1 R.f. Magnetron Sputtering Method	78
4.2.1.1 Intermediate Layer Deposition	81
4.2.1.2 Gas Sensitive Layer Deposition	83
4.2.2 Plasma Enhanced Chemical Vapour Deposition	84
4.2.2.1 Intermediate Layer Deposition	84
4.2.3 Electron Beam Evaporation	86
4.2.3.1 Intermediate Layer Deposition	87
4.2.4 Physical Vapour Deposition of 1-D InO _x Nanostructures	87
4.3 Layered SAW Sensor Frequency Response	89
4.4 Summary	90
Chapter 5.....	91
Gas Calibration System	91
5.1 Measurement Techniques	92
5.1.1 SAW Gas Sensor	92
5.1.2 Conductometric Sensor	94
5.2 Gas Sensor Measurement System	95
5.3 Summary	99
Chapter 6.....	100
Microstructural Characterisation of Sensors' Layers.....	100
6.1 Chemical Characterisation	102
6.1.1 X-Ray Photoelectron Spectroscopy (XPS)	102
6.1.1.1 Indium Oxide Sensitive Layer	105
6.1.1.2 Silicon Nitride Intermediate Layers	110
6.1.2 Discussion	114
6.2 Electron Concentration of the Indium Oxide Layers	116
6.3 Surface Morphology and Structural Characterisation	120
6.3.1 Scanning Electron Microscopy (SEM)	120
6.3.1.1 Planar Two-Dimensional (2-D) Nanostructures	121
6.3.1.2 One-Dimensional (1-D) Nanostructures	122
6.3.2 X-Ray Diffraction (XRD)	126
6.3.2.1 Planar 2-D InO _x layer	127
6.3.3 Discussion	130
6.3 Summary	131

Chapter 7.....	133
Results – Gas Sensing Performance	133
7.1 Layered SAW Sensors	134
7.1.1 Hydrogen Sensing Results	135
7.1.1.1 Sensor with PECVD Intermediate Layer (InO _x /SiO ₂ /SiN _x /36°YXLiTaO ₃).....	136
7.1.1.2 Sensor with a R.f. Sputtered Intermediate Layer (InO _x /SiN _x O _y /36°YXLiTaO ₃)	140
7.1.1.3 Sensor with E-beam Evaporated Intermediate Layer (InO _x /SiN _x /36°YXLiTaO ₃)	142
7.1.1.4 Comparative Analyses of the H ₂ Gas Sensing Results	144
7.1.2 Ozone Sensing Results.....	147
7.1.2.1 Sensor with PECVD Intermediate Layer (InO _x /SiO ₂ /SiN _x /36°YXLiTaO ₃).....	148
7.1.2.2 Sensor with R.f. Sputtered Intermediate Layer (InO _x /SiO _x N _y /36°YXLiTaO ₃)	151
7.1.2.3 Sensor with E-beam Evaporated Intermediate Layer (InO _x /SiN _x /36°YXLiTaO ₃)	152
7.1.2.4 Comparative Analyses of the O ₃ Gas Sensing Results	153
7.1.3 Discussion	155
7.2 Conductometric Sensor with SnO ₂ Nanorods Sensitive Layer.....	159
7.2.1 Discussion	160
7.3 Concluding Remarks.....	162
7.4 Summary	165
 Chapter 8.....	 168
Conclusions and Future Work.....	168
8.1 Conclusions.....	170
8.2 Suggestions for Further Work.....	172
 Appendix A	 174
SH-SAW Substrate Material Data	174
 Appendix B.....	 175
SH-SAW Propagation Characteristics.....	175
B.1 Stress and Strain in Non-piezoelectric Elastic Solid	176
B.2 Piezoelectric Interactions	178
B.3 SH-SAW (LSAW) Propagation.....	179
B.4 SH-SAW (LSAW) Generation	181
 Appendix C	 186
Material Constants.....	186
 Appendix D	 187
SAW Testing System.....	187

Appendix E..... 190
Static Performance Characteristics..... 190
Bibliography 192

List of Tables

Table 1.1	Analytical instruments and techniques for ozone concentration measurements: requirements and properties (modified from [18])	8
Table 3.1	Comparison of the calculated and measured sheet conductivity of the indium oxide sensitive layers of a SAW based gas sensor	57
Table 4.1	R.f. magnetron sputtering deposition parameters used for SiN _x layers	82
Table 4.3	PECVD parameters used for deposition of SiN _x layers.....	83
Table 4.4	PECVD parameters used for SnO ₂ nanorod thin layers.	85
Table 4.5	E-Beam evaporated deposition parameters used for the SiN _x layer	86
Table 5 1	Gas pulses and their concentrations used for testing the sensors	99
Table 6.1	Comparison of the r.f. sputtered InO _x thin layers before depth profiling	105

Table 6.2	XPS – Elemental composition of an InO _x layer deposited on r.f. magnetron sputtered SiN _x on a 36°YX LiTaO ₃ substrate showing the atomic percentage of the main elements before and after 60 minutes of etching.....	106
Table 6.3	XPS - Elemental composition of an r.f. magnetron sputtered InO _x film on 36°YX LiTaO ₃ substrate showing the atomic percentage of the main elements before and after 60 minutes of etching.	106
Table 6.4	Modified Auger parameters in (eV) for the indium oxide layers before and after 5 minutes of ion sputter etching	109
Table 6.5	Atomic percentage of the main elements with their corresponding binding energies in eV at different sputter etching time intervals for a sample with InO _x /PECVD SiN _x layers deposited on a 36°YX LiTaO ₃ substrate.	111
Table 6.6	XPS - Elemental composition of an r.f. magnetron sputtered SiN _x layer deposited on a 36°YX LiTaO ₃ substrate showing the atomic percentage of the main elements.	112
Table 6.7	XPS – Elemental composition before depth profiling of an E-Beam evaporated SiN _x film deposited on a 36°YX LiTaO ₃ substrate showing the atomic percentage of the main elements.....	113
Table 6.8	XPS results of the SiN _x layers before depth profiling. The layers were deposited on 36° YX LiTaO ₃ substrates and were utilised as intermediate layers for SAW based sensors.	115
Table 6.9	Calculated sheet resistance, resistivity and conductivity values of the deposited 100 nm InO _x layers	117
Table 6.10	Resistivity (ρ), conductivity (σ) and carrier concentrations of the doped and non-doped indium oxide films from the published literature [146-149]....	117

Table 6.11	Resistivity (ρ), conductivity (σ) and extrapolated carrier concentrations of the non-doped indium oxide films deposited on layered SAW devices.....	119
Table 6.12	Operating conditions of the GADDs.....	127
Table 7.1	Frequency shifts at three consecutive operational temperatures for the for the SAW sensors with the 1 μm and 2 μm PECVD SiN_x intermediate layer at different H_2 concentrations	138
Table 7.2	Summary of the H_2 sensing results for three layered SAW sensors with 1 μm thick intermediate layers.....	146
Table 7.3	Summary of the H_2 gas sensing results of a non-layered SAW sensor	146
Table.7.4	Summary of the O_3 gas sensing results of the layered SAW sensors	154
Table 7.5	Non-layered SAW based Gas Sensors (updated from [158]).....	162
Table 7.6	Layered SAW based Gas Sensors (updated from [158]).....	163
Table A. 1	Properties of piezoelectric Leaky SAWs.	174
Table C.1	Material constants	186

List of Figures

Figure 1.1	Cross section schematic of layered SAW sensor structure.....	12
Figure 2.1	Delay line SAW device (plan view)	22
Figure 2.2	Particle displacement for: (a1) Rayleigh SAW and (a2) SH-SAW (from [43]), Cross sectional view of the propagation of (b1) Rayleigh SAW and (b2) SH- SAW between the IDTs of a SAW device.....	23
Figure 2.3	Proposed novel layered SH-SAW structure.....	33
Figure 3.1	Variation of attenuation and relative change of acoustoelectric velocity versus $\log(\sigma_{sh} / \sigma_{or})$ of a sensitive layer	40
Figure 3.2	The electromechanical coupling coefficient (K^2) versus Si_3N_4 layer thickness: calculated for a periodicity of $\lambda = 24$ (μm) at the 36°YXLiTaO_3 substrate	47
Figure 3.3	Comparison of the electromechanical coupling coefficient (K^2) versus Si_3N_4 layer thickness: calculated for a periodicity of $\lambda = 24$ μm at the 36°YXLiTaO_3 substrate for two different silicon nitride material data.	50

Figure 3.4	Electromechanical coupling coefficient (K^2) changes versus In_2O_3 layer thickness for the $\text{In}_2\text{O}_3/1\mu\text{mSi}_3\text{N}_4/36^\circ\text{YXLiTaO}_3$ and $\text{In}_2\text{O}_3/1\mu\text{m PEVCD Si}_3\text{N}_4/36^\circ\text{YXLiTaO}_3$ structures	52
Figure 3.5	Electromechanical coupling coefficient (K_2) changes versus Si_3N_4 layer thickness of the $\text{Si}_3\text{N}_4/36^\circ\text{YXLiTaO}_3$ SAW structure with and without a 100 nm In_2O_3 gas sensitive layer	52
Figure 3.6	Electromechanical coupling coefficient (K^2) changes versus Si_3N_4 layer thickness for the PECVD $\text{Si}_3\text{N}_4/36^\circ\text{YXLiTaO}_3$ SAW structure with and without a 100 nm In_2O_3 sensing layer	53
Figure 3.7	Calculated change in frequency shift of a $\text{Si}_3\text{N}_4/36^\circ\text{YXLiTaO}_3$ SAW structure as a function of a sheet conductivity of the indium oxide sensitive layer	54
Figure 3.8	Variation of the sensitive 100 nm thin indium oxide layer sheet conductivity with the change of the intermediate layer thicknesses.....	56
Figure 3.9	Model of band bending in a semiconductor after chemisorption of oxygen on the surface sites	60
Figure 3.10	Structural and band model showing the intergranular contact regions for a polycrystalline semiconductor metal oxide in an: (a) relatively low oxygen concentration and (b) higher ambient oxygen concentration.....	61
Figure 3.11	Schematic cross-section views showing gas interaction in: (a) Compact and (b)Porous metal oxide layers	64
Figure 3.12	Schematic representation of a compact layer with energy band representations showing: (a) Partly depleted compact layer and (b) Completely depleted compact layer	65

Figure 3.13	Schematic representation of a porous layer showing geometry and surface energy band diagram for necks between grains: (a) represent a partly depleted neck and (b) is when the neck contact is completely depleted	66
Figure 3.14	Schematic representations of neck and grain boundary and resistance distribution	67
Figure 3.15	The effect of In_2O_3 thin film grain size on the In_2O_3 sensor response towards NO_2 (from [133])	70
Figure 3.16	The influence of film thickness on the ratio of main XRD peak intensities for an indium oxide film deposited by spray pyrolysis [119].....	71
Figure 3.17	The influence of the indium oxide film texture on the recovery time for ozone sensing [119]	71
Figure 4.1	Orientation of a 36°YX LiTaO_3 wafer and two SAW delay line devices.....	76
Figure 4.2	Photolithography steps for IDT patterning	77
Figure 4.3	Two port delay line SAW device used in this research work: (a) magnified photograph comparing the delay line SAW device with a 5 cent Australian coin, (b) Schematic of the device with dimensions.	78
Figure 4.4	Schematic diagram of the r.f. planar magnetron sputtering system used	81
Figure 4.5	Schematic of the experimental apparatus used for the growth of InO_x nanostructures	88
Figure 4.6	Frequency response of a $\text{InO}_x/\text{SiN}_x/36^\circ\text{YXLiTaO}_3$ SAW sensor at three stages of fabrication process	89
Figure 5.1	Basic schematic of an oscillator for measuring the SAW device	92

Figure 5.2	Diagram of the multi-channel gas calibration system setup	96
Figure 5.3	Custom built teflon chamber and RF amplifier assembly from [29]	97
Figure 5.4	Heaters used for testing with : (a) sapphire and (b) alumina substrate	98
Figure 6.1	XPS depth profile of $\text{InO}_x/\text{SiN}_x$ layers deposited by r.f. magnetron sputtering on a $36^\circ\text{YX LiTaO}_3$ substrate	107
Figure 6.2	XPS depth profile of an r.f. magnetron sputtered InO_x layer on a $36^\circ\text{YX LiTaO}_3$ substrate	108
Figure 6.3	XPS spectra of the $\text{In}_{3d5/2}$ and $\text{In}_{3d3/2}$ peaks registered after different sputtering time intervals (t_s)	108
Figure 6.4	XPS depth profile of an r.f. magnetron sputtered InO_x layer on PECVD SiN_x layer on a $36^\circ\text{YX LiTaO}_3$ substrate	110
Figure 6.5	XPS depth profile of an r.f. magnetron sputtered SiN_x layer on $36^\circ\text{YX LiTaO}_3$ substrate	112
Figure 6.6	Extrapolation methods used to determine the carrier concentration of the non-doped indium oxide films deposited on the layered SAW devices	118
Figure 6.7	SEM micrographs of an r.f. magnetron sputtered InO_x layer on LiTaO_3 substrate: (a) top view and (b) cross-sectional view of this layer	121
Figure 6.8	FE-SEM micrographs of a polycrystalline InO_x thin film with (a) uniform distribution of the nanosized crystallites and (b) in some parts agglomerations of crystallites occurred	122
Figure 6.9	FEG-SEM micrographs of SnO_2 nanorods deposited on: (a) SAW transducer IDT and (b) a $36^\circ\text{YX LiTaO}_3$ substrate	125

Figure 6.10	Bright field HRTEM image of a cluster of SnO ₂ nanorods	125
Figure 6.11	TEM lattice image and Fourier reconstructed diffraction pattern of the SnO ₂ nanorods on a LiTaO ₃ substrate	126
Figure 6.12	XRD diffractograms of as-deposited r.f. magnetron sputtered and annealed InO _x layers 36° YX LiTaO ₃ substrate.	129
Figure 6.13	XRD diffractogram of the r.f. magnetron sputtered InO _x thin film on a silicon substrate	129
Figure 7.1	Dynamic responses of layered SAW sensors with 1 μm and 2 μm intermediate layers towards a sequence of pulses between 0.06% and 1.0% H ₂ in synthetic air at 290°C.....	136
Figure 7.2	Frequency shift versus operational temperature for a layered SAW sensor with: (a) 1 μm and (b) 2 μm thick PECVD SiN _x intermediate layer.....	137
Figure 7.3	Hydrogen gas concentrations v. frequency shift for the layered SAW sensors with 1 and 2 μm PECVD SiN _x at 290°C	139
Figure 7.4	Frequency shift versus operational temperature of the layered SAW sensors with PECVD SiN _x intermediate layers for 1.00% H ₂ concentrations in synthetic air.....	140
Figure 7.5	Frequency shift versus operating temperature for the layered SAW sensor with 1 μm r.f. magnetron sputtered intermediate layer	141
Figure 7.6	Dynamic response of the SAW sensor with r.f. magnetron sputtered intermediate layer towards a H ₂ pulse sequence at different operational temperatures at: (a) 240 °C, (b) 215°C and (c) 190°C.....	142
Figure 7.7	Frequency shift versus operational temperature for layered SAW sensor with E-beam evaporated 1 μm SiN _x intermediate layer	143

Figure 7.8	Dynamic response of the layered SAW sensor with E-beam evaporated 1 μm SiN_x intermediate layer towards a sequence of H_2 pulse at 290°C	143
Figure 7.9	Dynamic response of a layered SAW sensor when it is exposed towards an oxidizing gas (O_3)	148
Figure 7.10	Frequency shift versus operational temperature for the layered SAW sensor with a PECVD SiN_x intermediate layer, towards different O_3 concentrations.....	149
Figure 7.11	Dynamic response of a layered SAW sensor with a PEVCD SiN_x intermediate layer, towards O_3 at two different operational temperatures at: (a) 195°C and (b) 220°C	150
Figure 7.12	Frequency response of a SAW sensor (red line) showing the influences caused by the Triple Transient Echo (TTR).....	150
Figure 7.13	Frequency shift versus operational temperature for the layered SAW sensor, with r.f. magnetron sputtered intermediate layer, for two different O_3 concentrations.....	151
Figure 7.14	Dynamic response of a layered SAW sensor with a r.f. magnetron sputtered intermediate layer, towards O_3 at two operational temperatures: (a) 195°C and (b) 190°C	152
Figure 7.15	Frequency shift versus operational temperature for the layered SAW sensor with E-beam evaporated intermediate layer towards two different O_3 concentrations.....	153
Figure 7.16	Dynamic response of a layered SAW sensor with E-beam intermediate layer towards O_3 at two operational temperatures: (a) 215°C and (b) 240°C	153
Figure 7.17	Dynamic responses for the conductometric sensor at 280°C towards: (a) oxidizing (NO_2) and (b) reducing (CO) gas.....	159

Figure B. 1	SH-SAW propagating along the X-axis and rotated by about θ the Y-axis	180
Figure B. 2	Delay line SH-SAW device composed of an input and output IDT formed by metal electrodes patterned on a piezoelectric crystal: (a) Top view and (b) Side view, (redrawn and modified from [104])	182
Figure B. 3	Frequency response of a SAW delay line can be approximated to a sinc(X) function, where is the centre frequency [177]	185
Figure D.1	Three stage R.F. amplifier schematic (from [29]).	188
Figure D.2	R.F. amplifier printed circuit board (from [29])	188
Figure D.3	Comparison of the simulated and measured S_{21} parameter of the amplifier	189

[This page has intentionally been left blank.]

Abstract

Planar two-dimensional (2-D) nanostructured indium oxide (InO_x) and one-dimensional (1-D) tin oxide (SnO_2) semiconductor metal-oxide layers have been utilised for gas sensing applications. Novel layered Surface Acoustic Wave (SAW) based sensors were developed consisting of $\text{InO}_x/\text{SiO}_x\text{N}_y/36^\circ\text{YXLiTaO}_3$, $\text{InO}_x/\text{SiN}_x/\text{SiO}_2/36^\circ\text{YXLiTaO}_3$ and $\text{InO}_x/\text{SiN}_x/36^\circ\text{YXLiTaO}_3$ structures. The 1 μm intermediate layers of silicon oxynitride (SiO_xN_y), silicon nitride (SiN_x) and $\text{SiO}_2/\text{SiN}_x$ matrix were deposited on lithium tantalate (36°YXLiTaO_3) substrates by r.f. magnetron sputtering, electron-beam evaporation and plasma enhanced chemical vapour deposition (PECVD) techniques, respectively. As a gas sensitive layer, a 100 nm thin layer of InO_x was deposited on the intermediate layers by r.f. magnetron sputtering. The targeted gases were ozone (O_3) and hydrogen (H_2). An intermediate layer has multiple functions: protective role for the interdigital transducers' electrodes as well as an isolating effect from InO_x sensing layer, thereby improving the sensor performance. The developed SAW sensors' exhibited high response magnitudes with repeatable, reversible and stable responses towards O_3 and H_2 . They are capable of sensing concentrations as low as 20 parts-per-billion for O_3 and 600 parts-per-million for H_2 . Additionally a conductometric type novel sensing structure of $\text{SnO}_2/36^\circ\text{YX LiTaO}_3$ was also

developed by depositing a thin layer of SnO₂ nanorods by PECVD. The gas sensing performance exhibited repeatable, reversible, stable responses towards NO₂ and CO. The surface morphology, crystalline structure and preferred orientation of the deposited layers were investigated by Scanning Electron Microscopy (SEM) and X-ray Diffraction (XRD). A polycrystalline, oxygen deficient non-stoichiometric InO_x with grain sizes of 20-40 nm was revealed. The 1-D nanostructures were characterised by Transmission Electron Microscopy (TEM) showing nanorods with needle-like shape, diameters of 10-20 nm at the top and 30-40 nm at the base as well as a preferential growth orientation of $[10\bar{1}]$ on the LiTaO₃ substrate. The developed sensors are promising for O₃, H₂ and CO sensing.

Chapter 1

Introduction

1.1 Motivation

Due to ever increasing industrial activity, the air in the earth's atmosphere has become polluted and is rapidly deteriorating [1]. There are a variety of air pollutants with well known harmful effects on human health, the environment and climate; such as sulphur dioxide (SO_2), nitrogen dioxide (NO_2), oxides of carbon (CO_x), hydrocarbons, volatile organic compounds (VOCs) and ozone (O_3). These pollutants are produced by industrial and domestic sources; however today in both developed and developing countries one of the main threats to clean air is posed by motor vehicle traffic emissions [2]. These emissions contain a wide variety of contaminants, mainly CO, oxides of nitrogen (NO_x) and VOCs, which have an increasing negative impact on urban air quality [3]. Furthermore, photochemical reactions resulting from

the reaction of sunlight on NO_2 and VOCs emitted from vehicles leads to the formation of ground level O_3 , which has an impact in areas often far from the original emission site.

All these air pollutants present tremendous health risks, e.g. the World Health Organisation (WHO) estimates that 4.6 million people die each year from causes directly linked to air pollution [4]. Therefore, due to the rapid increase in environmental pollution there is a growing demand for highly sensitive, cheap, user-friendly devices to monitor the air quality in indoor and outdoor areas in order to protect the health of human beings.

Analytical instruments, such as mass spectrometers, provide the most precise form of monitoring of gases. Although they are accurate and sensitive, they are also bulky, expensive and require highly trained personnel for proper operation as well as for data interpretation. A significant disadvantage of these systems is that they are generally located in laboratories, where specific samples are brought for analyses, rendering such instruments impractical for in-situ outdoor multi-spot measurements. Therefore intense research efforts have been carried out on novel sensors that are capable of overcoming the abovementioned shortcomings.

Solid-state devices have been widely employed as a practical solution for sensing. They are compact, have a small size, can be produced relatively inexpensively, and are capable of monitoring analyte gas concentrations in the parts per million (ppm) or parts per billion (ppb) ranges. Their main advantage is that they can be easily interfaced with electronics, making them battery-operated and portable devices for multi-spot monitoring. However they have traditionally suffered from limited measurement accuracy and problems of long-term stability.

The two most commonly encountered solid state gas sensors are Metal Oxide Semiconductor (MOS) devices and Semiconductor Metal Oxide (SMO) based sensors. MOS based sensors

include Field Effect Transistors (FETs) and Schottky diodes. They are small, measuring less than a few mm^2 and generally consist of a thin catalytic layer (e.g. platinum or palladium) deposited on an insulating oxide layer (e.g. silicon dioxide) and the substrate in most cases is silicon (Si) [5]. These sensors are very stable and can be made sensitive to a broad range of gases. Recently, MOS devices based on silicon carbide (SiC) substrates have enabled them to perform sensing measurements at high temperatures (in excess of 500°C) [6]. SMO based gas sensors work by measuring changes in the electrical conductivity of the semiconducting material. Analyte gas molecules may chemisorb on the surface of the SMO thin film, resulting in changes in the film's electrical conductivity that can be correlated to the concentration of the analyte [7]. Such sensors are called conductometric or chemiresistors.

Since the development of tin oxide (SnO_2) based sensors in 1962 by Seiyama [8], many other SMO based gas sensors have been developed for air quality monitoring, automotive, medical and industrial applications utilizing materials such as zinc oxide (ZnO), tungsten trioxide (WO_3) and titanium dioxide (TiO_2) as gas sensitive layers. Indium oxide (In_2O_3 or InO_x in non-stoichiometric form) was reported for the first time in an O_3 sensing application in 1993 by Takada [9]. Soon after, an O_3 conductometric sensor became commercially available through New Electric Cosmos Co. Ltd. Although in the last four decades considerable progress has been made in the development of SMO based gas sensors there is still intense research activity being undertaken currently worldwide to improve the sensitivity, long-range stability and selectivity of these devices. Research is also being undertaken to reduce the power consumption of such sensors in order to realise portable instruments for outdoor measurements.

Along with the above mentioned types of sensors, acoustic wave based devices were also developed. These types of sensors include the quartz crystal microbalance (QCM), thin film

resonators (TFRs) as well as surface acoustic wave (SAW) based devices. In the last two decades the application of SAW based devices for gas sensing has increased greatly [10] as these proved to be an efficient and economically feasible alternative for the measurement of different gas concentrations. A SAW based gas sensor usually utilizes a semiconductor metal oxide as a gas sensitive layer deposited over the top of a SAW transducer. The analyte gas species that becomes chemisorbed on the surface of this gas sensitive layer induces either a change in the electrical conductivity of the gas sensitive layer or the mass of the layer. SAW devices are capable of responding to either mechanical or electrical perturbations at their surface arising from the adsorption of gas molecules. A SAW device that responds to electrical perturbations is referred to as a conductometric SAW [11].

This thesis is mainly concerned with the development of a novel layered conductometric SAW based gas sensors. Before the structure and distinctive advantages of this type of sensor are outlined, an introduction to ozone, nitrogen dioxide, carbon monoxide and hydrogen will be presented, as these common pollutant gases were used to test the fabricated novel sensors.

Ozone (O_3) is known to be highly reactive and a major toxic pollutant with considerable health risks [12]. The ozone molecule contains three oxygen atoms (O_3) and is highly unstable, reacting with many other substances. It occurs naturally in the earth's atmosphere, with 90% of this in the stratosphere (altitude of 12 to 50 km), formed by the action of ultraviolet light emitted by the sun on oxygen molecules. This naturally occurring high-level ozone, called "*good ozone*" forms a shield that prevents the penetration of ultraviolet radiation, which causes biological damage (e.g. skin cancer). The release of man-made chemicals such as chlorofluorocarbons (CFCs), halocarbons and other substances used in extinguishers, solvents and coolants have depleted this ozone layer. This has led to a hole in

the ozone layer over the earth's poles. The other 10% of ozone is found in the troposphere (earth's surface to 12 km up), called "*bad ozone*", formed mainly from hydrocarbons and nitrogen oxides released by motor vehicles and industrial processes [12].

The ozone formed at ground level can cause different health problems such as chest pains, coughing, wheezing, and shortness of breath [13]. Moreover, recent (2005) epidemiological studies have provided evidence that short-term exposure to high ozone concentration causes severe health problems (possibly life-threatening) and experimental evidence confirmed a long-term damaging effect on people's lungs [14].

These findings are particularly important as previously it was known that ozone is harmful but was not linked to mortality. In view of these studies the U.S. Environmental Protection Agency (EPA) is presently reviewing its standards for ozone levels. The U.S National Ambient Air Quality Standard (NAAQS) states that ground ozone levels must not exceed 75 ppb (effective from May 27, 2008) for an averaging time of 8 hours (this is based on the 4th highest measurement annually, averaged over 3 consecutive years) [15]. Furthermore an "Ozone Regulation Assembly Bill" was approved in 2006 to develop and adopt a regulation until the end of 2008 to limit the ozone emitted from indoor air cleaning devices in order to protect public health [16]. The WHO also concluded (based on these epidemiological studies) that there is sufficient evidence to reconsider its air quality guidelines (AQG) for O₃ and the previously recommended limit, which was fixed at 120 µg/m³, has been reduced to 100 µg/m³ (50 ppb). This is based on controlled human exposure studies, for a maximum duration of 8-hours [17].

Table 1.1 Analytical instruments and techniques for ozone concentration measurements: requirements and properties (modified from [18])

Analytical Techniques and Instruments	UV Spectrometer	Chemi-luminescence Spectrometer	Fluorescence Technique	Chemical Analysis	Mass Spectrometry
Measurement Principle	photometry	chemiluminescence of organic alkenes, alkanes and pigment	fluorescence quenching method	liberation of iodine	deflection in electric and magnetic field
Operational area	in air at room temperature, and in atmosphere	in air at room temperature, and in atmosphere	atmospheric measurements	atmospheric and near-ground level measurements	in higher atmosphere and in laboratory
Sensing range	up to $1962 \mu\text{g} / \text{m}^3$	up to $4000 \mu\text{g} / \text{m}^3$	$0.5 \mu\text{g} / 25 \text{ ml}$	n/a	n/a
Sensing limit	$1.96 \mu\text{g} / \text{m}^3$	$\sim 6 \mu\text{g} / \text{m}^3$	$0.01 \mu\text{g} / 25 \text{ ml}$	$\sim 2 \mu\text{g} / \text{m}^3$	n/a
Advantages	no cross - sensitivities to NO_2 and SO_2 , possible to miniaturize	highly sensitive (1 ppb) no cross-sensitivities to other gases	highly sensitive and selective, no cross-sensitivities to NO, rapid determination	simple, cheap	highly sensitive and selective
Disadvantages	high cost, high cross-sensitivities to organic compound	high cost, complex calibration	necessity of bromine for calibration	insufficient sensitivity to ozone	high cost , complex , limited to laboratory
References	[19]	[20]	[21]	[22]	[23]

Considering these new requirements there is an urgent need to measure O_3 concentrations at low ppb levels. Analytical instruments have been used for O_3 measurements (listed in Table 1 above, modified from [18]) but are not suitable for outdoor multispot measurement. These instruments are expensive, are not portable and properly qualified personnel is needed for operation and interpretation of the obtained data. Therefore there is a demand for a cheap, user-friendly, highly sensitive ozone sensor which is capable of measuring concentrations in

the low ppb range and that can be integrated in portable devices for outdoor multispot measurements.

Nitrogen Oxide (NO₂), a reddish-brown gas, has a characteristic sharp, biting odour and is one of the most prominent air pollutants [3]. In the lower atmosphere, oxides of nitrogen play a major role in the formation of photochemical smog in a complex set of reactions resulting in the formation of excessive levels of ozone. Industrial and motor vehicles are the main source of emissions. Adsorption through the skin or by dissolution of nitrogen dioxide in moist surfaces such as the eyes and mouth can cause fatigue, gastric upset or even pulmonary oedema [24], so there is a great demand for NO₂ gas sensors for motor vehicle engine exhaust control and environmental monitoring.

Carbon Monoxide (CO) is a colourless, odourless, and tasteless gas. A significant source of CO is from the incomplete combustion of carbon-containing compounds, notably in internal-combustion engines. It is present in the exhaust gas of motor vehicle engines and it is regarded as the most common cause for poisoning in residential homes and personnel in industry [25]. Therefore there is a stringent need for gas sensors for the detection of low concentrations of CO.

Hydrogen (H₂) is a colourless, odourless *non-polluting gas*; but it has numerous industrial applications and has the potential to be used as a clean source of energy. Hydrogen gas is highly flammable and will burn at concentrations as low as 4% H₂ in air [26]. Hydrogen gas may be explosive when mixed with oxygen. The flames are nearly invisible, so it is difficult visually to detect if a hydrogen leak is burning. Therefore there is a huge demand for highly

sensitive devices for precise monitoring of hydrogen gas concentrations in applications such as fire warning systems, leak detection and monitoring of industrial process control systems.

1.1.1 Layered SAW based Device for Gas Sensing Applications

SAW based devices provide a highly sensitive approach for gas sensing. They are efficient, practical alternatives for the sensing of different gas concentrations and present distinctive advantages in comparison with other types of sensors [27]:

- they have a small planar structure which simplifies the deposition of gas sensitive layers
- they have reproducible device performance characteristics controlled by photolithographic mask designs
- they have a direct frequency output and therefore are very convenient for remote sensing
- they can have operating frequencies up to the low gigahertz range
- they can be easily fabricated at low cost
- they have low power consumption and therefore can be used as portable devices when interfaced with electronics

A SAW gas sensor consists of a piezoelectric crystal substrate on which metal electrodes (interdigital transducers - IDTs) are fabricated by conventional photolithography techniques. For specific crystal orientations in many piezoelectric substrates the propagation of surface acoustic waves are confined to the surface within one or two wavelengths. This confinement of energy makes them highly sensitive to surface perturbations. Layers of Semiconductor Metal Oxide (SMO) films with different chemical compositions and thicknesses are deposited

upon the substrate material. The SMO is chosen to be sensitive to the targeted gas analytes. The interaction of the gas molecules with the sensitive SMO layer affects the propagation of the acoustic wave between the transmitting and receiving transducers. This can be measured as an incremental change in frequency of oscillation when the SAW sensor is connected to an RF amplifier in an oscillator configuration. SMOs can be oxidised or reduced upon exposure to different gases and when the SAW device is exposed to a gas, a change in the conductivity of the metal oxide layer occurs. This will result in a change of its operational frequency, which can be correlated to the gas concentration.

The sensitivity of a SAW sensor can be further enhanced by employing a nanostructured thin film as a gas sensitive layer due to the increased surface-to-volume ratio for gas molecules in such a layer [28]. By adding an intermediate layer between the substrate and the gas sensitive layer the SAW device performance is improved [29] resulting in a number of advantages over its non-layered counterparts [29, 30]. These advantages are:

- the intermediate layer has an isolating effect against the capacitive and conductive loading of the sensitive semiconductor metal oxide layer
- the intermediate layer deposited over the IDTs has a protective role against the surrounding environment increasing the long term stability of the SAW device
- an intermediate layer will electrically shield the metal electrodes from the gas sensitive layer making it possible to deposit this layer onto the entire surface of the device and as a result the response magnitudes will be increased

In this thesis the term “layered” has been used for the SAW devices where an intermediate layer has been added between the substrate and gas sensitive layer. The term conductometric SAW sensor has been used for a SAW device whose operation principle is based on the change of conductivity of the sensitive layer which causes a change in the measured oscillation frequency. Figure 1.1 shows a cross-section schematic of a layered SAW structure.

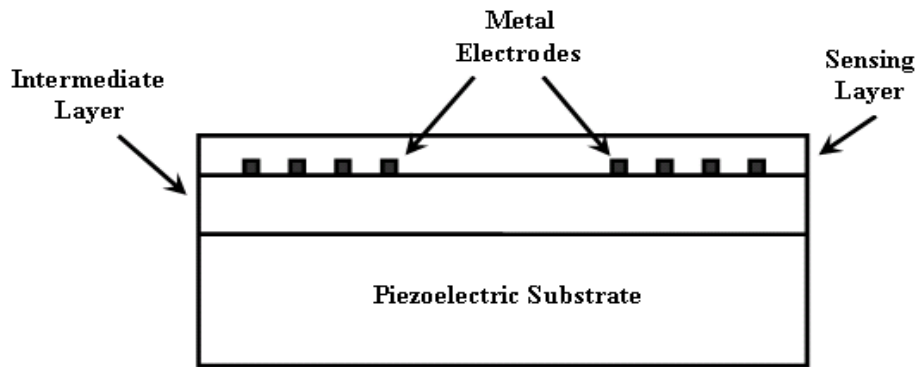


Figure 1.1 Cross section schematic of layered SAW sensor structure

The development of layered SAW devices with a nanostructured SMO thin film sensing layer as well as using as an intermediate layer appears to be a very promising alternative over other SMO device structures. Employing a layered SAW device satisfies the rigorous requirements necessary for a modern gas sensing device (e.g. easy-to-use, portable, cheap, stable, low power consumption) to monitor the quality of air and to provide safety protection.

The author has chosen to utilise a nanostructured indium oxide thin film as a gas sensitive layer (this material is one of the most sensitive materials reported towards O_3 [31]) and a 36° rotated Y-cut X-propagating lithium tantalite ($LiTaO_3$) piezoelectric substrate which presents advantages such as: relatively high electromechanical coupling and low temperature coefficient of delay. As an intermediate layer, silicon nitride was selected.

Silicon Nitride (Si_3N_4 or SiN_x in non-stoichiometric form) presents several distinctive advantages: it is an inert and passive material, has high-wear resistance and lower propagation loss than the materials used previously (e.g. silicon dioxide or zinc oxide) and is a common material in semiconductor material fabrication [32]. The rationale for the selection of these materials and substrate is discussed in the following chapter.

One-dimensional (1-D) nanostructures of semiconductor metal oxides such as nanorods, nanowires and nanobelts have recently attracted much attention for their potential applications in electronics and sensors [33]. The author has also investigated the application of a SnO_2 nanorod gas sensitive layer deposited on a LiTaO_3 substrate for CO and NO_2 sensing.

1.2 Thesis Objectives

The objectives of this research are to develop novel layered SAW based O_3 and H_2 sensors using nanostructured InO_x thin films and to investigate their gas sensing performance and sensing mechanism. To achieve the above, the research conducted had the following steps:

- fabricated SAW transducers on LiTaO_3 substrates, determined suitable deposition parameters for the intermediate and the gas sensitive layers
- performed structural and chemical characterisation in order to examine the material properties of the intermediate and sensitive layers using appropriate analytical methods : X-Ray Diffraction (XRD) , X-ray Photoelectron Spectroscopy (XPS), Scanning Electron Microscopy (SEM) and Transmission Electron Microscopy (TEM) techniques
- investigated the gas sensors performance to explain their gas sensing mechanism

1.3 Author's Achievements

There have been several significant outcomes from this research program which have contributed to the field of gas sensors. The most important achievement is the development of novel layered SAW based O_3 and H_2 sensors, as well as the application of SnO_2 nanorod layer in a conductometric sensor for CO and NO_2 detection.

The author's achievements are summarised below:

- three deposition techniques: r.f. magnetron sputtering, Electron-Beam evaporation and Plasma Enhanced Chemical Deposition (PEVCD) were employed to deposit intermediate layers with different thicknesses. Layers obtained were composed of both (i) silicon nitride (SiN_x), (ii) silicon oxynitride (SiO_xN_y) or (iii) an intermediate layer composed of two films, silicon oxide and silicon nitride (SiO_2/SiN_x). R.f. magnetron sputtering was employed for the InO_x sensing layer deposition; films with nanosized grains (less than 50 nm) were deposited.
- novel layered SAW O_3 and H_2 sensors with $InO_x/SiN_x/36^\circ YLiTaO_3$, $InO_x/SiO_2/SiN_x/36^\circ YLiTaO_3$ and $InO_x/SiO_xN_y/36^\circ YLiTaO_3$ structures, in particular for sensing O_3 concentrations in the low ppb range (~ 20 ppb) were developed. The sensors presented very stable, reversible and reproducible responses and were also capable of sensing H_2 concentrations as low as 600 ppm.
- microstructural characterisation was performed using SEM, Field Emission (FE) SEM, XRD and XPS techniques. These revealed that the InO_x thin films have promising gas sensing material properties (e.g. non-stoichiometric films with

oriented polycrystalline structure and nanosized grains between 20 and 40 nm in diameter)

- application of SnO₂ nanorod gas sensitive layer on a LiTaO₃ substrate for NO₂ and CO sensing in a conductometric sensor. The SnO₂ nanorods are single crystals, with diameters of 10 to 20 nm at the tip and 20 to 40 nm at the base. The TEM Fourier reconstructed diffraction pattern showed a preferential orientation for these nanorods formed on a LiTaO₃ substrate.

This research program successfully fulfilled its objectives in developing novel layered SAW based sensors for sensing low concentration of O₃ and H₂. Additionally a novel conductometric sensor was developed by employing a 1-D nanostructured gas sensitive layer on a LiTaO₃ substrate.

To the best knowledge of the author, SAW based sensors with an InO_x/SiN_x/36°YXLiTaO₃, InO_x/SiO₂/SiN_x/36°YXLiTaO₃ or InO_x/SiO_xN_y/36°YXLiTaO₃ structure have not been previously reported in the literature and neither has a conductometric sensor with a SnO₂ nanorod layer deposited on a LiTaO₃ substrate.

The results of these achievements have been published in refereed journals and conference proceeding, which are listed below.

List of author's publications

A. Refereed Journal Articles

1. **A. C. Fechete**, W. Wlodarski, K. Kalantar-Zadeh, A. S. Holland, J. Antoszewski, S. Kaciulis and L. Pandolfi, "SAW-based Gas Sensors with r.f. Sputtered InO_x and PECVD SiN_x Films: Response to H_2 and O_3 Gases", *Sensors and Actuators B: Chemical*, vol. 118, pp. 362-367, 2006.
2. **A. C. Fechete**, A. Wisitsora-at, L. L. Lin, W. Wlodarski, K. Kalantar-zadeh and A. S. Holland, "Hydrogen and Ozone SAW based Gas Sensors with RF Magnetron Sputtered InO_x and Electron Beam Evaporated SiN_x ", *Journal of Rare Metal Materials and Engineering*, vol. 35, pp.206-210, 2005.
3. **A. C. Fechete**, S. J. Ippolito, K. Kalantar-zadeh, W. Wlodarski, A. S. Holland and A. Wisitsora-at, "Layered $36^\circ\text{YXLiTaO}_3/\text{Si}_3\text{N}_4/\text{In}_2\text{O}_3$ Surface Acoustic Wave Based Hydrogen Sensor", *Chiang Mai Journal of Science*, vol.32, pp. 465-470, 2005.

B. Refereed Conference Papers

1. **A. C. Fechete**, W. Wlodarski, K. Kalantar-zadeh, A. S. Holland, J. Antoszewski, S. Kaciulis and L. Pandolfi, "Comparative Study of Surface Acoustic Wave Based Hydrogen Sensors with: $\text{InO}_x/\text{SiN}_x/36^\circ\text{YXLiTaO}_3$ Structure", *SPIE*, vol. 6035, pp. 603517, 2006.
2. **A. C. Fechete**, S. J. Ippolito, K. Kalantar-zadeh, W. Wlodarski and A. S. Holland, "Surface Acoustic Wave based Ozone Sensor with a $\text{InO}_x/\text{Si}_3\text{N}_4/36^\circ\text{YXLiTaO}_3$ structure", *SPIE* vol. 5650, pp. 268-275, 2005.

3. **A. C. Fechete** , W. Wlodarski, K. Kalantar-zadeh, A. S. Holland and A. Wisistsora-at, “Ozone Sensors based on Layered SAW Devices with $36^\circ\text{YXLiTaO}_3/\text{SiN}_x/\text{InO}_x$ structure”, Proceedings of IEEE TENCON , Melbourne 21-23 November, 2005.

C. Other Conference paper

1. **A. C. Fechete**, S. J. Ippolito, K. Kalantar-zadeh, W. Wlodarski, A. S. Holland, K. Galatsis, G. Kiriakidis, N. Katsarakis and M. Katharakis, “The Study of $\text{InO}_x/\text{ZnO}/\text{XZ LiNbO}_3$ Layered SAW Devices for Ozone Sensing”, Proceedings of IEEE Sensors, vol. 3, pp. 1510-1513, 2004.
2. **A. C. Fechete**, W. Wlodarski, S. Kaciulis and L. Pandolfi, ”Characterization of r.f. Sputtered $\text{InO}_x/\text{SiN}_x$ Thin Films for Gas Sensing Applications”, in Sensors and Microsystems, in: C. Di Natale, A. D’Amico, P. Siciliano (Eds.), Proceedings of the 10th Italian Conference, World Scientific, Singapore, 2006.
3. **A. C. Fechete**, W. Wlodarski, A. S. Holland, K. Kalantar-zadeh, “Growth of Indium Oxide Nanostructures by Thermal Evaporation” Proceedings of the International Conference on Nanoscience and Nanotechnology (ICONN’06), 3-7 July 2006, Brisbane.
4. **A. C. Fechete**, H. Huang, T. White, O. K. Tan, W. Wlodarski, K. Kalantar-zadeh and A. S. Holland, “Gas Sensing Properties of Tin Dioxide Nanorods Grown by Plasma Enhanced Chemical Vapour Deposition”, 7th East Asian Conference On Chemical Sensor, Singapore, 3 - 5 December, 2007.

The author has also attended and presented at the following international conferences:

- International Symposium on Smart Materials, Nano-, and Micro-Smart Systems, Sydney, Australia, 12-14 December, 2004 – Oral Presentation
- International Workshop and Postgraduate Symposium on Nanotechnology, Perth, Australia, 17-22 July, 2005 – Oral Presentation
- EUROSENSORS XIX, The 19th European Conference on Solid-state Transducers, Barcelona, Spain, September 11-14, 2005 – Poster Presentation
- ICONN'06, International Conference on Nanoscience and Nanotechnology, Brisbane, Australia 3-7 July, 2006 – Poster Presentation

1.4 Thesis Organisation

The thesis is organised into eight chapters and four appendices, with a list of references.

Chapter 1 describes the motivation behind the development of a layered SAW based gas sensors and outlines the author's achievements and publication record.

Chapter 2 provides a critical literature review of SAW based devices and semiconductor metal oxide (SMO) materials and the proposed novel sensor structures are presented.

Chapter 3 describes the layered SAW based sensor. It starts with an explanation of the operation principle of a SAW based device followed by a presentation of a layered SAW based gas sensor. The SMO gas sensing mechanism is also discussed and the chapter concludes with a discussion on the effect of thin film grain size on the sensitivity of a SMO based gas sensor.

Chapter 4 describes the SAW transducer fabrication steps and the intermediate and SMO gas sensitive layer deposition procedures.

Chapter 5 describes the gas sensor calibration system and testing procedure.

Chapter 6 focuses on the presentation of the sensor layers microstructural characterisation results obtained by XRD, XPS, TEM and SEM analyses.

Chapter 7 investigates and reports the gas sensing performance of the developed layered SAW and conductometric sensors.

Finally in **Chapter 8** the major conclusions from this work are given along with suggestions for possible future work.

Chapter 2

Literature Review and Research Rationale

The previous chapter outlined the motivation and objectives of this research work. In order to fulfil these objectives the author is proposing a new layered SAW structure utilising nanostructured materials as sensitive layers. The author has chosen to investigate such sensors on the basis of a literature review of SAW based sensor devices and semiconductor metal oxide (SMO) materials.

This chapter is divided into three sections. In the first section (2.1), a critical literature review of SAW based devices is provided. The second section (2.2) presents the rationale and justification for selecting the SMO materials InO_x and SnO_2 , which were used as gas sensitive layers. In the last section (2.3) the proposed novel layered SAW sensor structure will be presented.

2.1 Literature Review of SAW Based Devices

Surface acoustic wave devices have been in commercial use for more than 40 years, mainly in the telecommunication industry, in mobile phones and base stations, and as band pass filters of transceiver electronics [34]. A historical account of the development and application of SAW based devices in the electronics industry can be found in [35, 36].

A SAW transducer is composed of input and output interdigital transducers (IDTs) patterned on a piezoelectric substrate, shown schematically in Figure 2.1. The IDTs consist of thin metal electrodes (known also as fingers). White and Voltmer [37] showed for the first time in 1960s, that by depositing interdigitated metal electrodes on piezoelectric substrates, surface acoustic waves can be directly generated. The application of an alternating voltage to the input IDT induces oscillating electrical fields between pairs of metal electrodes. The field distribution in turn will create particle displacements or strain in the piezoelectric material of a particular crystal orientation generating acoustic (mechanical) waves that propagate away from the input IDT in both directions with velocity v_0 . The output IDT will detect the generated waves and transform the acoustic wave energy back into electrical energy. This discovery resulted in the widespread use of SAW devices in a number of signal processing applications which include frequency filters, resonators, delay lines and convolvers.

The most commonly utilized SAW structures for sensing applications are the devices with a delay line (space) between the input and output IDTs, illustrated in Figure 2.1. For a SAW based gas sensor, a gas sensitive layer is deposited on the delay line. Interactions between the gas sensitive layer and the gas analyte result in perturbations of either mechanical or electrical boundary conditions and the sensor functions via either change in the mass density on the device surface via mass loading, or via conductivity changes of the sensitive layer.

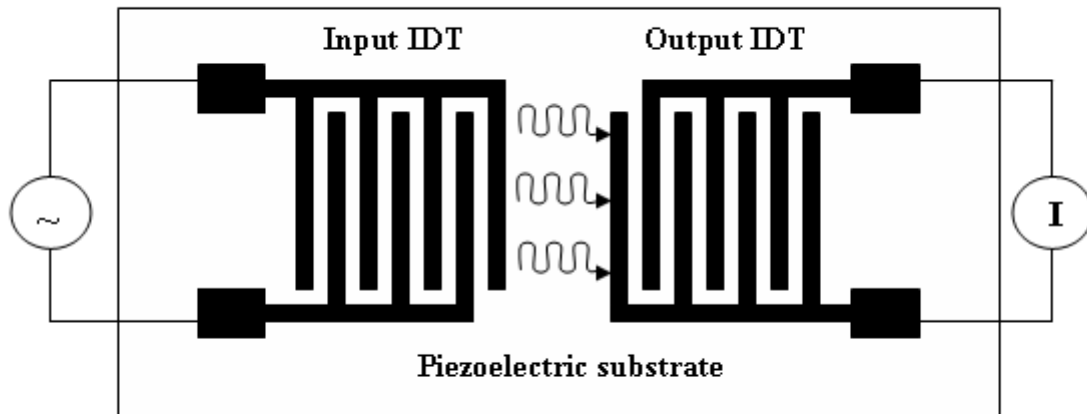


Figure 2.1 Delay line SAW device (plan view)

SAW devices provide several distinctive advantages in comparison with other sensor types, including: a planar structure, direct frequency output signal, and low power consumption. Therefore they are currently used in a wide range of sensor fields mainly in chemical and bio-sensing.

The application of SAW devices for sensing has gained enormous interest since Wohltjen and Dessy introduced a SAW based chemical sensor in 1979 [38]. They utilized a SAW based sensor system employing an ST-cut quartz crystal with IDTs for the excitation and detection of Rayleigh waves, which have particle displacement normal to the substrate surface. Following their work a variety of SAW based sensors were developed for sensing different gases, such as hydrogen [39], nitrogen dioxide (NO₂) [40], hydrogen sulphide (H₂S) [41], sulphur dioxide (SO₂) [42] as well as many other gases.

Initially Rayleigh waves were employed for sensing applications that can be used only in gas media because in liquid these waves are quickly attenuated. In a liquid media a shear horizontal (SH) SAW is usually used where the particle displacement is parallel to the surface, so it can be used for both liquid and gas sensing applications. The vertical displacement particle caused by Rayleigh wave propagation is shown in Fig 2.2 (a1) [43]. Fig 2.2 (b1) shows a schematic of Rayleigh wave propagation in a cross-section through the IDTs of a SAW device. Figure 2.2 (a2) [43] and (b2) show similar representation for SH wave propagation.

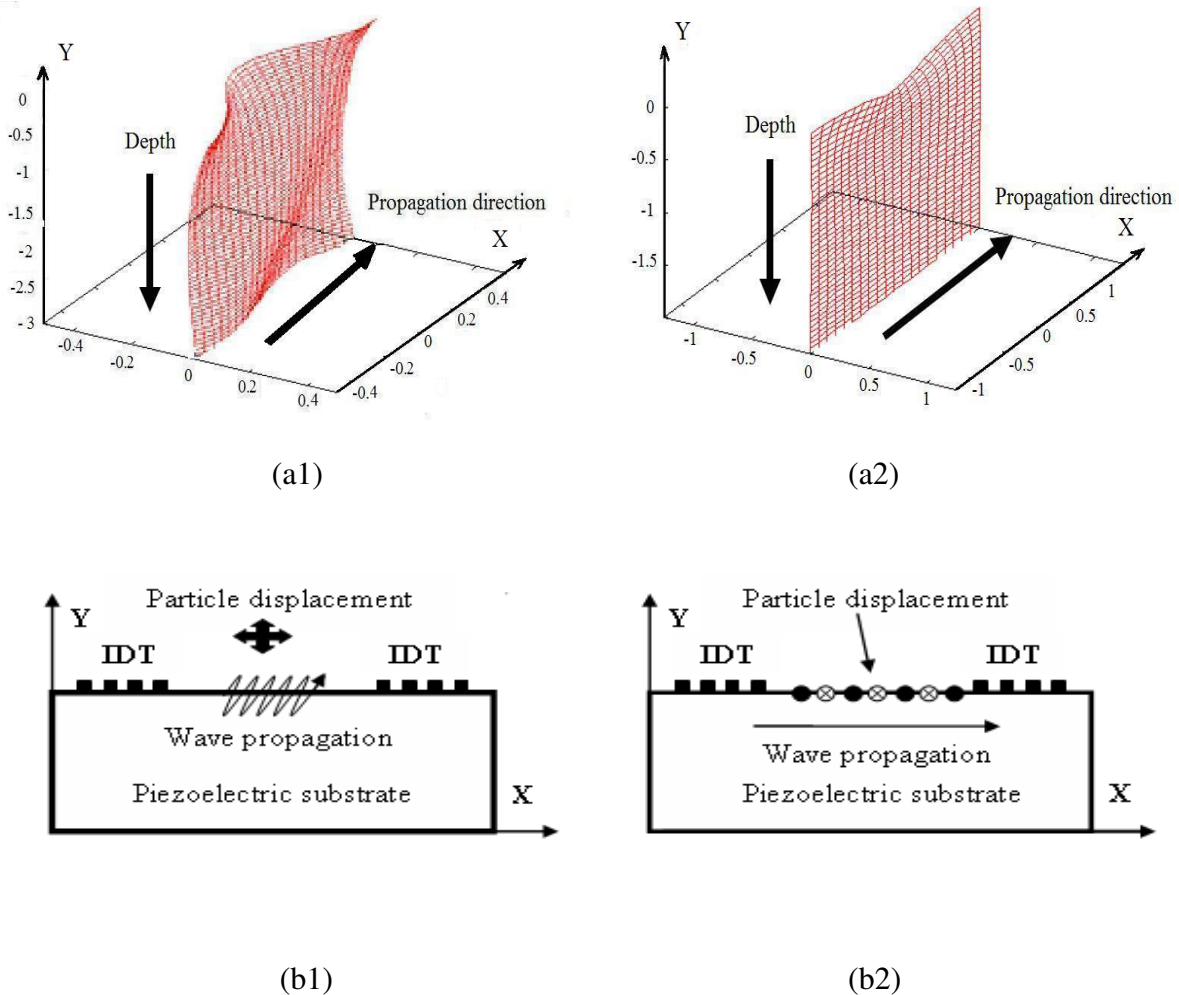


Figure 2.2 Particle displacement for: (a1) Rayleigh SAW and (a2) SH-SAW (from [43]), Cross sectional view of the propagation of (b1) Rayleigh SAW and (b2) SH-SAW between the IDTs of a SAW device

The author has chosen to use 36°YX LiTaO₃ substrates, which support SH-SAW wave propagation. This is also called a Leaky-SAW (LSAW) because it consists of coupled modes involving one term decaying into the substrate and a term representing a radiating bulk wave [44]. Appropriate selection of the most suitable substrate orientation and cut leads to a minimal thermal coefficient of delay (TCD) and a maximum electromechanical coupling coefficient (K^2). The K^2 of the piezoelectric substrate is one of the most important parameters relating to SAW propagation and is the measure of efficiency of a substrate in converting an applied electric energy into mechanical energy associated with a SAW [45].

Takayanagi et al. [46] have shown that the surface wave propagating along the X-axis of Y-cut LiNbO₃ reduces to a SH-type surface wave at a certain rotation angle. As LiNbO₃ belongs to the same class of crystals as LiTaO₃ it was suggested that this type of wave can occur in this substrate too. In fact later in 1977 Nakamura et al. [44] showed that the LSAW propagating along the X axis of a rotated Y-cut of LiTaO₃ substrate reduces to a perfect surface wave (or non-leaky) at the rotation angles of 36° and 126°. They concluded that the surface wave with the rotation angle of 36° is a SH-type SAW and that at 126° is a Rayleigh-type SAW. Besides the SH-type surface wave on the 36° YX LiTaO₃ substrate there can also exist a Rayleigh wave propagating along the X-axis with free surface velocity $v_f = 3232$ m/s but with a very small electromechanical coupling coefficient ($K^2 = 0.00046$). It has also been shown that this substrate supports a surface skimming bulk wave (SSBW) for free surface conditions [45].

The attractive features of a 36°YXLiTaO₃ substrate include not only its high electromechanical coupling coefficient ($K^2 = 0.047$), in comparison with Rayleigh waves, but also a high acoustic wave velocity ($v_f = 4212$ m/s on the free surface and $v_m = 4112$ m/s on a

metallised surface [45]), a relatively low temperature coefficient of delay (45 ppm/°C on the free surface and 32 ppm/°C on the metallised surface) and very low attenuation in the bulk of the substrate. In fact Meier and Russer [47] have calculated the phase velocities and the accompanied attenuation constants at different rotation angles of the LSAWs. They have reported that the attenuation was almost equal to zero ($\delta = 2.7 * 10^{-4} \text{ db} / \lambda$) at the rotation angle of $\theta = 36^\circ$, when the LSAW reduces to a perfect surface wave. The discovery of these advantages raised the interest of various groups in investigating LSAW propagation on different substrates and orientations for applications in the electronics industry as frequency filters.

Moriizumi et al. [48] reported (for the first time) a LSAW device for liquid sensing applications, using 36°YX LiTaO₃ substrate, that had a frequency shift three times greater than could be obtained with an AT-cut quartz (QCM) oscillator. Since then this type of wave has been utilised extensively, mainly for liquid sensing [49, 50] as well as for gas sensing applications [51]. The properties of piezoelectric LSAWs in different materials and cuts are summarised in Table A1 of Appendix A in this thesis.

One of the distinctive advantages of SAW devices is that they are sensitive to mass and conductivity changes. Mass based sensing is one of the most commonly used. The change in the acoustic wave velocity is caused by a mass increase due to the molecules absorbed on the structure surface. Typically used mainly for liquid sensing, mass absorption mechanism has been also employed for gas sensing, e.g. for volatile organic compounds. SAW sensors based on the change of the conductivity of the sensitive layer, which causes a shift in oscillating frequency, using a non-layered device were first reported by Ricco and Martin [11].

A significant step in the development of SAW devices was the introduction of a layered SAW device (with an intermediate layer between the substrate and sensing layer) after Love [52] showed that a low velocity layer on a semi-infinite substrate will have a trapping effect on shear waves, making such a device more sensitive to changes in surface boundary conditions. A Love wave can exist only if the shear velocity of this intermediate layer is less than the shear velocity in the substrate [53]. A Love wave device was applied for the first time as an immuno-sensor by using synthetic polymer, Polymethyl methacrylate (PMMA) intermediate layer, deposited onto 90° rotated ST-quartz [54]. PMMA has a low density and low shear modulus and can be deposited using relatively simple techniques such as spin coating. However it has high acoustic losses in comparison with other materials used for SAW sensing, resulting in a high insertion loss inhibiting the device operation. Love wave devices were also developed by Jacoby et al. [55] using a polymer sensitive layer for vapour sensing applications. Zimmermann et al. [56] applied a Love wave device for organophosphorous vapours and achieved approximately 10 times the sensitivity of a Rayleigh wave sensor operating at a similar frequency. Furthermore Kovacs et al. introduced a SiO₂/90° ST-quartz Love wave structure [57]. The acoustic loss of SiO₂ is less than for the polymers but for a higher sensitivity a thick layer and long deposition time is necessary for devices operating at low frequency. Utilising ZnO as an intermediate layer on a quartz substrate Kalantar-zadeh et al. showed that mass sensitivity improved compared to SiO₂ [58]. The investigation of layered SAW devices, such as the Love wave device, by using a suitable intermediate layer (e.g. thickness, and material selection) provided a more sensitive sensor devices compared with their non-layered counterparts.

Another major step in the development of SAW devices was the introduction of multilayered structures by Du et al. [59]. Using a PMMA/SiO₂/quartz layered SAW; higher sensitivity was obtained, compared with devices having only SiO₂ or a PMMA layer. In 1992 Niewenhuizen

et al. [60] developed a conductometric multilayered device with a $\text{Si}_3\text{N}_4/\text{ZnO}/\text{SiO}_2/\text{Si}$ structure with a copper phthalocyanine sensing layer for NO_2 sensing with the aim to integrate the sensor with IC fabrication technologies. The Si_3N_4 layer was used to prevent interaction of the gas molecules with the reference delay line. In 2002 Jakubik et al. [61, 62] used a metal-free phthalocyanine/copper phthalocyanine intermediate layers and a palladium sensitive layer for H_2 sensing to increase the sensitivity by matching the conductivity of the sensing layer with the operation point of the SAW mode.

Recently Ippolito et al. [51, 63] reported layered SAW sensors for NO_2 and H_2 with a ZnO intermediate layer deposited on lithium tantalate and lithium niobate substrates. By optimising the thickness of the intermediate layer (velocity-permittivity product of the SAW device with the conductivity of the sensing layer) it was shown that the sensitivity of a sensor can be increased [29].

There are numerous comprehensive reviews regarding the developments of SAW gas sensors compiled by D'Amico et al. [64] in 1989, Ballantine and Wohltjen [65] also in 1989, Vellekoop in 1998 [10], Cheeke and Wang [66] in 1999, and more recently Drafts [67] and Anisimkin et al. [68] in 2001.

With recent developments in nanotechnology and the synthesis of 1-D nanostructures the current trend in research and development is focusing on the application of these structures in SAW sensor technology. A SAW device with a sensitive layer of polyaniline nanofibres for H_2 sensing, which can be operated at room temperature, was reported in 2005 [69]. Recently Penza et al. [70] developed a highly sensitive layered SAW device for H_2 , NH_3 and NO_2

sensing using carbon nanotubes on ZnO/LiTaO₃ obtaining high sensitivity at room temperature.

Another trend in gas sensor research and development is the use of sensor arrays (commonly referred to as “electronic noses”), containing several different SAW sensors, each with their own response characteristics. Early research was lead by D’Amico and Verona [64] followed by Ballantine and Wohltjen [65] and by Grate et al. [42]. Recently Alizadeh and Zeynali [71] reported a polymer coated SAW sensor array for sensing warfare chemical agents. Fernandez et al. [72] developed an electronic nose based on a SAW sensor array using ZnO for sensing of three volatile compounds: octane, toluene and methyllethylketon.

2.2 Literature Review of Semiconductor Metal Oxide Thin Films Pertaining to this Research

Since the development of the first Semiconductor Metal Oxide (SMO) gas sensors by Taguchi [73] and Seiyama [8] in the 1960s, much research has been carried out to investigate different SMO thin films for gas sensing applications. The SMO sensing mechanism involves an electrical conductance change caused by absorption and chemical reaction on the semiconductor surface. Seiyama used zinc oxide (ZnO), demonstrating that if this material is heated in air, the conductivity change of the ZnO thin film is proportional to the concentration of the reactive gas present in the ambient. Taguchi used a porous sintered SnO₂ thin film, obtaining a sensor with stable responses. Since these early efforts, many other SMO materials have been used for gas sensing applications; such as titanium oxide (TiO₂), tungsten trioxide (WO₃), indium oxide (In₂O₃) and molybdenum oxide (MoO₃) although the vast majority of research used SnO₂ [74,75,76].

Gas sensors based on SMO thin films have been successfully commercialised and many companies have been established to develop and manufacture sensors for different sensing

applications in areas such as environmental monitoring, domestic safety, public security, the automotive industry and sensor networks. Commercial enterprises, which have developed gas sensors for O_3 and NO_x detection using In_2O_3 and WO_3 , include New Cosmos and Figaro [77,78]. Although the last four decades has seen considerable progress in the development of SMO gas sensors, today there is still intense worldwide research activity to improve the “3S”s: Sensitivity, Selectivity and long-term Stability of these sensors.

In 1991 Yamazoe et al. [79] demonstrated that the reduction of the polycrystalline film grain's sizes increased the SMO sensor performance. Since then the challenge became to prepare SMO layers with small grain sizes and thin films were deposited by chemical and physical evaporation. Tremendous advancement has also been achieved with the development and synthesis of stable single crystal one dimensional (1-D) SMO nanostructures (e.g. nanobelts and nanowires) and with their application for gas sensing [28]. 1-D nanostructures obtained by thermal evaporation at high temperatures (e.g. nanowires, nanobelts, nanorods) exhibit novel physical and chemical properties in comparison with microstructured thin films [80]. Their application in the field of sensor devices is predicted to be very promising as they have a larger surface to volume ratio (compared with their microstructured film counterparts) that increases considerably the sensitivity of the devices made with such films [33]. In addition, the device's power consumption is considerably reduced as the sensors operate at lower working temperatures or even at room temperature, so there is no need of an additional heating element. Therefore the current research and development efforts are directed towards optimising their deposition conditions and to gaining a deeper understanding of the physical and chemical properties of 1-D SMO nanostructures.

2.2.1 Literature Review of Indium Oxide Thin Films for Gas Sensing

Indium oxide is an n-type semiconducting metal oxide in its non-stoichiometric form, with high free electron concentrations. The sensitivity of InO_x can be attributed to the oxygen vacancies in the films; by controlling the oxygen deficiency, the conductivity of InO_x films can be altered [31]. Indium oxide films have typically a high dispersity, a desirable condition for the absorption of gases like NO_2 and O_3 . In 1993 Takada reported an O_3 sensor using an In_2O_3 thin film [9]. Since then different deposition techniques, e.g. spray pyrolysis, spin coating, sol-gel method and magnetron sputtering have been used to enhance the sensitivity of In_2O_3 thin films [81-85]. Using the sol-gel method, highly dispersed In_2O_3 films with a significant deviation from stoichiometry were obtained [85]. Doping InO_x films with molybdenum and nickel ions further increases the sensitivity [86]. Gurlo et al. [87] correlated the sensing properties of In_2O_3 films to the grain size distribution and morphology of the sol-gel prepared films. Furthermore, Korotcenkov et al. [82] reported that In_2O_3 porous films with small grain sizes had a high sensitivity towards O_3 and fast response compared with previously reported thin films. Previously, highly sensitive films towards O_3 capable of sensing 5-100 ppb concentrations were reported by Faglia et al. [88] using Au-doped indium oxide thin films.

Comprehensive research has been completed by Kiriakidis et al. [31, 89], who investigated d.c. sputtered InO_x films for O_3 sensing application. The films were exposed to UV light (photo reduction/oxidization), which increased the sensitivity towards O_3 by six orders of magnitude. More recently Suche et al. [90] presented a comprehensive study of the influence of the d.c. sputtered InO_x thin films surface topology on ozone sensitivity, concluding that grain size variation mostly determines the sensitivity towards O_3 .

In the past few years stable 1-D indium oxide nanostructures, such as nanowires and nanobelts have been synthesised and used in devices for the detection of gases such as NO₂, ammonia and ethanol. Li et al. [91] reported a gas sensor FET structure for ammonia and NO₂ sensing in the presence of argon at room temperature. In 2004 the same authors reported the detection of NO₂ down to ppb levels for the first time with metal oxide nano-wire transistors [92]. In 2006 Comini et al. [93] deposited nanowires on d.c. conductometric sensors which were sensitive to CO and NO₂ at the working temperature of 200°C, observing that responses were strictly dependent on the lateral dimensions of the wires. More recently M. Epifani et al. [94] using chemical syntheses have developed highly sensitive (60 ppb) O₃ sensors using a nonporous and nanocrystalline In₂O₃ layer.

2.2.2 Literature Review of Tin Oxide Thin Films for Gas Sensing

Since the development of the first SnO₂ based gas sensor by Taguchi in 1962, the vast majority of research and development of gas sensors has been undertaken using this material. Solid-state gas sensors based on SnO₂ have become the dominant devices for gas alarms used in domestic, commercial and industrial premises [95]. SnO₂ is an n-type semiconductor material widely used in devices for the sensing of a wide range of oxidizing and reducing gases, and is capable of operating at temperatures in the range of 200 - 500°C [96]. Different fabrication techniques have been used for SnO₂ based sensors with different degrees of success. Most commercially available sensors with high sensitivity and long-term stability were produced by ceramic fabrication processes [97]. A thick-film SnO₂ sensor presents several disadvantages such as poor selectivity, dependence on relative humidity and large power consumption.

With the improvement of thin-film fabrication technologies, such as evaporation and sputtering processes, some of these disadvantages were substantially reduced or eliminated.

Consequently, thin polycrystalline, nanocrystalline films with different thicknesses were obtained by thermal, electron-beam evaporation and reactive sputtering. In a similar manner to indium oxide, research has also been carried out to reduce grain sizes and hence the sensitivity was increased and improvement in dynamic performance has been achieved

With the appearance of 1-D nanostructures, research efforts have been directed to synthesis of SnO₂ nanowires and nanobelts using vapour-solid (VS) and vapour-liquid-solid (VLS) growth processes by the evaporation of commercial nanopowders in a furnace under controlled conditions. In 2002 Law et al. [98] developed a room temperature single crystalline based d.c. conductometric sensor for NO₂ detection. Later in 2004 Zhang et al. [99] presented a SnO₂ nanowire in a FET structure for CO, NO₂ and O₂ sensing. In 2005 Comini et al. [100] used tin oxide nanobelts as conductometric gas sensors obtaining high sensitivity towards NO₂ (few ppb), CO (30ppm) and ethanol (10ppm), observing that ethanol sensing is strongly influenced by the density of the nanobelts.

2.3 Proposed Layered SAW Gas Sensor Structure

Based on the literature review presented above, the author is proposing a novel layered conductometric SH-SAW O₃ and H₂ sensor with InO_x/Si₃N₄/36° YX LiTaO₃ structure, shown schematically in Figure 2.3.

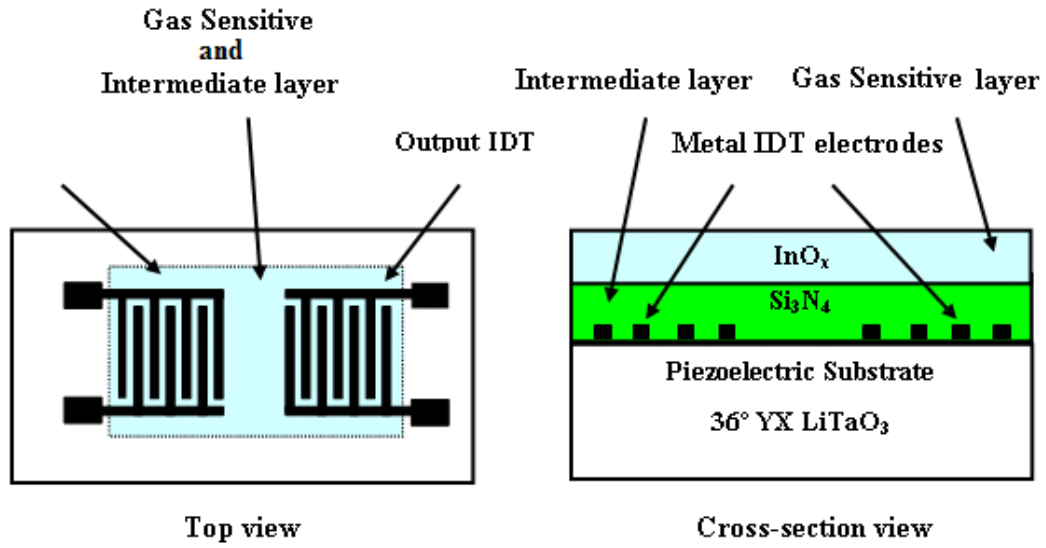


Figure 2.3 Proposed novel layered SH-SAW structure

In addition, the author has utilised a 1-D SnO_2 nanostructures as a gas sensitive layer on a $36^\circ \text{ YX LiTaO}_3$ substrate, since a novel method has been found to deposit this material at a significantly lower temperature (90°C) than for layers of 1-D indium oxide nanostructures. The author undertook an investigation to synthesize indium oxide nanowires by thermal evaporation. The nanowires were successfully synthesised but this was only possible at an elevated temperature which obliterates the LiTaO_3 substrate piezoelectricity making the structure unusable as a SAW sensor operation after deposition of the nanowires. An account of this investigation is included in Chapter 6.

The $36^\circ \text{ YX LiTaO}_3$ piezoelectric substrate was selected as it has a high K^2 and almost zero attenuation in the bulk of the substrate when compared to other LSAW substrates (e.g. LST-Quartz). InO_x and SnO_2 SMO materials are very sensitive n-type SMO materials towards both reducing and oxidizing gases.

The silicon nitride intermediate layer presents several attractive properties, such as high wear resistance and low propagation loss [32]. It has wide application in semiconductor devices and as a thin dielectric film it has been incorporated into SAW devices on LiNbO_3 substrates for electronics applications [101]. This layer can provide various functions including, device passivation, waveguiding, reflective structures and can be employed as a protective layer.

A non-layered SAW based device has been developed for ozone sensing [102]. It is the opinion of the author that the proposed layered SAW structure will provide an improved gas sensing performance towards O_3 and H_2 in comparison with other SAW devices currently available.

2.4 Summary

In this chapter the author presented a critical literature review of the SAW devices and SMO materials with an emphasis towards gas sensing applications. Based on this literature review, the author proposed a novel layered SAW sensor structure.

The author referred to literature on SAW devices and SMO materials to systematically direct the reader to relevant publications, highlighting the advantages for the selected materials for the novel sensor structure. The chapter concluded with presentation of the proposed layered SAW structure. The following chapters of this thesis will investigate the benefits and unique features of this sensor structure.

Chapter 3

Layered SAW Gas Sensor

This chapter is dedicated to analyses of the layered SAW gas sensors. Section 3.1 describes the operation principle of SAW devices. This is followed by the presentation of SAW based gas sensors (including the layered SAW based sensors) in section 3.2. The method used by the author to determine the intermediate and gas sensitive layer thicknesses is also described in this section.

A brief discussion of the Semiconductor Metal Oxide (SMO) gas sensing mechanism is included in section 3.3. An overview of the two types of SMO sensitive layer morphologies, (i) compact and (ii) porous layer are presented in section 3.4. Then the chapter concludes in section 3.5 with a discussion of the grain size effect on the sensitivity of SMO gas sensors.

3.1 Operation Principle of SAW Based Sensors

Operation of a SAW sensor is based on the detections of small changes in its acoustic wave propagation characteristics (e.g. change of the acoustic velocity or attenuation) caused by perturbations on the active surface of the device. These perturbations can be affected by many external factors; each can cause a potential sensor response [103, 104]. The following general equation (3.1) illustrates the possible external perturbations of the acoustic wave phase velocity due to T - temperature, E - electric field, ε - permittivity, σ - electrical conductivity, m - mass and p - pressure [11].

$$\frac{\Delta v}{v_0} \cong \frac{1}{v_p} \left(\frac{\partial v}{\partial T} \Delta T + \frac{\partial v}{\partial E} \Delta E + \frac{\partial v}{\partial \varepsilon} \Delta \varepsilon + \frac{\partial v}{\partial \sigma} \Delta \sigma + \frac{\partial v}{\partial m} \Delta m + \frac{\partial v}{\partial p} \Delta p + \dots \right), \quad (3.1)$$

where v_p is the phase velocity and v_0 is the unperturbed velocity. Changes in the parameters shown can cause a change on the surface of the device producing a measurable shift of the SAW mode's phase velocity. Since SAW devices use a piezoelectric substrate for the generation and detection of the acoustic waves the parameters involved in a sensors applications can be either mechanical or electrical and it is possible to obtain expressions for $\Delta v/v_0$ for different cases using the theory of perturbation and the appropriate boundary conditions (e.g. mechanical or electrical) [105]. In terms of a chemical sensor in the early stages of development in the 1980s, the emphasis was on the accumulation of surface mass since the first SAW device utilised thin polymer, metallic or metal oxide layer [39, 64, 106]. However the influence of the sheet conductivity of these layers was also recognised [11]. In the following section the factors that can make a substantial contribution to the sensors response will be presented (e.g. acoustoelectric effect, mass loading and elastic and viscoelastic effect).

3.2 SAW Based Gas Sensors

A SAW based gas sensor consists usually of a delay line device with a gas sensitive layer deposited on the active surface between the input and output IDTs. The sensing mechanism involves the chemical interaction between the analyte gas and the gas sensitive layer producing a shift in the SAW mode's phase velocity, due to the perturbations described by equation (3.1).

In the case of a SAW device, which operates due to the conductivity change of the gas sensitive layer, the interaction of the gas analytes with the layer perturbs the electrical boundary conditions at the surface, and a change in the electrical conductivity of the sensitive layer takes place. Accordingly, the velocity and attenuation of the propagating wave is changed by this surface interaction. There are two common methods used for measuring the change in the SAW velocity, the phase and frequency measurement methods [107]. In this work the frequency measurement technique was employed by measuring the oscillation frequency of the device. The change in the SAW phase velocity (Δv) can be related to the change in the device's oscillation frequency or frequency shift (Δf) by the following relationship:

$$\frac{\Delta f}{f_0} \cong \frac{\Delta v}{v_0} \quad (3.2)$$

where f_0 is the oscillation frequency and v_0 is the SAW velocity [103]. In this way, the measured frequency shift Δf can be correlated to the concentrations of the gas analyte. More details regarding the frequency measurement technique and a description of the measurement set-up are included in Chapter 5.

For the proposed layered SAW structure, in this Ph.D. project, the sensitive layer covers the entire surface of the device. In this way, the sensitive layer's interaction area is increased.

A SAW propagating in a piezoelectric material generates a layer of bound charge, which accompanies the mechanical wave. A discussion on the Shear Horizontal SAW (Leaky SAW) propagation is included in Appendix B of the thesis.

When SAW propagates through the device, the charge carriers in the surface film redistributes to compensate for the layer of bound charge generated by the propagating wave [104]. The electrical coupling between the SAW and film can then result in an *acoustoelectric effect*, which is caused by the interactions between the electric fields and charge carriers of the conductive film. The interaction between the mechanical coupling of the SAW and the sensitive film can result in *mass loading* (transfer of mass by the SAW surface displacement). *Elastic and viscoelastic effects* can also occur by the SAW induced deformation of the surface of the film.

Acoustoelectric effect

In 1985 Ricco and Martin [11] developed a SAW sensor based on conductivity change. Using the perturbation theory, and neglecting the thickness of the layer, they showed that the relative change in velocity $\Delta v / v_p$ and the attenuation divided by the wave number $k = 2\pi\lambda$, α / k , for a non-layered SAW device in contact with a thin conductive layer can be calculated by:

$$\frac{\Delta v}{v_p} = -\frac{K^2}{2} \frac{\sigma_{sh}^2}{\sigma_{sh}^2 + (v_p C_s)^2} \quad (3.3)$$

$$\frac{\alpha}{k} = -\frac{K^2}{2} \frac{v_p C_s \sigma_{sh}}{\sigma_{sh}^2 + (v_p C_s)^2} \quad (3.4)$$

where K^2 is the electromechanical coupling of the SAW mode at the device surface, $C_s = \epsilon_0 + \epsilon_p$ is the surface capacitance per unit length (ϵ_p is the substrate permittivity and ϵ_0 the free space permittivity, considering that the layer above the substrate is air), v_p is the phase velocity and σ_{sh} is the sheet conductivity of the layer. From these equations it can be seen that the conductometric sensitivity (or the magnitude of the acoustoelectric response) is proportional to K^2 and the sensitivity is dependent on the sheet conductivity of the thin conductive layer.

The maximum change in velocity and the peak in the attenuation are achieved when $\sigma_{sh} \equiv \sigma_{or} = v_p C_s$, which coincides with maximum power dissipation into the layer. This is called the *resonant (or critical) sheet conductivity* and indicates that for high sensitivity the sheet conductivity of the layer has to be matched to the *velocity permittivity* product of the substrate [29, 30].

Substituting $v_p C$ with σ_{or} and dividing by σ_{sh}^2 equations (3.3) and (3.4) can be written as:

$$\frac{\Delta v}{v_p} = -\frac{K^2}{2} \frac{1}{1 + \left(\frac{\sigma_{or}}{\sigma_{sh}} \right)^2} \quad (3.5)$$

$$\frac{\alpha}{k} = -\frac{K^2}{2} \frac{\frac{\sigma_{or}}{\sigma_{sh}}}{1 + \left(\frac{\sigma_{or}}{\sigma_{sh}}\right)^2} \quad (3.6)$$

Plots of equations (3.5) and (3.6) as functions of $\log(\sigma_{sh} / \sigma_{or})$ are given in Figure 3.1:

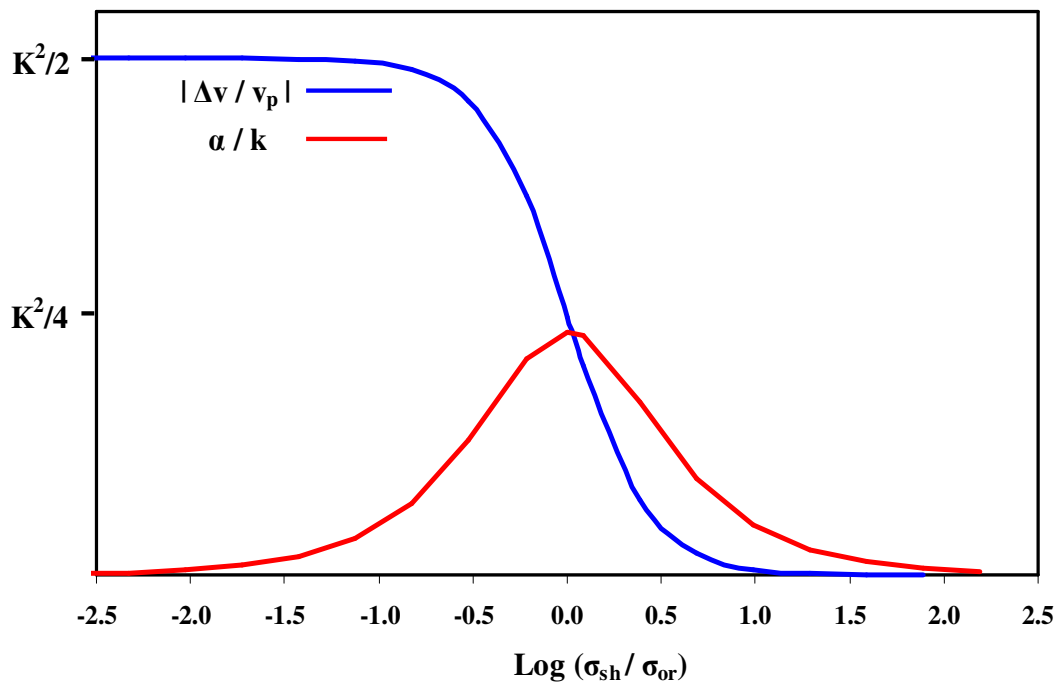


Figure 3.1 Variation of attenuation and relative change of acoustoelectric velocity versus $\log(\sigma_{sh} / \sigma_{or})$ of a sensitive layer

From this figure it can be seen that when the sensitive (conductive) layer sheet conductivity falls in the highest gradient region of the curve (i.e. the sheet conductivity of the sensitive layer will be matched to the velocity permittivity product of the substrate), the maximum sensitivity is obtained.

Mass Loading

The simplest and most utilised SAW sensor applications are represented by mass accumulation on the surface of the sensor. It is well known that the change in wave velocity and attenuation can be related to the changes in the wave energy density and power dissipation [104].

When the wave is propagating through a unit cube with the energy density of U (energy/volume), the energy density increases by the incident power density P (power/area) times the transit time $\tau = 1/v$:

$$U = P\tau = \frac{P}{v} \quad (3.7)$$

and from here:

$$P = Uv \quad (3.8)$$

In a lossless medium (when P is constant) the changes in wave velocity can be related to the changes in wave energy density by differentiating equation (3.7):

$$\frac{\Delta v}{v_0} = -\frac{\Delta U}{U_0} \quad (3.9)$$

where v_0 and U_0 are the unperturbed velocity and energy density. From this equation it can be seen that an increase in the kinetic energy density causes a decrease in the wave velocity. The displacement of particles in a thin and rigid surface layer causes an increase in the kinetic

energy density U_k without dissipating any wave energy. By definition the instantaneous kinetic energy density (kinetic energy/volume) is given by:

$$U_k = \frac{1}{2} \rho \sum_1^3 \dot{u}_i^2 \quad (3.10)$$

where the squares of the particle velocities \dot{u}_i over three directions are summed and ρ is the density. For a sinusoidal wave the change in average kinetic energy per area of the surface can be written as:

$$\Delta U_k = \frac{\rho}{4} (v_{xo}^2 + v_{yo}^2 + v_{zo}^2) \quad (3.11)$$

where v_{xo} , v_{yo} and v_{zo} are the particle velocities in x, y and z directions. From equations (3.7), (3.9) and (3.11) an expression for the change in wave velocity caused by surface mass loading can be obtained:

$$\frac{\Delta v}{v_0} = -\frac{\omega v_0 \rho}{4} \left(\frac{v_{xo}^2}{\omega P} + \frac{v_{yo}^2}{\omega P} + \frac{v_{zo}^2}{\omega P} \right) \quad (3.12)$$

The wave velocities increase proportionally to $(\omega P)^{1/2}$. The term in bracket is a constant of the material, depending only by the substrates material and is independent of the wave amplitude.

Hence equation (3.12) can be written as:

$$\frac{\Delta v}{v_0} = -c_m f_0 \rho_s, \quad (3.13)$$

where c_m is a constant called the mass sensitivity factor. This equation represents the mass-induced change in SAW propagation velocity, where the mass sensitivity factor is given by:

$$c_m = \frac{\pi v_0}{2} \left(\frac{v_{xo}^2}{\omega P} + \frac{v_{yo}^2}{\omega P} + \frac{v_{zo}^2}{\omega P} \right) \quad (3.14)$$

The equation (3.13) shows clearly the frequency dependence of the SAW mass sensitivity.

The fractional velocity change varies (increases linearly) with the operating frequency f_0 .

Elastic and Viscoelastic effect

When the films have finite thickness and elastic properties it is necessary to consider the effects of SAW induced deformations. An elastic and/or viscoelastic film on a SAW device causes additional contributions to the SAW velocity and attenuation energy storage and power dissipation [108]. These films can be described by the bulk modulus: $K = K' + K''$ and shear modulus $G = G' + G''$, where K' and G' are the *storage moduli*, K'' and G'' are the *loss moduli*.

Two different type of film can be identified here:

- *Acoustically thin films*, where the entire film moves synchronously with the substrate surface, resulting in uniform displacement across the films thickness [104].

- *Acoustically thick films*, the upper part of the film lags behind the film/substrate surface, resulting in non-uniform displacement across the film thickness. This leads to shear displacement in the film, which can be described by the viscoelastic response. This film type is characteristic of polymer films and has been studied in great detail by Martin et al. [109].

In the case of an (acoustically thin) perfectly elastic film when there is no loss ($K'' = G'' = 0$) Tiersten and Sinha [110] have shown that the velocity perturbation is given by

$$\frac{\Delta v}{v_0} = -\omega h \left[c_1 \left(\rho - \frac{\mu}{v_0^2} \right) + c_2 \rho + c_3 \left(\rho \frac{4\mu}{v_0^2} \frac{\lambda + \mu}{\lambda + 2\mu} \right) \right], \quad (3.15)$$

where c_1 , c_2 and c_3 are the films coupling parameters, ρh is the mass loading term, λ and μ are the Lamé constants.

The author has utilised in this research work indium oxide films (n-type semiconductor metal oxide material) as gas sensitive layers for the proposed layered SAW structures. As the observed attenuation of SAW sensors responses was negligible, when they were exposed to the gas analytes, it is believed that the responses are primarily caused by the acoustoelectric effect (e.g. change in conductivity of the indium oxide layer). The mass loading (and/or elastic/viscoelastic effects) were reported to be mainly responsible for non-layered SAW sensor's responses when polymer based and/or palladium films were used [39, 103, 111]

3.2.1 Layered SAW Sensors

Layered SAW devices use an intermediate layer deposited between the substrate and the gas sensitive layer, isolating the IDT electrodes from the analyte gas. By combining a high electromechanical coupling coefficient (K^2) piezoelectric substrate with suitable intermediate and gas sensitive layers, significant improvements in the gas sensing performance of a SAW device can be achieved [30].

As previously described for conductivity based sensing applications K^2 can be thought as a measure of the interaction between electrical and mechanical fields in a piezoelectric material [30]. This parameter can be estimated by [45]:

$$K^2 = 2 \frac{v_f - v_m}{v_f} \quad (3.16)$$

where v_f and v_m are the free surface and metallised surface phase velocities, respectively. The metallised surface condition can be modelled with an infinitesimal thin, perfectly conducting layer on the device surface. The value of K^2 depends on the media in which it is calculated. In non-layered devices it should be calculated at the substrate surface whereas in layered devices can be either calculated at the interface of the intermediate layer and the substrate or at the surface. For conductivity based sensors, it should be calculated at the device surface [30].

3.2.1.1 Determination of the Optimum Intermediate Layer Thickness

The addition of an intermediate layer can increase the acoustic energy confinement at the surface as well as isolate the IDT electrodes from the sensitive layer. In addition it can

also influence the velocity of the propagating SAW, effective permittivity and K^2 of the structure [30]. The intermediate layer material should be homogeneous, has low acoustic loss and should electrically isolate the IDTs from the sensitive layer. Hence, the intermediate layer material properties and thickness need to be considered, and chosen carefully. In order to determine an appropriate thickness for the intermediate layer the author utilised a theoretical approach combined with the experimental work.

Theoretical approach

At the beginning of this research work, after the literature search was completed, the simulation of the proposed SAW sensor structure was performed using the “SAW Analysis” software which was developed by E. L. Adler [112,113]. This program was based on the scattering matrix method. Simulations were carried out to determine the optimal thicknesses of the intermediate layer. Soon after this a new software program called “SAW Software” was developed by D. A. Powell [114] at the Sensor Technology Laboratory at RMIT University. This software consists of three main modules based on *Green's function* [115,116]. It can calculate parameters such as the velocity and electromechanical coupling coefficient K^2 as a function of the thicknesses of the layers deposited on the SAW device substrate.

As can be seen from equations (3.3) and (3.4), the conductometric sensitivity (or the magnitude of the acoustoelectric response) is proportional to K^2 . The simulations were performed to investigate the variation of this parameter with the intermediate layer thickness.

Using this newly developed software program the simulations of the proposed SAW layered structure, which was previously performed using the “SAW Analysis” software, were replicated. The stoichiometric silicon nitride (Si_3N_4) material constants, e.g. elastic stiffness c_{11} and c_{44} , density ρ and permittivity ε (all material constants are included in the Appendix C

of the thesis) from [117] were used for determining the most suitable thickness of the intermediate layer for optimising K^2 . The variation of K^2 as a function of Si_3N_4 layer thickness is shown in Figure 3.2 below.

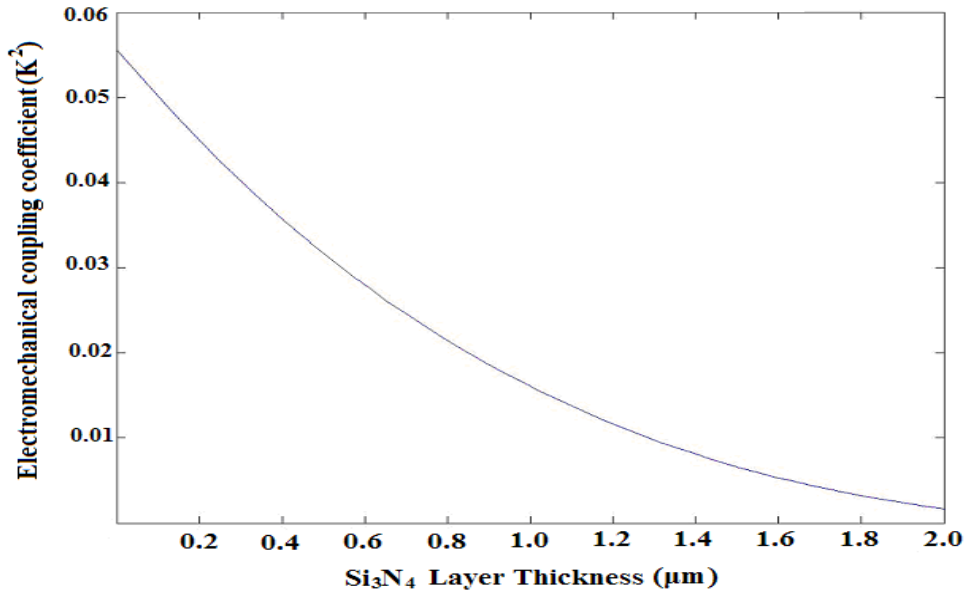


Figure 3.2 The electromechanical coupling coefficient (K^2) versus Si_3N_4 layer thickness: calculated for a periodicity of $\lambda = 24$ (μm) at the 36°YXLiTaO_3 substrate

As it can be seen, the K^2 value decreases with the increase of the intermediate layer thickness. Soon after the first set of simulations was completed for the $\text{Si}_3\text{N}_4/36^\circ\text{YXLiTaO}_3$ structures and the first SAW devices were fabricated, microstructural characterisations were performed to determine the stoichiometry of the deposited intermediate layers. When the r.f. sputtered method was used, the deposited films had a silicon oxynitride composition (SiO_xN_y – the microstructural characterisation results are presented in chapter 6).

Experimental work

Considering the microstructural characterisation results and also the fact that the simulations were performed using the stoichiometric silicon nitride (Si_3N_4) material constant, to determine the suitable thickness of the intermediate layer the author has incorporated the experimental results.

Intermediate layers with thicknesses of 0.2 μm , 0.5 μm , 0.8 μm , 1 μm and 2 μm were deposited by using r.f. magnetron sputtering from a Si_3N_4 target (the only available deposition method for Si_3N_4 at RMIT University) on the 36°YXLiTaO_3 substrates. All SAW devices were coated with a 100 nm indium oxide thin film using r.f. magnetron sputtering to form the sensitive layer using the same deposition conditions. The method used to determine the thickness of the indium oxide gas sensitive layer is presented in next section.

The fabricated SAW sensors were subjected to the same testing procedure (details can be found in chapter 7) and it was found that the devices with silicon nitride layers thicknesses of 0.2 μm , 0.5 μm , and 0.8 μm were not operational. The first two devices with silicon nitride thicknesses of 0.2 μm and 0.5 μm could not oscillate and as a result they could not be tested as SAW sensors. SAW devices with 0.8 μm thickness were unstable and the oscillations could not be maintained when the devices were exposed to a gas analyte (e.g. H_2) or when the operational temperature was gradually increased (e.g. from room temperature to 150° C).

The author believes that this can be explained by the fact that the r.f. sputtering method causes pinholes (and cracks) in the deposited silicon nitride films. Accordingly the intermediate layer loses its protective function (e.g. it will not stop the shorting of the IDTs after the deposition of gas sensitive layer). It seems that at around the thickness of 0.8 μm these pinholes are

starting to be eliminated or reduced. As a conclusion, it can be stated that the experimental results suggested for an operational SAW device (e.g. to be used as a gas sensor) this should be at least 1 μm (minimum thickness at which oscillations could be maintained).

It is important to point out that:

- the microcharacterisation analyses performed later in this research work consistently showed that the r.f. sputtered intermediate layer is not stoichiometric (e.g. has a similar SiO_xN_y composition)
- no materials constants were available for non-stoichiometric ‘silicon nitride’
- the chosen thickness of 1 μm for the intermediate layer was the was the best trade-off between the SAW device sensitivity and silicon nitride thickness in order to make the SAW device operational.

Comparison of two sets of simulations for the developed SAW structure

In the later stages of this research work the author has organised the deposition of silicon nitride layers by Plasma Enhanced Chemical Vapour Deposition (PECVD) (University of Western Australia) and E-Beam Evaporation (Thailand) as the only available deposition method for Si_3N_4 at RMIT University was r.f. sputtering. Simulations were also performed on the same SAW structure using the PECVD silicon nitride intermediate layer. The used material constants for a PECVD silicon nitride were those reported by Hickernell et al. [118]. Unfortunately no material data constants were available for the E-Beam Evaporated silicon.

Figure 3.3 shows the plots of the theoretical results obtained by performing simulations of K_2 as a function of the Si_3N_4 intermediate layer thickness at the 36°YXLiTaO_3 substrate surface when the two sets of silicon nitride material data constants were used

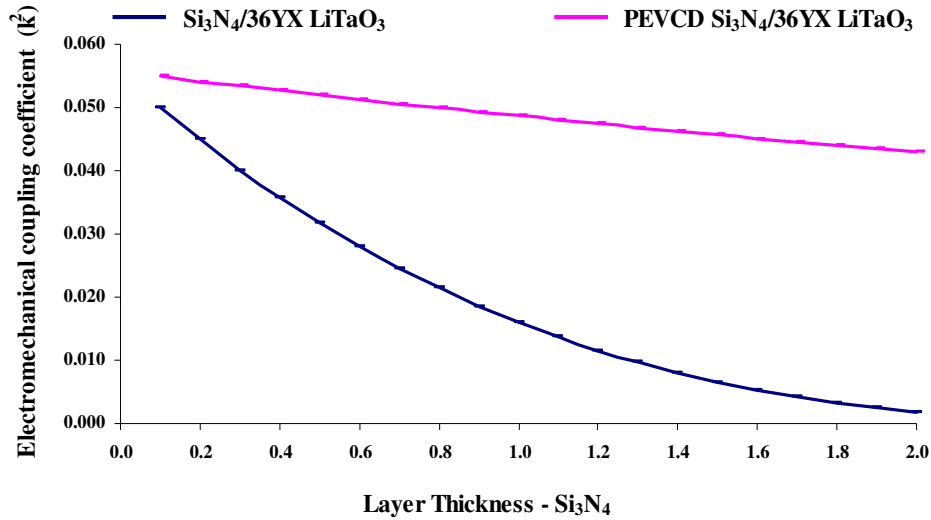


Figure 3.3 Comparison of the electromechanical coupling coefficient (K^2) versus Si_3N_4 layer thickness: calculated for a periodicity of $\lambda = 24 \mu\text{m}$ at the 36°YXLiTaO_3 substrate for two different silicon nitride material data.

It can be seen that there is a significant difference between the two plots. There is a decrease of K^2 for both structures with increasing intermediate layer thickness, but for the device with the PECVD intermediate layer this decrease is considerably less. Or it can be said that the simulation results indicate that the SAW device with the PECVD intermediate layer has a higher K^2 . Undeniably the experimental gas sensing results, presented in chapter 7 of the thesis, shows that the SAW sensor with a $1 \mu\text{m}$ thick PECVD intermediate layer presented a better gas sensing performance. It has a higher response magnitude for H_2 (Table 7.1), faster response and recovery time for both O_3 and H_2 , when compared to the other SAW sensors with $1 \mu\text{m}$ r.f. sputtered and E-beam evaporated intermediate layers.

3.2.1.2 Gas Sensitive Layer Thickness and its Effect on the K^2 of the SAW Structure

The thickness of the indium oxide film was chosen based on the reported literature. The chosen 100 nm is the most researched and reported thickness in the published literature and is the one of the most suitable for ozone gas sensing [90,119,120].

However simulations were also utilised to determine the most suitable gas sensitive layer thickness as well as to investigate the influence (dependence) of K^2 on the gas sensitive layer using the following two SAW structures: $\text{In}_2\text{O}_3/\text{Si}_3\text{N}_4/36^\circ\text{YXLiTaO}_3$ and $\text{In}_2\text{O}_3/\text{PEVCDSi}_3\text{N}_4/36^\circ\text{YXLiTaO}_3$.

For the investigation the most suitable thickness of the gas sensitive layer the intermediate layers thicknesses was kept at 1 μm whilst the indium oxide layer thickness was varied. It was found (Figure 3.4) that for the highest K^2 the optimal thickness should be around 1.2 μm for the $\text{In}_2\text{O}_3/\text{PEVCDSi}_3\text{N}_4/36^\circ\text{YXLiTaO}_3$ structure and for $\text{In}_2\text{O}_3/\text{Si}_3\text{N}_4/36^\circ\text{YXLiTaO}_3$ this should be around 2.0 μm . The deposition of such thick layers of In_2O_3 is unsuitable not only from a gas sensing point of view (thin films are more suitable for ozone sensing than thick films, e.g. have higher sensitivity, faster response and recovery time) but also from a fabrication point of view it is not appropriate. The r.f. sputtering used for this thesis requires at least four-hour deposition duration. A metallic target with a low melting point such as indium may not endure such a long sputtering process (more details on the fabrication parameters can be found in chapter 4).

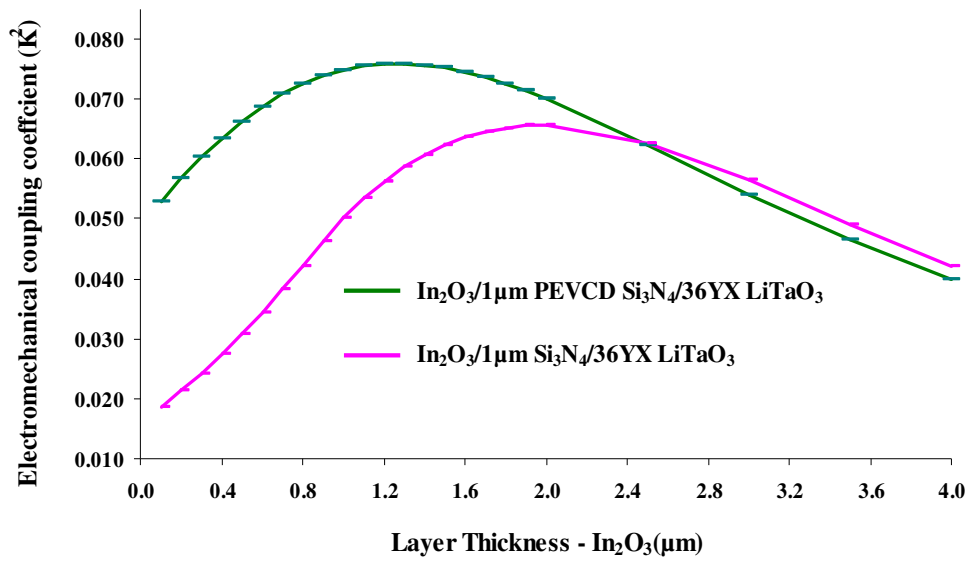


Figure 3.4 Electromechanical coupling coefficient (K^2) changes versus In_2O_3 layer thickness for the $\text{In}_2\text{O}_3/1\mu\text{mSi}_3\text{N}_4/36^\circ\text{YXLiTaO}_3$ and $\text{In}_2\text{O}_3/1\mu\text{mPEVCDSi}_3\text{N}_4/36^\circ\text{YXLiTaO}_3$ structures

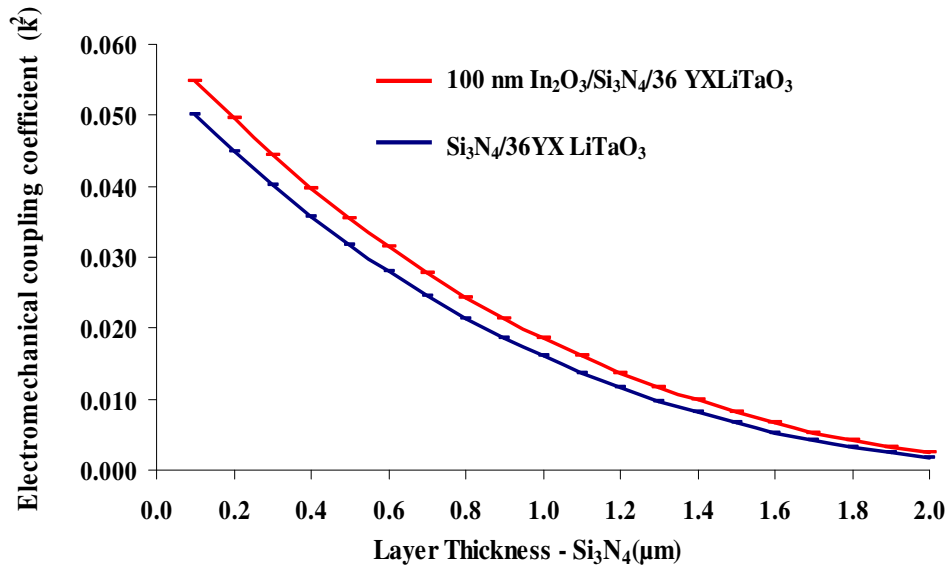


Figure 3.5 Electromechanical coupling coefficient (K^2) changes versus Si_3N_4 layer thickness of the $\text{Si}_3\text{N}_4/36^\circ\text{YXLiTaO}_3$ SAW structure with and without a 100 nm In_2O_3 gas sensitive layer

To investigate K^2 dependence on the sensitive layer, the indium oxide layer thickness was kept constant at 100 nm and the thicknesses of the intermediate layers was varied. Figure 3.5 above and Figure 3.6 below show the simulation results for both SAW structures. It was found that the K^2 of the both structures increased by the addition of 100 nm indium oxide layer.

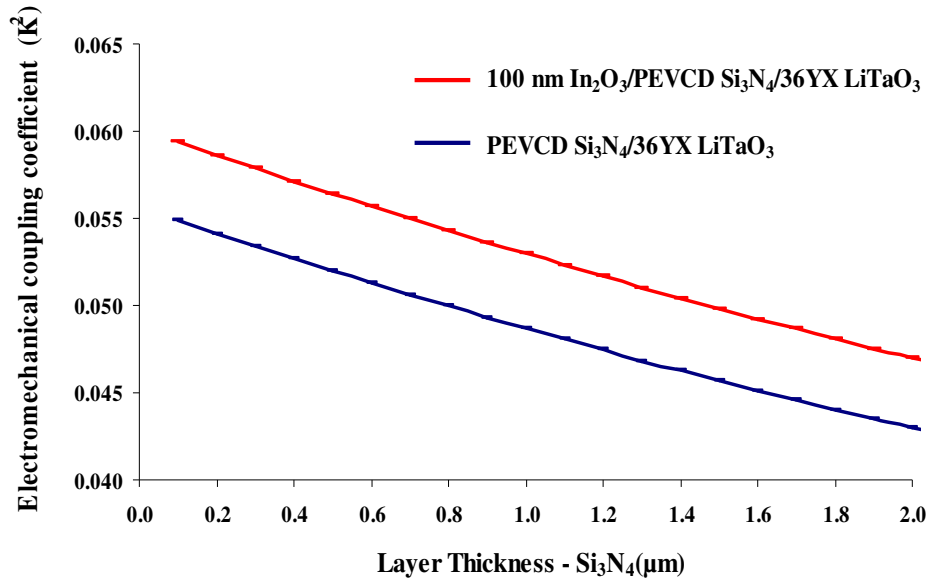


Figure 3.6 Electromechanical coupling coefficient (K^2) changes versus Si₃N₄ layer thickness for the PECVD Si₃N₄/36°YXLiTaO₃ SAW structure with and without a 100 nm In₂O₃ sensing layer

Calculation of the sheet conductivity of the gas sensitive layer

As previously was presented (acoustoelectric effect, Figure 3.1), if the appropriate thicknesses of the intermediate and sensitive layer are selected (e.g. a high K^2 value), the critical sheet conductivity σ_{or} of the gas sensitive layer will be matched with the velocity permittivity product of the SAW mode (e.g. substrate/intermediate layer structure).

The author used the K^2 obtained by previous simulations for the calculations of sensitivity. Figure 3.7 shows the variation of the fractional change in frequency versus the sensitive layer sheet conductivity for a SAW structure when a 1 μm thick Si_3N_4 intermediate layer was utilised.

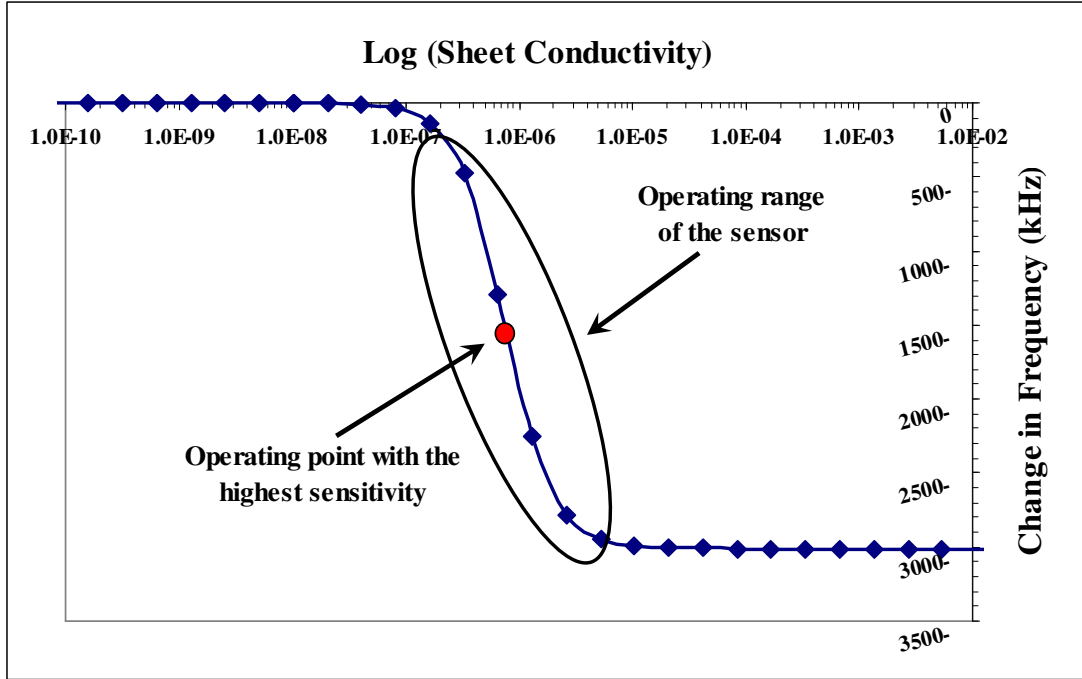


Figure 3.7 Calculated change in frequency shift of a $\text{Si}_3\text{N}_4/36^\circ\text{YXLiTaO}_3$ SAW structure as a function of a sheet conductivity of the indium oxide sensitive layer. For calculations, the K^2 value of the 1 μm thick Si_3N_4 intermediate layer and the periodicity of $\lambda = 24 \mu\text{m}$ at the substrate were used

The operating range and operating point with the highest sensitivity are also shown in Figure 3.7 where the sheet conductivity of the indium oxide layer is optimum for a highly sensitive SAW based device. In this operating range the SAW device is very sensitive to the surface perturbations (e.g. has a high K^2 value, large response magnitudes) and if it is combined with a suitable gas sensitive thin layer a highly sensitive SAW device for the

targeted gas analytes (e.g. reducing and oxidising gases) will be obtained. In the flat part of the curve very little frequency shift will be recorded.

For the calculation of the sheet conductivity $\sigma_{sh} = v_p C_s$ of the surface layer it is necessary to evaluate the permittivities of the SAW structures. The permittivities were obtained in two steps by using the method reported by Bløktæjer et al. [121]:

$$\varepsilon_p(k) = \varepsilon_{1p} \frac{\varepsilon_{1p} \tanh(k_0 h_1) + \varepsilon_{2p}}{\varepsilon_{2p} \tanh(k_0 h_1) + \varepsilon_{1p}} \quad (3.17)$$

In the first step, it was considered that ε_{1p} and ε_{2p} is the permittivity of the Si_3N_4 layer and of the semi-infinite substrate, respectively. The permittivity $\varepsilon_p(k)$ of the $\text{Si}_3\text{N}_4/36^\circ\text{YXLiTaO}_3$ structure was calculated for thicknesses of (h_1) between 0.1 and 4 μm .

In the second step, it was considered that the obtained $\varepsilon_p(k)$ value of the $\text{Si}_3\text{N}_4/36^\circ\text{YXLiTaO}_3$ structure obtained in the first step to be ε_{1p} in equation (3.17) and the indium oxide permittivity to be ε_{2p} . The permittivity values $\varepsilon_{pf}(k)$ of the entire layered SAW structure. were evaluated again for thicknesses between 0.1 and 4 μm of Si_3N_4 when the indium oxide layer thickness was kept constant at 100 nm. Finally to obtain the sheet conductivity of the thin surface oxide layer, the velocity permittivity product formula was used:

$$\sigma_{sh} = v_p (\varepsilon_{pf} + \varepsilon_0) \quad (3.18)$$

Figure 3.8 shows the variation of the calculated sheet conductivity of the indium oxide layer with the change of the thicknesses of the intermediate layer. It can be seen the sheet conductivity has only a small variation between $9.94 \times 10^{-7} \Omega^{-1} \text{ m}^{-1}$ and $7.27 \times 10^{-7} \Omega^{-1} \text{ m}^{-1}$ for the thicknesses between 0.5 and 1.0 μm .

This illustrates that the author's decision to select the thickness of 1.0 μm for the intermediate layer was justified (trade off based on the simulation and experimental work). The obtained sheet conductivity for this thickness is within the operating range of the layered SAW sensor as indicated in Figure 3.7.

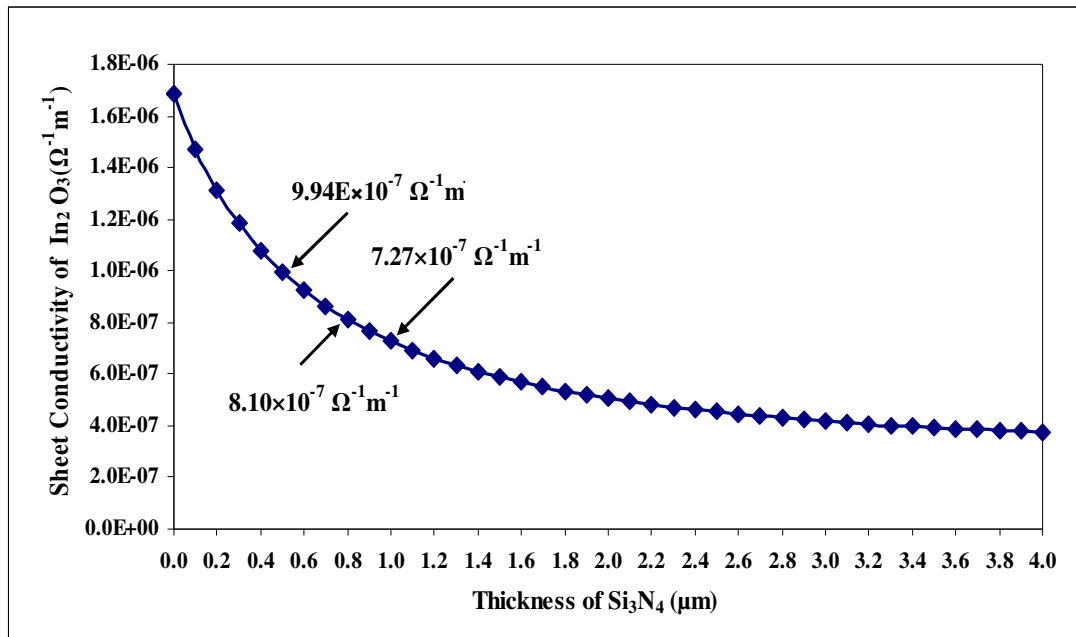


Figure 3 8 Variation of the sensitive 100 nm thin indium oxide layer sheet conductivity with the change of the intermediate layer thicknesses.

Furthermore, the calculated value is in agreement with the measured values of the sheet conductivity (details can be found in Chapter 6) for the indium oxide films of the developed layered SAW sensors shown in Table 3.1.

Table 3.1 Comparison of the calculated and measured sheet conductivity of the indium oxide sensitive layers of a SAW based gas sensor

Sample # SAW sensor	Intermediate layer thickness and deposition method	Extrapolated carrier concentrations $n(\text{cm}^3)$	Measured sheet conductivity $\sigma_{\text{sh}} (\Omega^{-1}\text{cm}^{-1})$	Calculated sheet conductivity $\sigma_{\text{sh}} (\Omega^{-1}\text{cm}^{-1})$
EF01	PECVD ($\text{SiO}_2/\text{SiN}_x$)	5.80×10^{-16}	8.33×10^{-6}	7.27×10^{-7}
EF12	E-beam Evaporation (SiN_x)	5.80×10^{-15}	8.70×10^{-7}	
EF08	R.f. sputtering (SiO_xN_y)	3.50×10^{-15}	5.85×10^{-7}	

The only exception is for the SAW sensor with the PECVD intermediate layer (sample EF01). This can be explained by the fact that the carrier concentrations of this layer is also very different compared to the other two layers as well that there is also a thin SiO_2 layer between the sensitive and silicon nitride intermediate layer. The formation and origin of this layer is explained in Chapter 6.

3.3 SMO Gas Sensing Mechanism

A change in the electrical conductivity of SMO (e.g. InO_x) gas sensor is measured as a function of gas concentration. When a semiconductor based sensor is exposed to a gas mixture environment, which contains an oxygen component, the defect chemistry of the oxide is perturbed [122]. This affects the electrical conductivity in the presence of the ambient oxygen partial pressure $p(\text{O}_2)$. In general, the relation between conductivity σ and the oxygen partial pressure $p(\text{O}_2)$ can be written as [5]:

$$\sigma = \sigma_0 \exp\left(\frac{-E_A}{k_B}\right) p(\text{O}_2)^{\pm \frac{1}{m}} \quad (3.19)$$

where k_B is the Boltzmann's constant, T is the temperature in degrees Kelvin, E_A is the activation energy, σ_0 is a factor that includes the bulk intergranular conductance, and m is a factor related to the oxygen sensitivity, which depends on the nature of point defects when oxygen is removed from the lattice. Therefore, it can be seen that the conductivity of SMO is dependent on temperature and has also a useful dependence of $p(O_2)$. The positive and negative signs of $1/m$ in equation (3.19) indicate p-type or n-type conduction, correspondingly.

There are two different classes of operating mechanisms in SMO gas sensors:

A) One involves changes in *bulk conductance*. The sensors based on this mechanism are strongly sensitive to the changes in $p(O_2)$ [122]. The oxide defect chemistry controls the sensor behaviour as the bulk has a tendency towards equilibration with ambient oxygen pressure.

B) The second class of mechanism is the *surface conductance*, which is a result of surface charge-exchange process with the ambient gaseous component adsorbed on the surface of the active layer.

Type of Adsorptions

When the target gas analyte reaches the SAW sensor it adsorbs to the sensor surface. It then diffuses in the bulk of the coating before it returns to the surface and subsequently desorbs. The rate of adsorption, diffusion and desorption is dependent on the temperature, the coating properties (e.g. thickness, porosity), surface area for adsorption, analyte gas concentration and

surface density of the active site [106]. There are two major types of adsorptions: *physiosorption* and *chemisorptions*.

Physiosorption is a physical adsorption in which the adsorbate adheres to the surface only through weak physical interactions, such as Van der Waals force. It is characterised by a low temperature (under the critical temperature of the adsorbate) and also by a low activation energy and enthalpy ($\Delta H < 40 \text{ KJ/mol-1}$ of adsorbate) [123]. For sensors using rigid, porous films, e.g. obtained by sol-gel deposition method, the responses can be entirely described by physiosorption process [106].

Chemisorption or chemical adsorption is when molecules adhere to a surface through the formation of a chemical bond. This is a strong covalent bond between adsorbate and surface molecules. It is characterised by lower temperature and higher pressure than physiosorption, as well as high activation energy and enthalpy ($50 \text{ kJ/mol} < \Delta H < 800 \text{ kJ/mol-1}$ of adsorbate). Adsorption takes place only in the surface monolayer and is reversible only at high temperatures [123]. Examples of this process are the dissociative adsorption processes in surface metal oxides and the binding of water to such surfaces [106].

It is believed that on the surface of the thin indium oxide layer *chemisorption* takes place when it is exposed to the gas analytes (O_3 and H_2) [120]. In the absence of any humidity and in the presence of oxygen the adsorption of the gas molecules on the surface of the indium oxide induces a change in the conductivity of the thin film. With increasing temperature the density of chemisorbed species increases too but at higher temperatures than 600°C the formation of various surface and bulk defects within the semiconductor metal oxide lattice occurs [5]. Therefore, it can be stated that the surface conduction mechanism is characterised

by chemisorption at temperature less than 600°C and by bulk conduction at higher temperatures than 600°C (by the formation of volume defects).

In the case of chemisorptions, depending on the ambient temperature the oxygen absorbents are predominantly O_2^- ions below 150°C, O^- between 150°C and 400°C and above 400°C are in the form of O^{2-} which are incorporated in the lattice [122]. The sensors developed in this research work only operated between 135°C and 310°C and therefore it is understood that O_2^- and O^- ions are present on the surface and responsible for the sensors' responses.

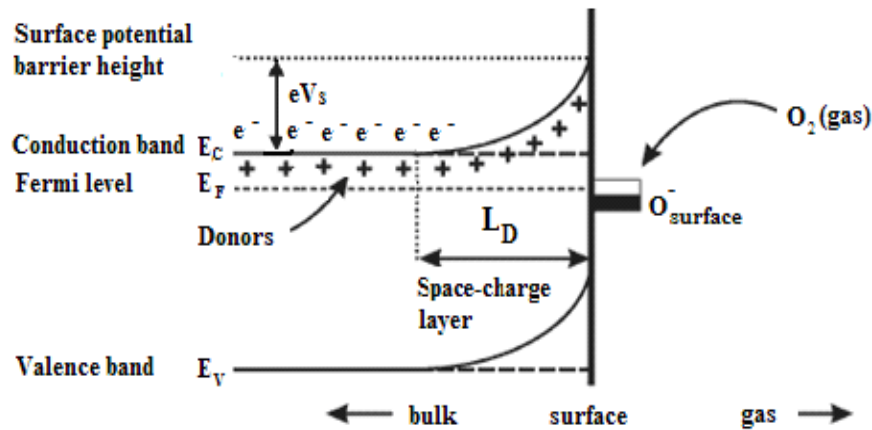


Figure 3 9 Model of band bending in a semiconductor after chemisorption of oxygen on the surface sites (adapted and redrawn from [124])

In the case of *n-type semiconductor metal oxides* (e.g. InO_x or SnO_2) the formation of these oxygen absorbents build a space - charge layer at the surface of the metal oxide grains, leading to an electron - depleted surface region (Figure 3.9). The required electrons for this

process are coming from donor sites (\oplus indicates a donor site in figure 3.9) and are extracted from the conduction band (E_C).

The space charge layer (L_D) can be defined as follows [5,125]:

$$L_D = \sqrt{\frac{2 K \epsilon_0 \Delta \phi_s}{e N_D}} \quad (3.20)$$

where N_D are the surface charge and the number of ionised donor states per unit volume , K is the static dielectric constant, ϵ_0 is the permittivity of free space, e is the electron charge and $\Delta \phi_s = e V_s$ the surface potential barrier height. As indicated in Figure 3.10 the surface potential barrier (V_s) and thickness (L_D) of the depletion region depends on the amount of adsorbed oxygen.

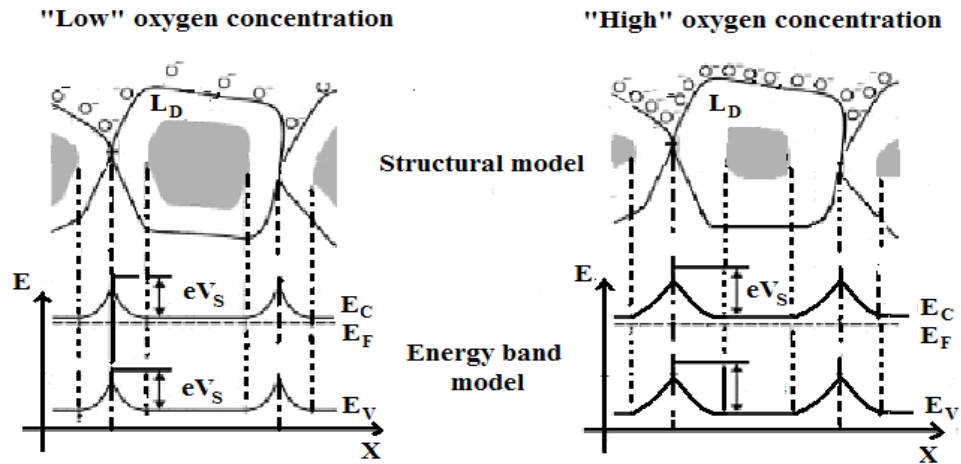


Figure 3.10 Structural and band model showing the intergranular contact regions for a polycrystalline semiconductor metal oxide in an: (a) relatively low oxygen concentration and (b) higher ambient oxygen concentration) (redrawn and modified from [124])

Non-Stoichiometry of indium oxide

As the surface conductance mechanism is influenced by the SMO material's non-stoichiometric composition, the non-stoichiometry of indium oxides will be discussed. The chemical formulas for oxides and inorganic compounds are usually written to indicate that there is a definite ratio of cations to anions in the compound, e.g. M_aO_b , where a and b are usually small integers determined by the valency of constituents atoms. When the oxide M_aO_b does contain M and O atoms in the exact ratio a/b , it is said to have a stoichiometric composition. However numerous metal oxides exhibits marked deviation from stoichiometry. In a compound, non-stoichiometry is equivalent to the presence of point defects in the crystal lattice compared to the stoichiometric conditions and the extent of nonstoichiometry is measured by the net concentration of the corresponding defects. Formation or annihilation of these defects can only take place at surfaces exposed to the ambient gas atmosphere, or in concurrence with a higher or lower oxide or metal (e.g. at metal/oxide interface of an oxide film) [7].

Non-stoichiometry in metal oxides can be of two main types with respect to stoichiometric composition [7]:

1. *Oxygen deficient (or excess metal)* - the main defects can be either oxygen vacancies or interstitial metal ions (excess metal), both of these defects lead to the formation of complimentary free electrons. Therefore the conductivity is due to the transport of electrons and oxygen deficient oxides are characterised by n-type conductivity.
2. *Metal deficient (or excess oxygen)* - the predominant defects can be either metal vacancies or interstitial oxygen atoms (excess oxygen). The formation of charged metal ion vacancies leads to the formation of complimentary positive (charge carriers,

holes). Therefore the conductivity involves the transport of holes and metal deficient oxides are characterised by p-type conductivity [7].

Indium oxide in stoichiometric form is an insulator and in non-stoichiometric form is an n-type semiconductor material suitable for gas sensing applications [31]. In an indium oxide film an oxygen deficiency is observed mainly in the form of *oxygen vacancies* [126]. These act as doubly charged donors providing electrons to the conduction band. However, it has also been reported that indium oxide films oxygen deficient non-stoichiometry might be due to the presence of excess indium compared to the stoichiometric composition [127]. In this case, the dominant defects are interstitial In^{3+} cations but the possible contributions of these defects to the conductivity are low. Therefore, it can be stated that the main contributors to the conductivity of the oxygen deficient non-stoichiometric indium oxide films are the *oxygen vacancies*.

3.4 Gas Sensitive Layer Morphology

The sensing mechanism can take place at different sites of this layer depending on the SMO layer's morphology, which can be divided into [128]:

- **Compact layer:** the gases cannot penetrate into the layer, so the interaction takes place at the geometric surface of the sensitive layer (Figure 3.11 a).
- **Porous layer:** the gases can access more surface area within the volume of the sensitive layer (Figure 3.11 b). The active surface in this case is much larger than the geometric one; the gas interaction can take place at the surface of the individual

grains, at the grain-grain boundaries and at the interface between grains and electrodes.)

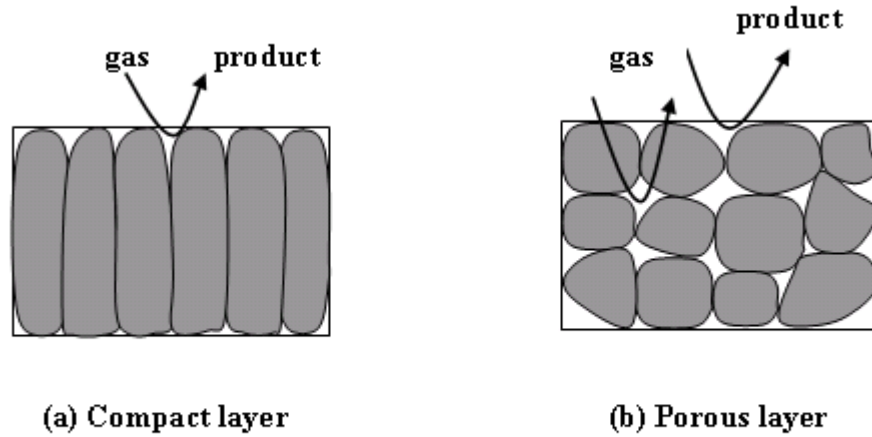


Figure 3.11 Schematic cross-section views showing gas interaction in: (a) Compact and (b) Porous metal oxide layers [128]

3.4.1 Compact Layer

A compact SMO sensitive layer may be either *partly depleted layer* (Figure 3.12) *completely depleted layer* depending on the ratio between the film thickness (Z_g) and the thickness of the depleted layer (Z_0), as shown in Figure 3.12 b.

For a *partly depleted sensing layer* ($Z_g > Z_0$) the surface reactions do not influence the electrical conduction in the entire layer, conduction can take place in the bulk region. Two resistances occur in parallel in this case: one is influenced by the surface reactions, layer Z_0 with a higher resistance value and the other one, by the $(Z_g - Z_0)$ layer, and has the bulk resistance value. The entire partly depleted SMO layer is considered a conductive layer with a gas reaction dependent thickness.

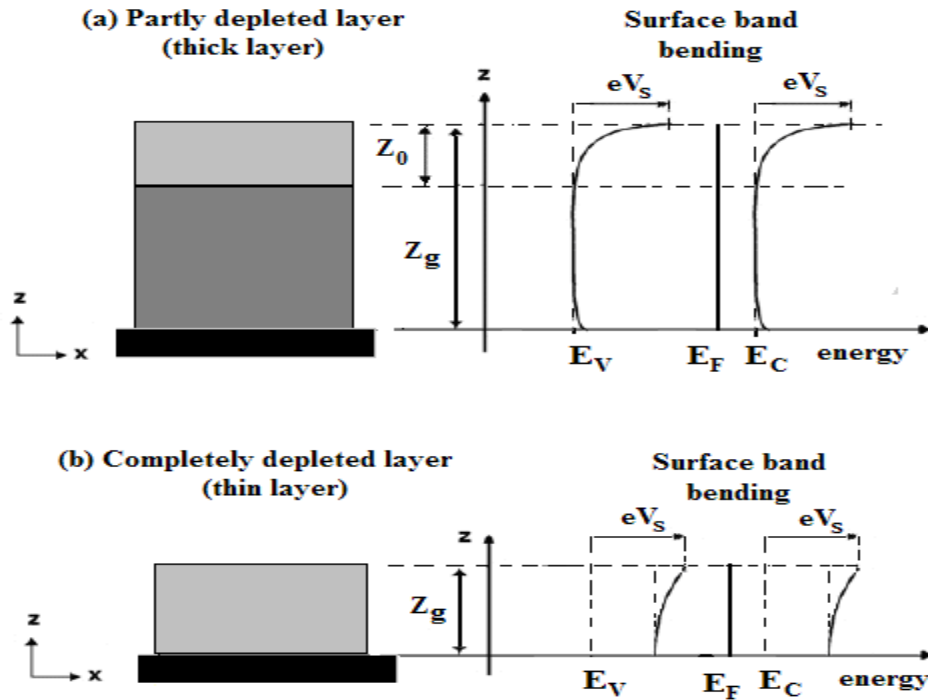


Figure 3.12 Schematic representation of a compact layer with energy band representations showing: (a) Partly depleted compact layer and (b) Completely depleted compact layer (redrawn and modified from [128]).

In the case of *completely depleted layer* the exposure to reducing gases can act as a switch to the partly depleted layer due to the contribution of additional free carriers. It is also possible that exposure to the oxidizing gases acts as a switch between partly depleted and completely depleted layer. Further details can be found in [129].

3.4.2 Porous Layer

In a porous sensing layer, due to the presence of necks formed by adjacent grains, it is possible to have (for large necks $Z_n > Z_0$, where Z_n is the neck diameter) a *surface/bulk contribution*.

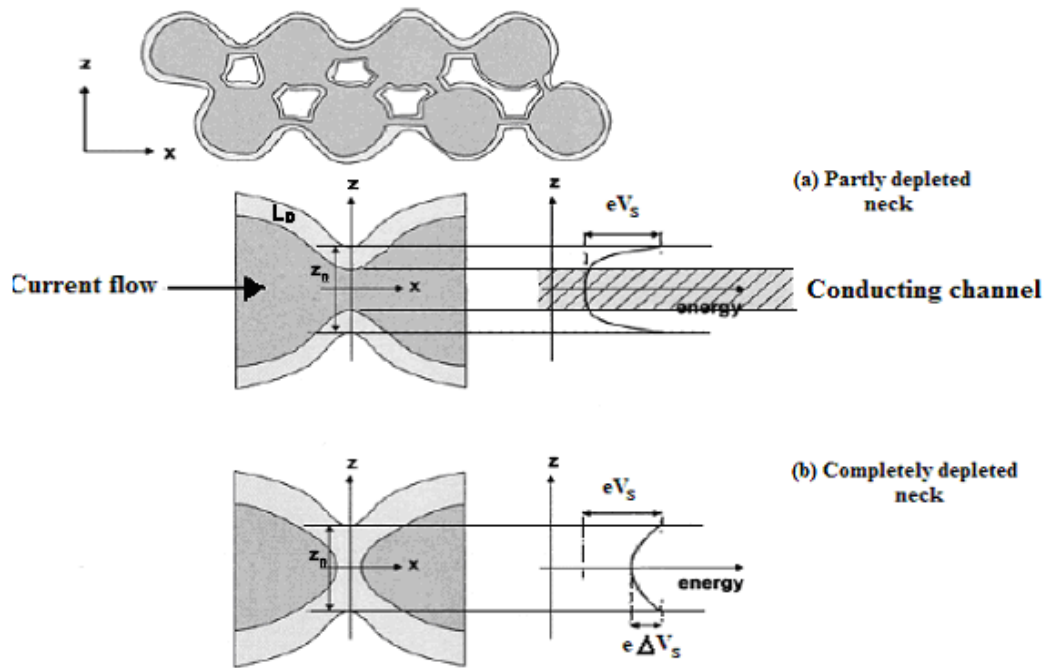


Figure 3.13 Schematic representation of a porous layer showing geometry and surface energy band diagram for necks between grains: (a) represent a partly depleted neck and (b) is when the neck contact is completely depleted [128]

For large grains a *grain boundary* and for small grains and small necks *flat bands contributions* are possible. A discussion on the “*flat band condition*” is included in the next section. The necks in a porous layer can be partly or completely depleted. As in the compact layer it is also possible for porous layers to have a switching role for the reducing and oxidizing gases since the depletion layer of the neck contact is influenced by the ambient atmosphere [128].

3.5 Grain Size Effect on the Sensitivity of SMO Gas Sensors

One of the most important factors which influence the sensitivity of polycrystalline SMO layers (or films) is the mean diameter of grains or crystallites (X_g) [79, 130].

It has been shown that by decreasing X_g the sensitivity increases [130,131]. Three grain size effects models were proposed assuming that a layer is composed of a chain of uniform crystallites of size X_g connected with each other through necks and grain boundary contacts, shown in Figure 3.14, where R_N and R_{GB} are the neck and grain boundary resistances and X is the width of the necks (non-depleted region).

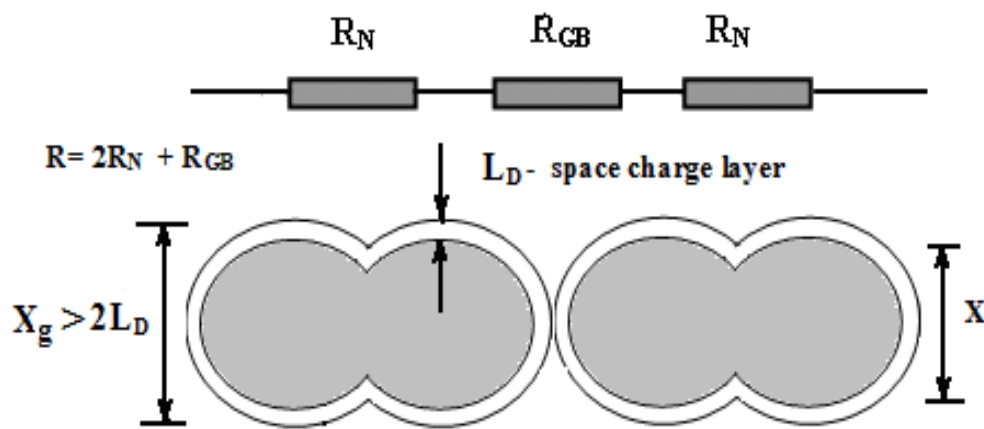


Figure 3.14 Schematic representations of neck and grain boundary and resistance distribution [132]

The three grain-size effect models proposed in conjunction with the space charge layer depth (L_D) [79,130] are:

- $X_g \gg 2L_D$ grain boundary control
- $X_g \leq 2L_D$ neck control
- $X_g \ll 2L_D$ grain control

For SMO materials the grain size is much larger than twice the space charge layer depth ($X_g \gg 2L_D$), so the grain boundary control mechanism is responsible for the electrical conduction. It was found that the sensitivity can be enhanced considerably when X_g becomes smaller than $2L_D$, due to the complete depletion of the grains, so for gas sensing the grain control ($X_g \ll 2L_D$) is the most preferable.

For an n-type semiconductor material, if $X_g \gg 2L_D$ the carriers (electrons) must overcome the potential barrier of eV_s of the adjacent grains. The interaction of the captured electrons with the adsorbed oxygen results in a change of V_s . In this case the conductance (G) of the sensing material is proportional to [124]:

$$G = G_0 \exp\left(\frac{-eV_s}{k_B T}\right), \quad (3.22)$$

where G_0 is proportionality constant. When the grain or particle size is reduced in such a way that the $X_g \ll 2L_D$ the depleted regions start to overlap and the surface barriers of the individual grains fall below the thermal energy ($k_B T$) resulting in the so called the "flat band conditions". In this case, the energetic difference, between the Fermi level and conduction band disappears and the conductance is proportional to the difference between the Fermi level (E_F) and conduction E_C band [124]:

$$G = G_0 \exp\left(\frac{-(E_C - E_F)}{k_B T}\right) \quad (3.23)$$

The oxygen adsorption under these conditions will result in grains being completely depleted of conduction band electrons and as a consequence an increased variation in resistance will be obtained. Therefore, SMO materials with nanosized grains or nanocrystalline materials have significant potential to be used to produce highly sensitive gas sensors [79]. As a result the author has utilised nanostructured SMO thin films as gas sensitive layers.

3.5.1 Grain Size effect on the Sensitivity of an Indium Oxide based Gas

Sensor

The grain size of the indium oxide films is one of the most essential parameters in controlling gas sensing characteristics (e.g. magnitude and response time) [118,87]. By reducing the grain sizes significant improvement in the operating characteristics of the indium oxide based gas sensors can be achieved [118,132].

If the grain size is decreased from 60-80 nm to 10-15 nm the indium oxide gas sensor's responses towards ozone can be increased 100-1000 times [118] and the response time can be decreased by 50-100 times at the operating temperature of 300° C.

Gurlo et al. [133] have also showed (Figure 3.15) that if the grain size of the indium oxide film is reduced to less than 50 nm the response magnitude for NO₂ increases exponentially. The indium oxide thin films deposited by the author have estimated grain sizes between 30 and 40 nm (details can be found in chapter 6).

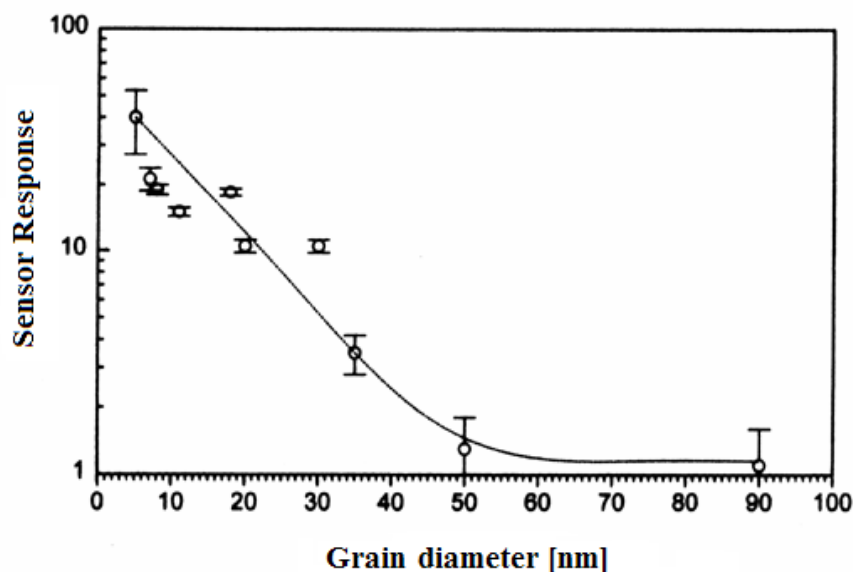


Figure 3.15 The effect of In_2O_3 thin film grain size on the In_2O_3 sensor response towards NO_2 (from [133])

Another important parameter for gas sensing is the film's texture. It was established that the preferred orientation of homogeneous ZnO films alters the electrical resistance at room temperature [119]. For an indium oxide film the degree of texture, defined as the ratio of the main XRD peaks, the (400) planes intensity (I) of (400) and (222), $[I(400)/I(222)]$, increases with the film thickness as shown in Figure 3.16 [119]. For ozone sensing an indium oxide based sensor recovery time will increase as the film's degree of texture increases. The ratio of $I(400)/I(222)$ for the as deposited r.f. sputtered indium oxide films deposited by the author was 4.92 and for the annealed film was 6.95, which is in agreement with the values published in the literature [119] and shown in Figure 3.17. This value of 6.95 indicates that the r.f. sputtered indium oxide films have a preferential orientation, which will be discussed in the Chapter 6.

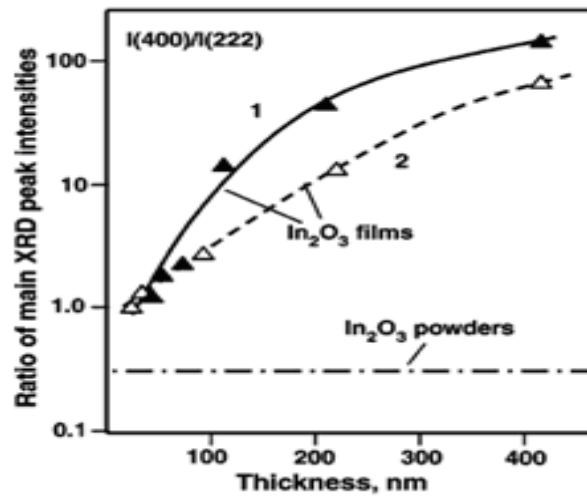


Figure 3.16 The influence of film thickness on the ratio of main XRD peak intensities for an indium oxide film deposited by spray pyrolysis [119].

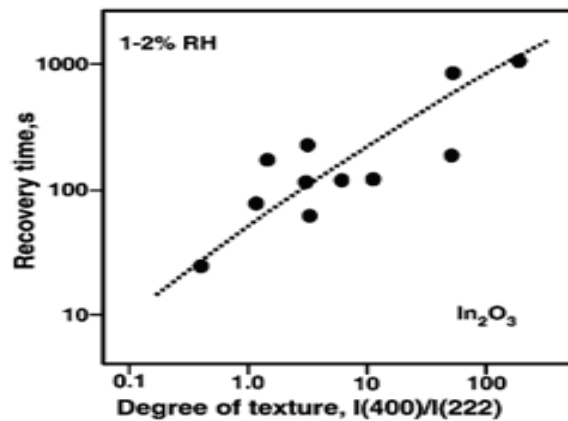


Figure 3.17 The influence of the indium oxide film texture on the recovery time for ozone sensing [119].

3.6 Summary

In this chapter the SAW based device operation principles as well as the conductometric layered SAW sensor were presented. The method utilised by the author for the selection of the intermediate and sensing layer thickness was also described. The grain size effect on the sensitivity of an SMO based sensor was presented, and the advantage

utilising a nanostructured thin films as gas sensitive layer was described. The author undertook these investigations in the application of nanostructured SMO sensitive layers for gas sensing applications.

The design of a SAW based gas sensor has a high degree of complexity since one has to take into consideration that not only the semiconductor metal oxide sensitive layer characteristics but also the design of a highly sensitive SAW transducer. For a semiconductor metal oxide sensitive layer, there are many factors that has to be considered, such as thickness, grain size, surface geometry, film texture and surface stoichiometry. For a highly sensitive layered SAW device the choice of substrate, crystallographic cut, IDT geometry, K^2 , intermediate layer thickness and stoichiometry are some of the factors that have to be considered. Controlling these parameters simultaneously is a very challenging task that a sensor engineer is faced in the design process. Therefore, a trade-off between these different factors should be applied in order to achieve the main goal.

In this design the author has applied a trade off between the thickness and K^2 value. The simulation results and the experimental results were taken into considerations in order to choose the most appropriate thicknesses of the intermediate and sensitive layers.

Chapter 4

Layered SAW Gas Sensor Fabrication

This chapter describes the steps used in the fabrication of the layered SAW sensors investigated during this research program. These include the patterning process for the metal electrodes to form interdigitated transducers (IDTs) as well as the deposition processes for the intermediate and gas sensitive layers. Additionally the frequency responses of a layered SAW device at different stages of fabrication are presented.

Two main methods are used to fabricate thin film electrodes on a flat polished substrate. These are *lift-off* and *etching*. In this work wet chemical etching was used to fabricate aluminium/chromium electrodes on a 36°YXLiTaO_3 piezoelectric substrate. This method utilizes an ultra violet (UV) sensitive, positive photoresist and a photolithographic mask. During developing of positive photoresist, it is removed in places where it was exposed

through a mask to UV light. Using the patterned photoresist the underlying metal was etched in the regions unprotected by the photoresist, thereby realising the desired pattern. Subsequent to etching the photoresist is removed, finalising the fabrication of the IDTs.

For deposition of the silicon nitride intermediate layer, planar r.f magnetron sputtering, PECVD and E-beam evaporation were used. InO_x thin films were deposited as gas sensitive layers by r.f. magnetron sputtering and layers of SnO_2 nanorods by PECVD. Physical vapour evaporation of metal oxide nanopowders was used to synthesize indium oxide nanowires and nanobelts on silicon substrates.

4.1 SAW Transducer Fabrication Procedure

The fabrication of the metal electrodes (IDTs) consists of four stages: sample preparation, metal evaporation, photolithography and wet chemical etching.

4.1.1 Sample Preparation

Single side polished, 500 μm thick, 36° rotated Y-cut, X-propagating LiTaO_3 wafers were diced into 7.5 mm \times 11 mm pieces using a diamond saw. After dicing, the samples were cleaned thoroughly to remove particles and impurities from the surface. The cleaning of the samples is a very important part of the fabrication procedure in order to obtain good adhesion and uniform coatings of the metallic films. The process began with an acetone rinse, followed by isopropanol and deionised (DI) water and after drying with compressed filtered nitrogen the cleaning process continued by immersing the samples in AZ-100 remover solution. The samples were baked for 20 minutes at 80°C in this solution and finally, after a 10 minute cooling period, they were rinsed again in acetone, isopropanol and DI water.

4.1.2 Thin Film Metal Evaporation

The cleaning procedure was followed by metal evaporation. A BalzersTM E-beam evaporator was used to deposit the metal layers for the IDT structure. A 300 Å layer of Cr followed by a 2500 Å layer of Al were deposited on the polished side of the LiTaO₃ wafer. The Al provides good electric coupling to the substrate, it is a light metal and bonds well to Cr. The purpose of the Cr layer is to provide good adhesion for the Al layer to the substrate. The E-Beam evaporator was set at the beam voltage of 10 keV and the chamber pressure before evaporation was 1×10^{-7} Torr. The beam current was 100 mA, which yielded a deposition rate of 2 Å sec⁻¹.

4.1.3 Photolithography

AZ-1512 positive photoresist supplied by Clariant was spun on the samples at 3000 rpm for 40 seconds forming a 1µm thick layer. The samples were baked in an oven at 90°C for 20 minutes to remove any remaining photoresist solvent. A contact mask aligner (Karl-Süss MJB-3) was employed to align and expose the photoresist-coated samples. It is very important to align the IDT patterns with specific crystallographic planes of the substrate to obtain a propagation of the SAW in the intended direction. The mask was aligned in a way to create a SAW propagating along the crystallographic X-direction (Figure 4.1). After alignment each sample was exposed to UV light for 8-10 seconds (corresponding to a UV exposure energy dose of 60 mJ/cm²) which was sufficient to fully expose the photoresist where required. The exposed samples were developed using an alkaline solution AZ-400K: DI (1:4). The photoresist developing time was between 18 and 20 seconds. After development, samples were post baked for 20 minutes at 110°C.

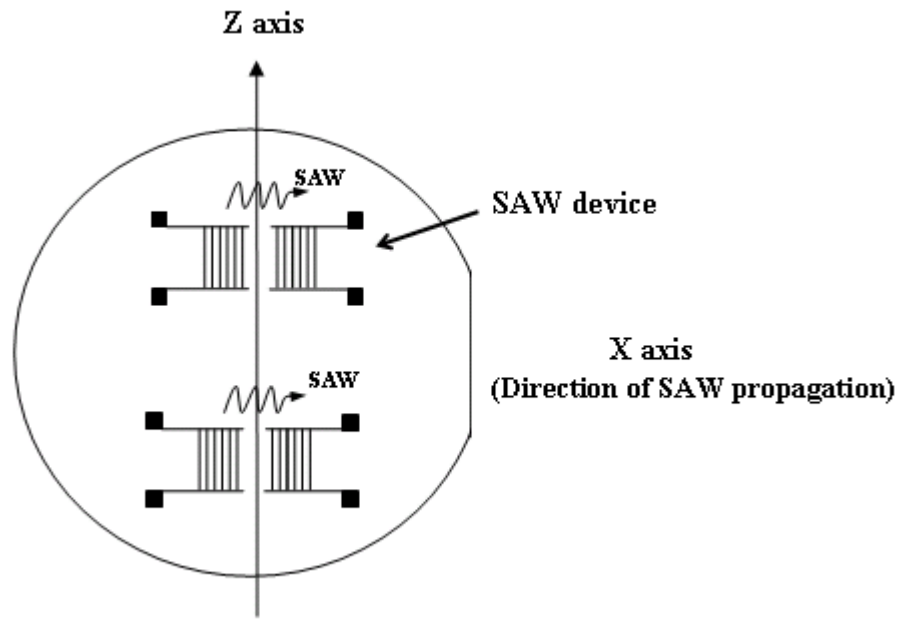


Figure 4.1 Orientation of a 36°YX LiTaO₃ wafer and two SAW delay line devices.
A LSAW propagates along the X direction.

4.1.4 Chemical Etching

Wet etching was used to remove the unwanted regions of Al/Cr. The Al was etched using the same alkaline solution of AZ-400K : DI (1:4) used before for developing. The Cr was etched in a solution composed of 50g ceric ammonium nitrate and 400 ml nitric acid and 500 ml of DI water ((NH₄)₂[Ce(NO₃)₆] / HClO₄). The etching time of the Al and Cr was varied between 5 and 7 minutes and 30 and 40 seconds respectively in order to obtain the IDT patterns with uniform width electrode fingers. Etching time is critical as any over-etching will result in a decrease in the width of the IDT fingers. After etching, the samples were immersed in a solution of AZ-100 Remover and were baked in an oven at 80°C for 20 minutes. Finally they were soaked in acetone to completely remove the photoresist. A summary of the IDT pattern fabrication process is summarised in Figure 4.2.

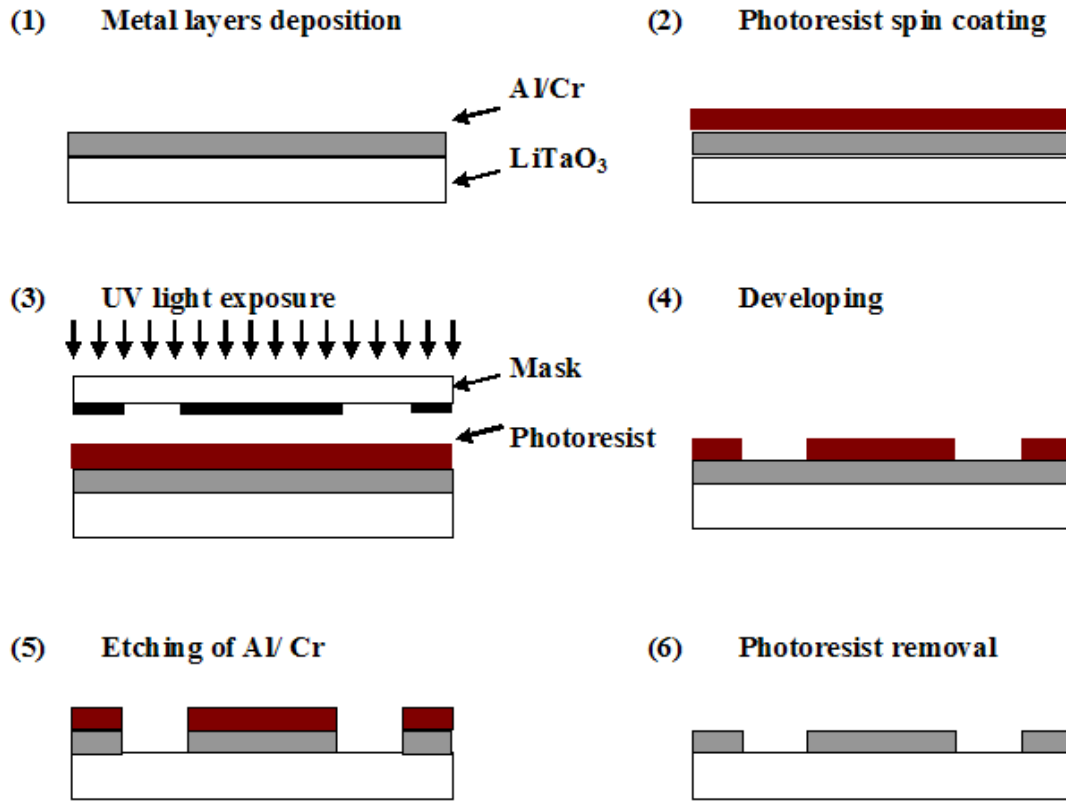


Figure 4.2 Photolithography steps for IDT patterning

Before the deposition of the intermediate and gas sensitive layers of the SAW devices gold wires were bonded to the contact pads for electrical connections using a thermal-ultrasonic wire bonding tool and to strengthen the bonds a silver base epoxy was placed on each bonds. Figure 4.2 (a) shows a magnified photograph and (b) a schematic drawing of the two-port delay line SAW device used in this research program. The device consists of two sets of IDTs with 64 finger pairs each has an aperture width of $W = 1250 \mu\text{m}$ and periodicity of $\lambda = 24 \mu\text{m}$. To decrease the insertion loss the centre-to-centre separation distance of the IDT ports employed was 85λ [29].

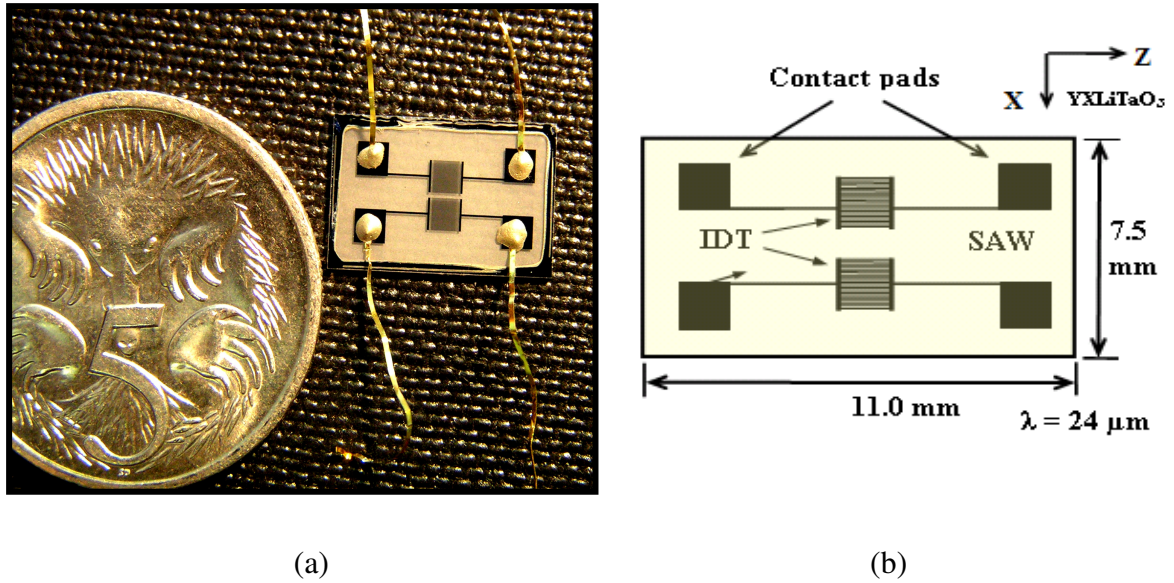


Figure 4.3 Two port delay line SAW device used in this research work: (a) magnified photograph comparing the delay line SAW device with a 5 cent Australian coin, (b) Schematic of the device with dimensions.

4.2 Intermediate and Sensitive Layers Deposition

The next stage in the sensor fabrication is the deposition of the intermediate and gas sensitive layers. Before deposition the samples were thoroughly cleaned following the same procedure described in section 4.1.2. In this section the deposition methods and conditions used for the intermediate and gas sensitive layers will be described.

4.2.1 R.f. Magnetron Sputtering Method

Sputter coating is a physical vapour deposition process used to form thin films on the surface of a substrate. It involves the ejection of atoms from the surface of a target material by bombardment with energetic ions, subsequently depositing the ejected material on the substrate opposite the target [134]. It was developed by Langmuir as a thin film deposition method in the 1920s and presents distinctive advantages when compared to thin film deposition by physical evaporation. It has a better step coverage and far less yields high

deposition rates and excellent adhesion [135]. These advantages make this technique the main alternative to evaporation for metal film deposition in microelectronics fabrication. Sputter coating can be used for depositing a wide variety of materials; for elemental metals d.c. (direct current) sputtering is preferred but when depositing insulating materials (e.g. SiO₂) r.f. sputtering has to be used [134].

Sputter coating uses a glow discharge or plasma, which is a partially ionised gas. Plasma is initiated by applying a large voltage across a gap containing a low pressure gas. Once plasma is generated a stream of ions will bombard the target material ejecting atoms which will be deposited on the substrate opposite the target. Since the ion bombardment will drive the sputtering process it is desirable to find ways to increase their concentrations. There are two widespread methods used to achieve this: (i) magnetron confinement and (ii) electron cyclotron resonance. Since the author has used the first method to deposit the sensor layers the r.f. magnetron sputtering will be discussed in the following. Figure 4.4 presents a schematic of the r.f. magnetron sputtering system utilised by the author. There are two planar electrodes, one of the electrodes is the cathode on which the target material is mounted, the other is the anode, which includes the substrate holder and is electrically grounded.

The magnetic field added to the plasma cause the electrons to spiral around the direction of the magnetic field lines. The Lorentz force (F) at any position of an electron will redirect the motion of the electron in a direction perpendicular to both the electric field and the magnetic field at that position [136]:

$$F = q \, \overline{v} \times \overline{B} \quad (4.1)$$

where F is the force (N), B is the magnetic field (T), q is the electric charge of the particle (C) and v is the instantaneous velocity of the particle (m/s).

The magnetic field causes the electrons accelerated away from the target to be trapped in a spiralling pattern (near the target) and hence increasing the ionisation rate of neutral gas molecules in this part of the gas [135]. This geometry is called a *magnetron*. The higher ion density increases the rate of the ion bombardment of the target compared with sputtering systems that do not have such a magnetic field. In a typical sputtering system the ion densities are 0.0001% and in magnetron systems it is often 0.03% [134].

Figure 4.4 shows that an arrangement of magnets added behind the target creates magnetic field lines concentrated near the surface of the target. A plasma is generated by an r.f. electric field, operating at 13.56 MHz. A tuning network is used to match the impedance between the plasma and the power source. Most of the power in the plasma is dissipated in the form of heat in the target. To avoid excessive heating the target is water cooled. The chamber is evacuated ($\sim 1 \times 10^{-5}$ Torr) and then sputtering gas is introduced into the vacuum chamber giving a pressure of $\sim 1 \times 10^{-2}$ Torr. The electric field strikes the plasma between the anode and cathode. In the magnetron system the electrons then create the highest amount of ionisation of the sputtering gas to occur near the target. The ions formed bombard the target and eject target atoms, (which have significant kinetic energy) and most of them head towards the substrate [135].

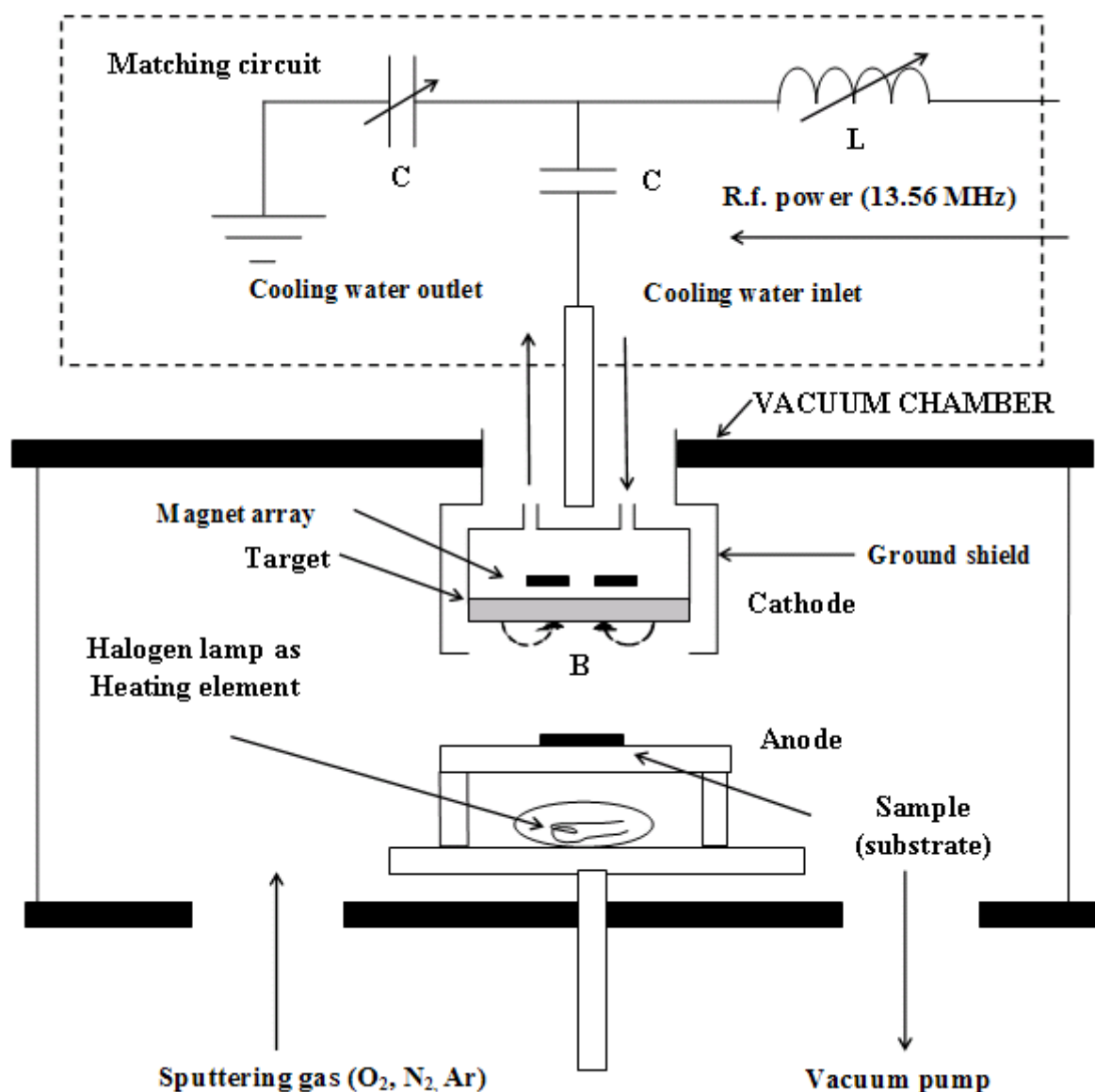


Figure 4.4 Schematic diagram of the r.f. planar magnetron sputtering system used

4.2.1.1 Intermediate Layer Deposition

The author has deposited silicon nitride films with thicknesses between 200 nm and 2500 nm by r.f. magnetron sputtering. A sintered Si₃N₄ ceramic target with purity of 99.99% was used and the sputtering gas was high purity nitrogen (99.999%). During the deposition process the substrate was heated to 120°C by a halogen lamp. Heating the substrate during the deposition process became a crucial factor to successfully deposit suitable SiN_x films. Films

that were deposited without in-situ heating exhibited residual stress fractures and delaminated from their substrates making the SAW devices unusable.

Table 4.1 R.f. magnetron sputtering deposition parameters used for SiN_x layers

PLANAR RF MAGNETRON SPUTTERING	
Vacuum System	Turbo molecular pump backed by a rotary pump
Target	100 mm diameter, 6 mm thick Si ₃ N ₄ ceramic target with 99.9 % purity
Base Pressure	1×10^{-5} Torr
R.f. Power	140 W
Sputtering Gas	Nitrogen (N ₂) with 99.999% purity
Substrate Temperature	120°C
Working Pressure	1×10^{-2} Torr
Distance between the target and samples	2.5 - 3.0 cm
Deposition rate	0.6 μm / hour

The substrate temperature, sputtering rate and the sputtering gases have a strong influence on the compositional properties of the thin films [136]. The thin films obtained by sputtering were amorphous and non-stoichiometric. The microcharacterisation results will be presented in Chapter 6. The sputtered films formed when using substrate heating had a better adhesion to the substrate and no residual fractures were observed. The deposition parameters used to obtain SiN_x film's with good adhesion to the substrate are shown in Table 4.1.

4.2.1.2 Gas Sensitive Layer Deposition

Several deposition methods have been reported for the deposition of indium oxide (In_2O_3 or InO_x) thin films, e.g. d.c. and r.f. sputtering, sol-gel method and spin coating [81-85]. Of these reported methods the sputtering processes have produced the best results giving stable films with good substrate adhesion [85]. The author used the r.f. magnetron sputtering method to deposit InO_x films with thicknesses of 100 nm. The deposition parameters used to deposit InO_x thin films are shown in Table 4.2.

Table 4.2 R.f. magnetron sputtering deposition parameters for InO_x layer

PLANAR RF MAGNETRON SPUTTERING	
Vacuum System	Turbo molecular pump backed by a rotary pump
Target	100 mm diameter, 6 mm thick indium metallic target with 99.999 % purity
Base Pressure	1×10^{-5} Torr
R.f. Power	80 W
Sputtering Gas	90% O_2 / 10% Ar (9:1 ratio)
Substrate Temperature	Room temperature
Working Pressure	1×10^{-2} Torr
Distance between the target and samples	6.5 cm
Deposition rate	0.3 μm / hour

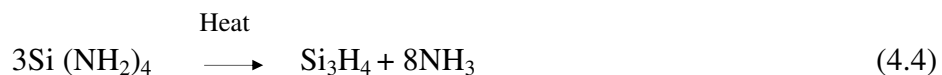
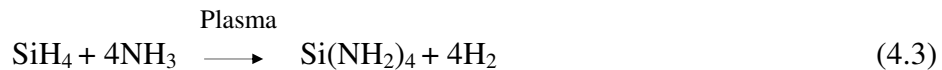
To avoid excessive heating and damage, the indium metallic target was bonded to a copper backing plate. An electrically heat-conducting silver based bonding paste was applied to

adhere the copper plate to the target. The same base and sputtering pressure was used as for the SiN_x deposition. A 99.999% pure indium metallic target was employed. To ensure that a high proportion of ejected indium ions will react with oxygen to form InO_x , a 90% O_2 (the highest available oxygen concentration) and 10% Ar (9:1 ratio) sputtering gas mixture was used.

4.2.2 Plasma Enhanced Chemical Vapour Deposition

For PECVD a plasma source provides the energy needed for chemical reactions to take place which leads to deposition. A plasma supplies additional energy to the reactant gases making possible the reaction for deposition to occur at lower temperatures. This allows easy modification of film properties such as density, stress, composition, and thus to the ability to tailor these properties for particular applications.

A low temperature and pressure PECVD system was used for the deposition of SiN_x intermediate layers. A common gas composition for the deposition of silicon nitride films is silane (SiH_4), ammonia (NH_3) and nitrogen (N_2). The process of low-temperature plasma deposition under ideal conditions involves a two-stage reaction between these gases [137]:



4.2.2.1 Intermediate Layer Deposition

SiN_x with 1 and 2 μm thick layers were deposited by PECVD on single delay line SAW transducers. In the 13.6 MHz Oxford Instruments Plasmalab 80 CVD reactor, SiH_4 and

NH₃ reactive gases and an ultrahigh-purity grade N₂ process gas were introduced to produce the SiN_x films. The deposition parameters for the PECVD of SiN_x layers are presented in

Table 4.3 PECVD parameters used for deposition of SiN_x layers
(SAW devices' intermediate layer)

PLASMA ENHANCED CHEMICAL VAPOUR DEPOSITION	
Deposition system	Oxford Instruments Plasmalab 80 CVD reactor
RF Power	75 W
Base Pressure	10×10^{-3} Torr
Deposition Temperature	125°C
Reactive Gases	Silane (SiH ₄), Ammonia (NH ₃)
Carrier Gas	Nitrogen (N ₂) with purity of 99.999%
Gas Flow Ratio	SiH ₄ /NH ₃ /N ₂ = 1/10/20 (5:50:100 sccm)
Working Pressure	875×10^{-3} Torr
Deposition rate	28 nm/min

4.2.2.2 SnO₂ Nanorod Sensitive Layer Deposition

Thin films of SnO₂ nanorods were deposited on 36° YXLiTaO₃ transducers. The deposition system was a PECVD reactor [138] which used an r.f source of 13.56 MHz and 1.2 kW power was used to generate inductively coupled plasma (ICP). The r.f. source was coupled via a copper tape circling the quartz deposition chamber. Dibutyltin diacetate (Aldrich, 99.999% purity) and (C₄H₉)₂ Sn (OOCCH₃)₂ precursors were held at a temperature of 90°C. The argon

carrier gas was set at a flow rate of 50 sccm and the flow rate of the reaction gas O₂ was set to 50 sccm. For nanorod growth, the transducers were placed downstream of the Ar/O₂ mixing plasma without substrate heating. All deposition parameters are summarised in Table 4.4.

Table 4.4 PECVD parameters used for SnO₂ nanorod thin layers.
(Conductometric devices' sensitive layer)

PLASMA ENHANCED CHEMICAL VAPOUR DEPOSITION	
Deposition System	PECVD reactor with inductively coupled plasma (ICP) operated at 13.56 MHz
RF Power	1.2 kW
Deposition Temperature	90° C
Reactive Gas	Oxygen (O ₂)
Carrier Gas	Argon (Ar)
Gas Flow Rate	Ar / O ₂ = 50 / 50 sccm
Working Pressure	Atmospheric pressure

4.2.3 Electron Beam Evaporation

Electron Beam (E-beam) evaporation is an extensively used deposition method in research applications to obtain a wide range of thin film materials. In most common E-beam evaporators, an electron gun under the crucible (with charge for evaporation) ejects an electron beam. The beam is bent through 270° by a strong magnetic field causing it to be incident on the surface of the high purity solid charge (e.g. metal). This beam can be rastered across the surface of the charge, heating it and leading to evaporation.

4.2.3.1 Intermediate Layer Deposition

E-Beam Evaporation was used to deposit silicon nitride films on SAW transducers and their properties were investigated and compared with the PEVCD and r.f. magnetron sputtered SiN_x films. The samples' surfaces were cleaned before deposition by exposure to a low power Ar ion beam. Films of approximately 1 μm thickness were obtained using a 99.999 % compressed Si₃N₄ powder. The deposition process was conducted at the rate of 1 nm/s and the substrate temperature was kept constant at 130°C. Table 4.5 includes the deposition system characteristics and parameters.

Table 4.5 E-Beam evaporated deposition parameters used for the SiN_x layer

ELECTRON BEAM EVAPORATION	
Deposition system	E-beam evaporator equipped with a cryogenic pump
E-beam evaporative source	E-gun with tungsten filament and 270° electromagnetic beam folding
Base Pressure	5×10^{-6} Torr
Deposition Temperature	Room temperature
Working Pressure	1.2×10^{-4} Torr
Deposition rate	1 nm/s

4.2.4 Physical Vapour Deposition of 1-D InO_x Nanostructures

The author employed physical vapour deposition (*thermal evaporation*) for the synthesis of thin layers of 1-D nanostructures of InO_x on silicon. This method uses thermal evaporation of nanosized metal oxide powders placed on an alumina boat inside a quartz tube, in a furnace controlled environment under constant gas flow. The deposition parameters, e.g.

temperature and deposition time can be varied to obtain different layer thicknesses. Rapid heating of the source material results in the formation of vapours which are carried to the “cold regions” where they condense forming nanostructures such as nanowires, nanorods, nanobelts and etc. Indium oxide thin films of nanowires/nanobelts were deposited using 99.995% pure In_2O_3 powder as a source material (purchased from China Rare Metal Material Co. Ltd.). Approximately 5 g of powder was placed in the central part of a 60 cm quartz tube (Figure 4.5).

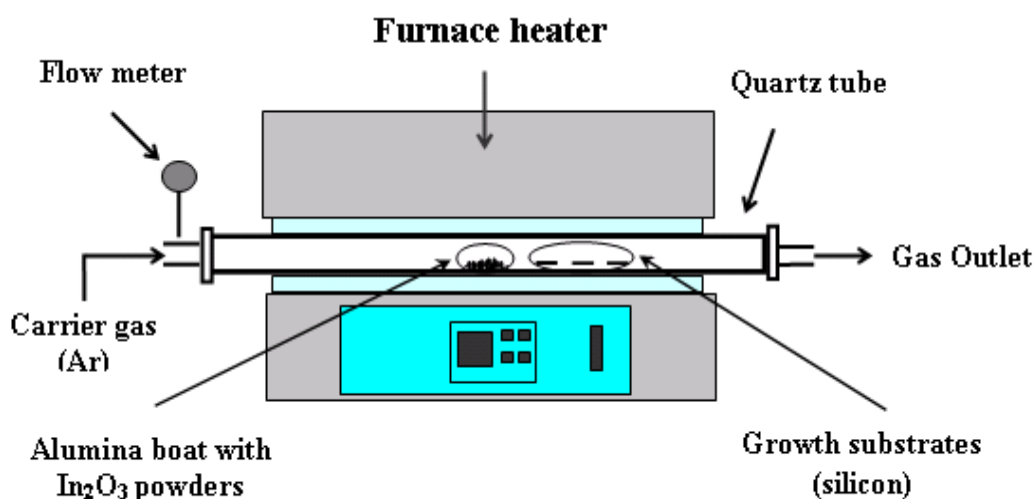


Figure 4.5 Schematic of the experimental apparatus used for the growth of InO_x nanostructures

Different substrate materials such as silicon, lithium tantalate with and without a thin layer of Au as a catalyst were placed at different distances from the source. A 5-40 nm thin catalyst layer of Au was deposited by a d.c. sputter coater. The furnace temperature was increased at a heating rate of $50^\circ \text{C}/\text{minute}$ and the Ar gas flow rate was kept constant at 500 sccm. The deposition temperature was varied between 600 and 1100°C and the deposition time between 30 and 180 minutes. The obtained nanostructures were mainly nanobelts and nanowires with different diameters and lengths.

4.3 Layered SAW Sensor Frequency Response

During the fabrication processes, before and after deposition of a layer, the device's frequency responses (S-parameters, S_{21} transmission parameter) were measured using a network analyser (Rhode & Schwarz ZVRE) using 50Ω calibrated leads.

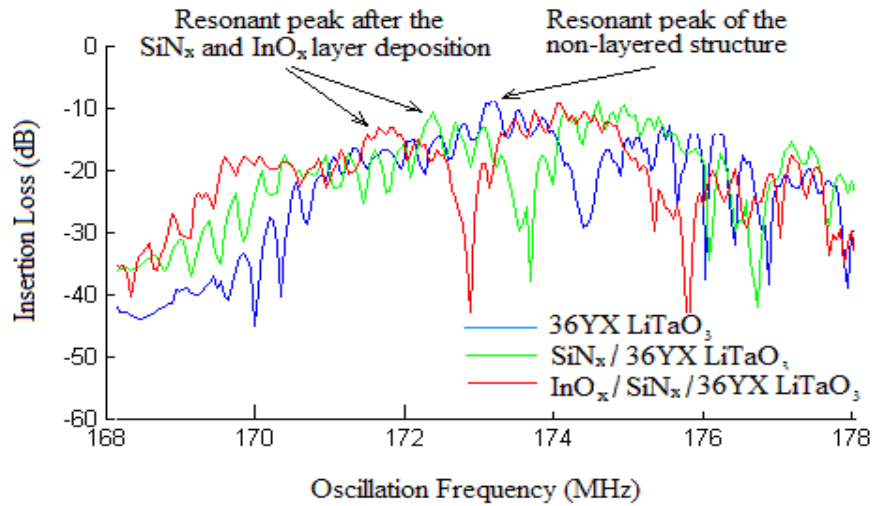


Figure 4.6 Frequency response of a $\text{InO}_x/\text{SiN}_x/36^\circ\text{YXLiTaO}_3$ SAW sensor at three stages of fabrication process

Figure 4.6 shows the measured S_{21} transmission parameters after each major step of the fabrication process of a $\text{InO}_x/\text{SiN}_x/36^\circ\text{YXLiTaO}_3$ layered SAW sensor. The sharp resonant peak in the non-layered structure (shown in blue) at 173.2 MHz changes significantly after the SiN_x intermediate and InO_x sensitive layers are deposited. The deposition of these layers resulted in a change in insertion loss from -8dB to -14dB.

4.4 Summary

In this chapter, the fabrication steps of the developed gas sensors have been presented. Firstly the patterning process of the IDTs was outlined. This was followed by a presentation of the deposition methods, including the deposition parameters used to obtain the intermediate and gas sensitive layers as well as the frequency response of the layered SAW device.

The SAW transducers were fabricated by the author using cleanroom and vacuum lab facilities provided by the Microelectronics and Materials Technology Centre (MMTC) at RMIT University. The metallisation of the substrate wafers was done by MMTC staff using E-beam evaporation.

Chapter 5

Gas Calibration System

This chapter describes the measurement set-up and testing procedures used for the fabricated layered SAW and conductometric sensors. To test the gas sensing performance of the sensors, a multi-channel gas calibration system was used with sequence control and data acquisition software. This includes a purpose built SAW sensor testing system, which was developed in the Sensor Technology Laboratory at RMIT University.

The chapter is divided in two sections. Section 5.1 describes the measurement techniques used in this research work to monitor the SAW devices' operational frequency and SMO films conductance changes during the gas sensing experiments. In section 5.2 the computer controlled gas calibration system is described. Section 5.3 provides a brief summary of this chapter.

5.1 Measurement Techniques

5.1.1 SAW Gas Sensor

The change in velocity of an acoustic wave due to the interaction of target gas molecules with sensitive layer in a SAW device can be measured by phase and frequency techniques. One of the phase measurement techniques involves measuring the transfer function of the SAW device with a two port network analyser. In this case a network analyser is used to measure phase and attenuation as a function of the input frequency. By measuring the scattering S – parameters (S_{11} , S_{22} , S_{12} , S_{21}) the SAW device phase and attenuation over a given frequency range can be determined. This method provides a stable platform for analyses; however it also requires a specialised and expensive network analyser setup. Further information on this technique can be found in [106]. The author has performed such measurements with a Rhode & Schwartz model ZVRE network analyser with 50 Ω calibrated leads, during SAW sensor fabrication steps and under test conditions.

Another widely used method, which requires less expensive laboratory equipment, is the frequency change measurement technique [107]. In this case the SAW device is used as the frequency control element in a closed loop oscillator circuit as shown in Figure 5.1.

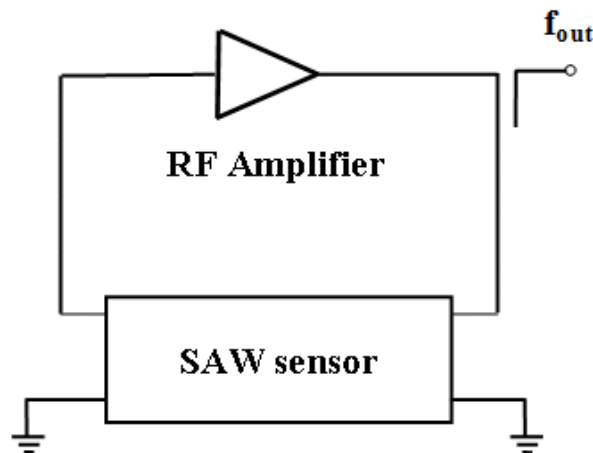


Figure 5.1 Basic schematic of an oscillator for measuring the SAW device oscillation frequency

In this set-up the SAW device functions as a positive feedback element in a circuit with an RF amplifier, where the voltage at the output of the RF amplifier is fed back through the SAW sensor. The signal is delayed by the SAW device before it is re-amplified again resulting in an alternating signal which will be self-sustained, hence forming an oscillator. In steady-state operation the circuit will oscillate if the total loop gain is unity (or larger) and the phase shift (equation 5.1) equals an integer (n) multiple of 2π [106]:

$$\Phi_{SAW} + \Phi_e = -2n\pi \quad (5.1)$$

where Φ_{SAW} and Φ_e are the phase shift of the SAW device and of the electrical circuit (amplifier and gas chamber electrical connections). The Φ_{SAW} of the SAW delay line can be related to the delay line length L (centre-to-centre spacing between the IDTs) by the following equation (5.2), where v is the acoustic wave velocity at the piezoelectric substrate surface [139].

$$\Phi_{SAW} = -\frac{2\pi fL}{v} \quad (5.2)$$

Using equation (5.1) and (5.2) the oscillator frequency f can be written as:

$$f = \frac{2\pi n - \Phi_e}{2\pi L} v \quad (5.3)$$

When the amplifier is working in a closed loop condition, Φ_e is constant and the following relationship exists:

$$\frac{\Delta f}{f_0} \cong \frac{\Delta v}{v_0} \quad (5.4)$$

where Δv is the change of SAW velocity, f_0 and v_0 are the unperturbed oscillation frequency and SAW velocity. From equation (5.3) it can be seen that the oscillation frequency depends on several system parameters. The performance of the system depends both on the sensor and electronic circuitry (e.g. a common problem can be the oscillator instability and random noise effects). A high gain RF amplifier was designed as well as a gas chamber for stable operation. Frequency measurements for each of the layered SAW structures were made by the author during the experimental gas testing sensing procedures, presented in Chapter 7. A high-resolution, 10 digit counter (Fluke PM6680B) was used to measure the oscillation frequency.

5.1.2 Conductometric Sensor

The conductometric sensors were tested using the same gas chamber and calibration system as used for the SAW gas sensors. The gas sensor's resistance change was recorded by a digital multimeter (Keithley 2001). Regulated DC voltage was supplied by a programmable power supply (Agilent E3649A) to the heater to operate the sensors at elevated temperatures. A Labview based program in the main computer controls all the calibration systems components via a GPIB interface. The measured data is recorded every 4 seconds and at the same time the sensor's response (resistance) is plotted.

5.2 Gas Sensor Measurement System

Gas Calibration System

A custom built SAW sensor testing system, consisting of an RF amplifier and a gas chamber, incorporated in a multi-channel gas calibration system was used to conduct the testing of the fabricated SAW sensors.

Figure 5.2 shows a diagram of the complete gas calibration system set-up used for testing. Four computers controlled mass flow controllers (MFC) were used to set a constant flow rate of 200 sccm to produce the required concentration of gas analytes (H_2 , NO_2 and CO) balanced in synthetic air (“zero-air”).

The gas calibration system setup includes the following instruments:

- MFC control processing unit (from MKS Inc. Instruments)
- sequence control computer, to automate the operational temperature and the sequence of gas concentrations
- data acquisition computer to monitor the oscillation frequency and resistance
- temperature logger to monitor the heater’s temperature
- Fluke (PM6680B) high-resolution frequency counter to measure the oscillation frequency
- Agilent (E3649A) 2-channel DC power supply to provide a 5V constant voltage for the RF amplifier as well as the power for the sensors’ heater
- custom built computer controlled ozone generator
- Keithley 2001 digital multimeter for conductometric sensor testing

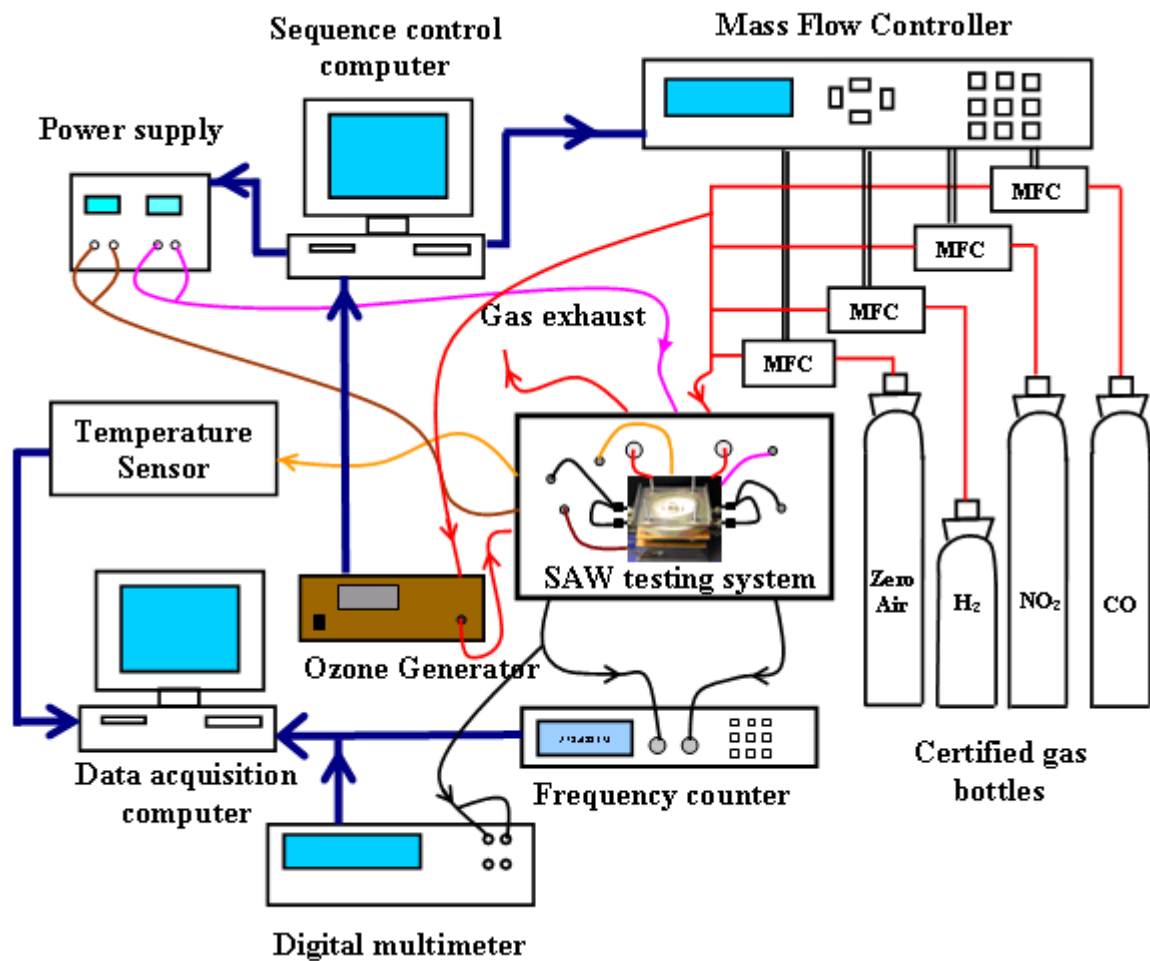


Figure 5.2 Diagram of the multi-channel gas calibration system setup

The SAW testing system (Figure 5.3) was incorporated in a steel box, for shielding against electromagnetic interference (EMI) and for thermal stability was placed in an environmental chamber with a constant ambient temperature of 22°C. An account of the RF amplifier design and characteristics and SAW testing system are described in Appendix C.

The amplifier PCB was mounted on an aluminium block to support the structure. The two PCBs (carrier and the amplifier) were connected by coaxial cables. The author measured the resonant (or oscillation frequency) of the SAW sensors' before and after they were placed in the SAW testing system. Different lengths of coaxial cables were used to vary the total loop

phase to satisfy the total loop-gain condition of unity (or higher) with a phase integer multiple of 2π (equation 5.1) and to reach the required oscillation frequency. This process was repeated until the correct length of coaxial cable was found and the sensors were locked on the proper resonance mode (or oscillation frequency).

Gas Chamber

The chamber (Figure 5.3) has a volume of 30 mm^3 with a Teflon block and a fused quartz lid.

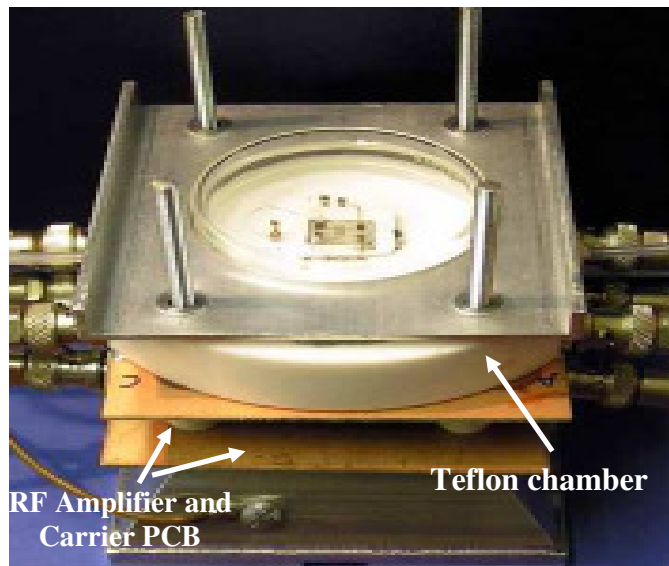


Figure 5. 3 Custom built teflon chamber and RF amplifier assembly from [29]

The sensors were mounted on micro-heaters inside the chamber. Two types of micro-heaters were employed in this research work and both are shown in Figure 5.4. One has a platinum serpentine resistive element on sapphire substrate ($10 \times 12 \text{ mm}$) and the larger one ($25 \times 25 \text{ mm}$) has an evaporated Ni/Cr layer serpentine resistive element on an alumina substrate heater. The larger heater had a better temperature distribution and a maximum temperature of 330°C compared to the other heater with platinum serpentine resistive element on sapphire substrate

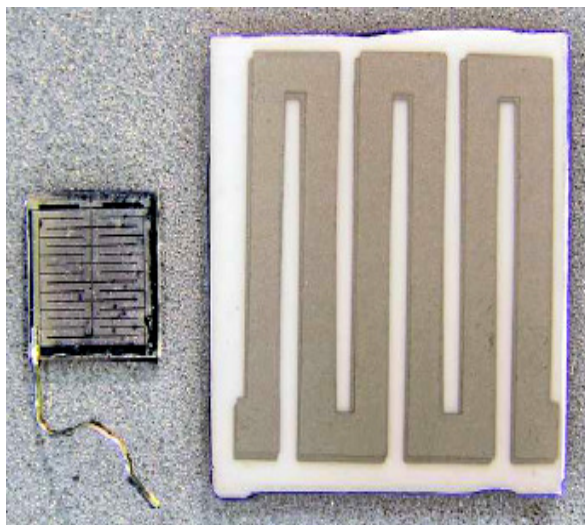


Figure 5.4 Heaters used for testing with : (a) sapphire and (b) alumina substrate

LabView software programs were used to record data from the Fluke (PM6680B) frequency counter as well as the Keithley digital multimeter. Data was collected using a computer with a GPIB IEEE-488 bus connection. The programs recorded the oscillation frequency (Fluke meter) and the resistance values (Keithley multimeter) every 4 seconds. The acquired data was displayed in real time via a graphical user interface. Certified gas bottles balanced in synthetic air (“zero-air”) were used with the following gas concentrations: 10,000 ppm H_2 , 8.4 ppm NO_2 and 1005 ppm CO.

An in-house designed and purpose built computer controlled ozone generator was used to generate ozone to test the SAW sensors. Ionised synthetic air flowing through a quartz tube under a UV light source (pen-ray type UV lamp) generated ozone. The intensity of the UV light source was determined by a microprocessor controlled metallic shutter: no exposure to ozone was generated when the metallic shutter was fully closed and 50 ppb when it was fully opened. A software program enabled the author to control the ozone concentrations, exposure time and the power supply voltages for the heater used in the test systems.

Table 5.1 lists the analyte gas concentrations and the pulse sequences used for testing throughout this research work.

Table 5 1 Gas pulses and their concentrations used for testing the sensors

Analyte Gas	Gas pulse sequence					
	<i>First</i>	<i>Second</i>	<i>Third</i>	<i>Fourth</i>	<i>Fifth</i>	<i>Sixth</i>
H₂* (%)	0.06	0.12	0.25	0.50	1.00	0.12
NO₂ (ppm.)	0.51	1.06	2.12	4.25	8.50	1.06
CO (ppm.)	125	250	500	125	-	-
O₃ (ppb.)	20	40	20	40	-	-

*1.00% H₂ in air = 10,000 ppm

5.3 Summary

This chapter described the testing procedure, testing system and setup used by the author to calibrate and test the sensors performance. Results will be presented in Chapter 7.

Chapter 6

Microstructural Characterisation of Sensors' Layers

The importance of the surface morphology and chemical composition of a SMO sensitive layer with regard to the sensitivity of a gas sensor was presented in Chapter 3. There is a strong connection between a gas sensor's performance and its sensitive layer's microstructure and chemical composition. By improving these characteristics, the film's gas sensing properties can be enhanced. For a layered SAW gas sensor it is also essential to investigate the intermediate layer's chemical composition. It is necessary to understand not only the deposited layers' characteristics but also the interface between them, since this influence the performance of the sensor. To make this possible the sensitive and intermediate layers were investigated by X-ray Photoelectron Spectroscopy (XPS), Scanning Electron Microscopy (SEM) and X-ray Diffraction (XRD). The surface morphology of the synthesized one-dimensional (1-D) thin films of InO_x nanobelts and SnO_2 nanorods were examined and

characterised by Scanning and Transmission Electron Microscopy (SEM, TEM) to determine their suitability for gas sensing applications.

The author has performed chemical and microstructural characterisation to answer the following research questions:

- What is the chemical composition (stoichiometry) of the deposited indium oxide sensitive and silicon nitride intermediate layers?
- How do the indium oxide film properties change for films deposited on different substrates (e.g. what is the crystalline orientation of such films on different substrates)?
- What is the structure of the deposited indium oxide layer (e.g. is it amorphous or polycrystalline)?
- Are the deposited one dimensional (1-D) indium oxide and SnO_2 nanorod layers suitable for gas sensing applications (e.g. have they suitable dimensions, density and orientations)?

To determine the elemental composition of the deposited films for the layered SAW sensor, X-Ray Photoelectron Spectroscopy (XPS) was used. The obtained results were compared to the stable stoichiometric forms of In_2O_3 and Si_3N_4 . Scanning Electron Microscopy (SEM), Field Emission Scanning Electron Microscopy (FE-SEM), X-Ray Diffraction (XRD), and

Transmission Electron Microscopy (TEM) were used to investigate the surface morphology (e.g. grain size, nanorods dimensions) and orientation of the deposited sensitive layers.

This chapter is organized into two main parts: one is dedicated for the chemical characterization and the other focuses on the surface morphology and structural characterisation of the deposited films. Each part includes a description of the analytical technique employed for characterisation, explaining its role in the overall characterisation process. This is followed by presentation of the results for each of the investigated layers and concludes with a discussion of the obtained results. Additionally, one section describes the method used for estimating the electron concentrations of the indium oxide thin layers.

6.1 Chemical Characterisation

By performing chemical characterisation, the type and density of different elements and compounds at the surface and in the bulk of the films can be determined as well as their spatial depth distribution. To determine the quantitative elemental composition and stoichiometry of the deposited indium oxide and silicon nitride layers the author has utilized XPS. Depth profiling was carried out on the indium oxide layers deposited on the intermediate layers and on the indium oxide layers deposited on the LiTaO₃ substrates.

6.1.1 X-Ray Photoelectron Spectroscopy (XPS)

This technique known also as Electron Spectroscopy for Chemical Analysis (ESCA) is a surface sensitive technique (1-10 nm deep), showing which chemical elements are present at the surface. XPS analyses can give information about the nature of chemical bonds and valence states which exists between these elements. Despite being a technique which analyses only the surface, by combining it with sputter etching of the film, XPS can also be used for

depth composition investigation by analysing the newly exposed surfaces during etching at close intervals of depth.

In XPS, the in-coming X-rays excite photoelectrons in a film and the emitted electron signal is plotted as a spectrum of binding energies. By exposure to these X-rays, electrons in an atomic orbital are freed from the attractive force of the nucleus of the atom and travel through the matter and into the vacuum around the sample in the XPS chamber. The kinetic energy associated with the emitted electrons is given by [5]:

$$E_{kinetic} = h\nu - E_{binding} - \Phi_m \quad (6.1)$$

where, $h\nu$ is the X - ray beam incident energy, h is Plank's constant, ν is the frequency of the incident radiation, $E_{binding}$ is the electron binding energy inside the atom and Φ_m is the work function of the material i.e. , the minimum energy required for an electron to be removed from the solid surface and go into vacuum. Electrons emitted from the films are detected and the collected information can be interpreted as several discrete binding energies, associated with different electron levels in different atoms and a spectrum of binding energies can be produced. For every element, there will be a characteristic binding energy associated with each core atomic orbital, i.e. each element will give rise to a characteristic set of peaks in the photoelectron spectrum at energy levels determined by the binding energies of electrons in different orbitals in different atoms. The relative intensity of the peaks is related to the concentration of the element within the sampled region. The presence of peaks at particular energies therefore indicates the presence of a specific element in a specific binding state in the sample under study. Quantitative data is obtained from the elemental distributed peak areas and the chemical state identification is obtained by curve fitting software simulations of

different compositions and accurate measurement of the various peak positions and their separation from other peaks.

XPS was performed on an Escalab MkII (VG Scientific) with a dual Al/Mg anode unmonochromated X-ray source operated at 300 W and 15 kV excitation voltages. During the measurements the samples were mounted on a standard VG Escalab stub by using an Au foil mask with a window of 3 mm in diameter. The XPS apparatus is equipped with a 5 channeltron detection system and a standard Al K_{α} excitation source ($K_{\alpha} = 1486.6$ eV) and an Ar^{+} ion gun used for cyclic sample sputtering between the selected-area measurements. The electrostatic lenses of the spectrometer were operated in selected-area mode that provided photoelectron collection from a sample area of about 1 mm^2 . The XPS depth profiles were acquired by using a 2.0 keV energy Ar^{+} beam, rastered over an area defined by the window in the Au mask.

In order to investigate the chemical composition of the films as well as the interface between the indium oxide and silicon nitride films and the interface between indium oxide and the 36° YXLiTaO₃ substrate, several samples were produced as follows:

- (i) indium oxide films, approximately 100 nm thick, were deposited by r.f. magnetron sputtering onto bare 36° YXLiTaO₃ substrates and on silicon nitride/ 36° YX LiTaO₃ substrates.
- (ii) silicon nitride films, approximately 1 μm thick, were deposited onto bare 36° YX LiTaO₃ substrates by r.f. magnetron sputtering, PECVD, and E-beam evaporation.

Prior to analyses the indium oxide thin films were annealed at 300°C for 3 hours in synthetic air in a similar manner as for the films deposited for the fabricated SAW devices. The thicknesses of the as-deposited films were measured by an XBIOS stylus profilometer. The

films thicknesses are determined by profiling the height of a substrate-to-film step in a profilometer trace.

6.1.1.1 Indium Oxide Sensitive Layer

Table 6.1 shows the typical elemental composition of the r.f. magnetron sputtered indium oxide (InO_x notation used for non-stoichiometric In_2O_3) thin layers, before XPS depth profiling, deposited on the surfaces of : (i) three different SiN_x (non-stoichiometric Si_3N_4) intermediate layers deposited by three different methods ($\text{SiN}_x/36^\circ\text{YXLiTaO}$) and (ii) bare 36°YXLiTaO_3 substrate.

Table 6.1 Comparison of the r.f. sputtered InO_x thin layers before depth profiling showing the atomic percentage of elements with their corresponding binding energies in eV and the atomic ratio of O/In

$\text{InO}_x/\text{PECVD SiN}_x/$ $/36^\circ\text{YX LiTaO}_3$ Atomic ratio O/In = 0.95	Atomic concentration (%)	In 44.1	O 42.1	C 10.6
	Binding Energy (eV)	444.6 ($\text{In}_{3d5/2}$)	530.4 (O_{1s})	285.0 (C_{1s})
$\text{InO}_x/\text{r.f. sputtered SiN}_x/$ $/36^\circ\text{YX LiTaO}_3$ Atomic ratio O/In = 1.00	Atomic concentration (%)	In 44.2	O 44.5	C 11.3
	Binding Energy (eV)	444.8 ($\text{In}_{3d5/2}$)	530.5 (O_{1s})	285.0 (C_{1s})
$\text{InO}_x/\text{E-beam SiN}_x/$ $/36^\circ\text{YX LiTaO}_3$ Atomic ratio O/In = 1.12	Atomic concentration (%)	In 46.5	O 52.1	C 1.4
	Binding Energy (eV))	444.7 ($\text{In}_{3d5/2}$)	529.5 (O_{1s})	285.0 (C_{1s})
$\text{InO}_x/36^\circ\text{YX LiTaO}_3$ Atomic ratio O/In = 1.12	Atomic concentration (%)	In 41.2	O 46.1	C 12.7
	Binding Energy (eV)	444.8 ($\text{In}_{3d5/2}$)	530.5 (O_{1s})	284.9 (C_{1s})

From this table it can be seen that the metal oxide is not stoichiometric In_2O_3 as the atomic ratio of O/In is approximately 1.0 for all layers. The XPS spectra peaks for $\text{In}_{3d5/2}$ and O_{1s} occurring at the binding energies (BE) listed in the table for the indium and for the oxygen peak corresponds to indium bonded to oxygen in the form of In_2O_3 (XPS handbook [140]). The presence of carbon contamination (peak C_{1s}) at the surface was also observed in all of these layers. This occurs during or after deposition due to handling the samples in air. Subsequent to sputter etching, the amount of carbon reduced significantly; as shown in Table 6.2 and 6.3.

Table 6.2 XPS – Elemental composition of an InO_x layer deposited on r.f. magnetron sputtered SiN_x on a $36^\circ\text{YX LiTaO}_3$ substrate showing the atomic percentage of the main elements before and after 60 minutes of etching

Ion Sputtering time	C_{1s}	$\text{In}_{3d5/2}$	O_{1s}
t = 0	11.3%	44.5%	44.2%
t = 60 min	5.5%	51.9%	42.6%

Table 6.3 XPS - Elemental composition of an r.f. magnetron sputtered InO_x film on a $36^\circ\text{YX LiTaO}_3$ substrate showing the atomic percentage of the main elements before and after 60 minutes of etching.

Ion Sputtering time	C_{1s}	$\text{In}_{3d5/2}$	O_{1s}
t = 0	12.7%	40.9%	46.2%
t = 60 min	1.15%	50.5%	48.3%

For the investigation of the interfaces between the deposited InO_x and SiN_x layers and between the SiN_x and the 36°YXLiTaO_3 substrate, depth profiling was carried out. From the depth profile shown in Figure 6.1 it can be seen that the interface between the r.f. magnetron sputtered InO_x film on SiN_x is neat and well defined. This means that the InO_x film was homogeneously deposited on the SiN_x and the interface was not affected by any thermal diffusion or any chemical reaction during the deposition process. It can be seen that there is the presence of a significant amount of oxygen within the SiN_x layer. It can be stated that this sample consists of two layers: InO_x and silicon oxynitride (SiO_xN_y).

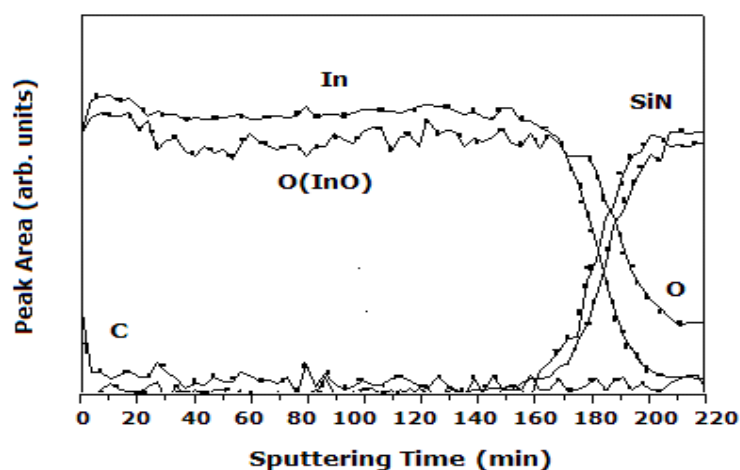


Figure 6.1 XPS depth profile of $\text{InO}_x/\text{SiN}_x$ layers deposited by r.f. magnetron sputtering on a $36^\circ\text{YX LiTaO}_3$ substrate

Figure 6.2 illustrates the depth profile for an InO_x layer on a 36°YXLiTaO_3 substrate showing that the interface is neat and well defined, meaning that the film is uniform through the whole thickness.

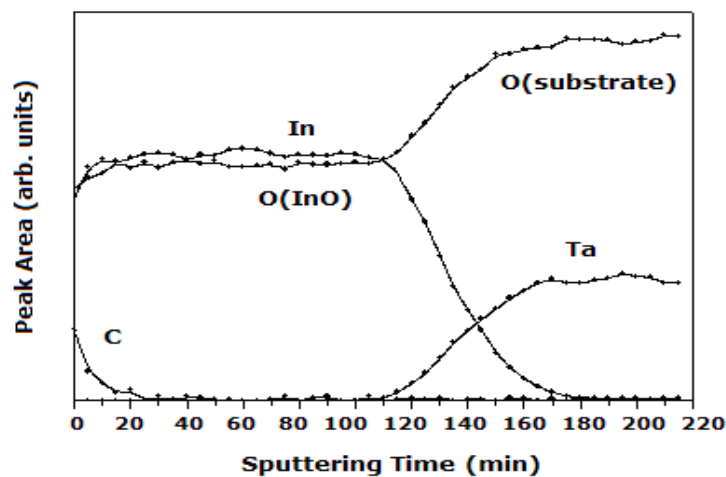


Figure 6.2 XPS depth profile of an r.f. magnetron sputtered InO_x layer on a 36°YXLiTaO_3 substrate

Figure 6.3 shows the $\text{In}3d_{5/2}$ and $\text{In}3d_{3/2}$ XPS spectra, for different sputter etching time intervals ($t_s = 0, 30, 60$ and 90 min), of a sample with an InO_x thin layer deposited onto PECVD SiN_x . The XPS spectra peaks for $\text{In}3d_{5/2}$ and $\text{O}1s$ before and after sputter etching are occurring at the BE of 444.6 eV for the indium and 530.5 eV for the oxygen peak which corresponds to indium bonded to oxygen in the form of In_2O_3 (as listed in the XPS handbook [140]).

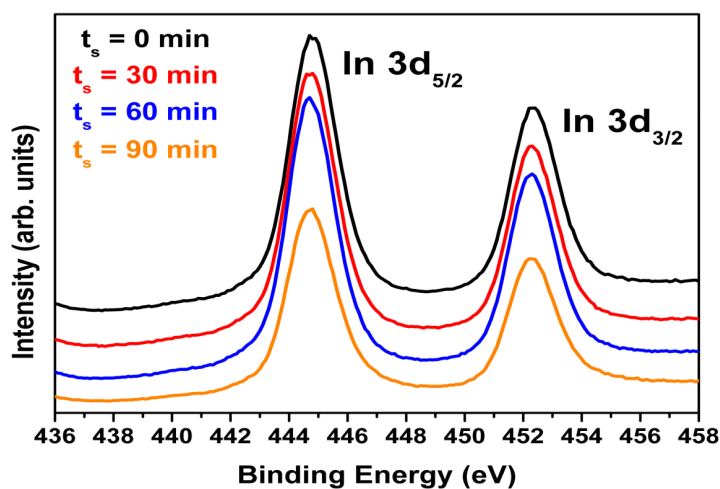


Figure 6.3 XPS spectra of the $\text{In}3d_{5/2}$ and $\text{In}3d_{3/2}$ peaks registered after different sputtering time intervals (t_s)

To further investigate the stoichiometry of the indium oxide layer the author has determined the modified Auger parameters of the deposited films which were then compared with the data reported in the literature from the National Institute of Standard and Technology (NIST) database [141].

The modified Auger parameter α' can be calculated as:

$$\alpha' = \text{BE} (\text{In}_{3d5/2}) + \text{KE} (\text{In}_{\text{MNN}}) \quad (6.2)$$

where $\text{BE}(\text{In}_{3d5/2})$ is the binding energy measured for the XPS signal for $\text{In}_{3d5/2}$ and $\text{KE} (\text{In}_{\text{MNN}})$ is the kinetic energy measured for the Auger signal In_{MNN} . Table 6.4 lists the values of this parameter before and after 5 minutes of ion sputter etching. The modified Auger parameter values given in Table 6.4 are in agreement with the standard value for non-stoichiometric indium oxide InO_x , $\alpha' = 851.4$ eV, where $x = 1$ [142].

Table 6.4 Modified Auger parameters in (eV) for the indium oxide layers before and after 5 minutes of ion sputter etching

Sample #	Before ion sputtering	After 5 minutes ion sputtering
$\text{InO}_x/\text{PECVD SiN}_x$	850.4	851.4
$\text{InO}_x/\text{r.f. sputtered SiN}_x$	850.4	851.5
$\text{InO}_x/36^\circ \text{ YX LiTaO}_3$	850.6	851.5

6.1.1.2 Silicon Nitride Intermediate Layers

Figure 6.4 show the depth profile of a sample with r.f magnetron sputtered InO_x on a PECVD SiN_x layer on a 36°YX LiTaO_3 substrate. Three layers are distinctly visible in Figure 6.4. There is the top layer of InO_x which is uniform in composition through the whole thickness of this layer. The second layer is composed of SiO_2 , which occurs between the InO_x and the SiN_x layers and has an estimated thickness of 20-30 nm. A SiN_x layer was observed after 230 minutes of ion sputtering, which is also listed in Table 6.5, where the atomic percentages of the main elements with their corresponding BE's in eV obtained during depth profiling are given. The possible reasons for the formation of the thin SiO_2 intermediate layer between the InO_x and SiN_x will be discussed in the next section.

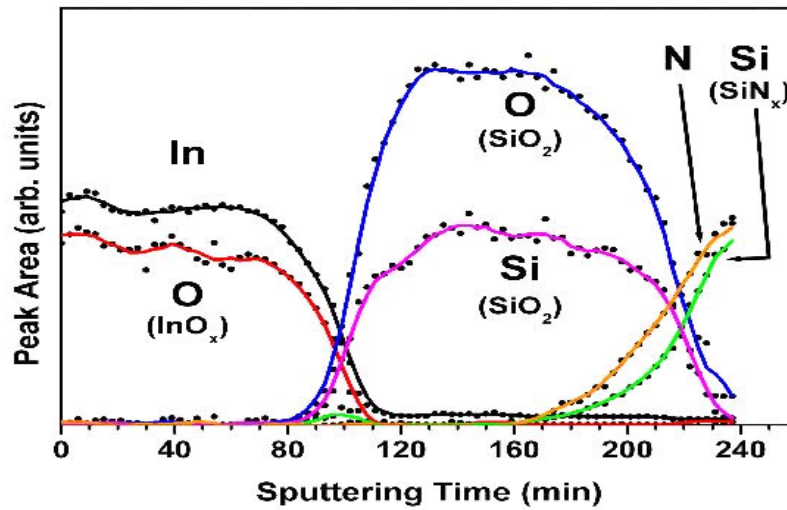


Figure 6.4 XPS depth profile of an r.f. magnetron sputtered InO_x layer on PECVD SiN_x layer on a 36°YX LiTaO_3 substrate

As seen in Figure 6.4 the interfaces between the InO_x and SiO_2 films as well as that between the SiO_2 and SiN_x layers is well defined. The binding energy values measured for the Si_{2p} and O_{1s} peaks is equal to 103.6 and 533.0 eV respectively, which are typical values of the SiO_2 compound [140]. The SiN_x layer, after the sputter etching time of 230 minutes, is

characterized by the complete absence of oxygen. The atomic ratio of this film is Si/N = 1.15 which is different from the atomic ratio of Si/N = 1.33 of stoichiometric silicon nitride (Si_3N_4), and thus it can be concluded that the deposited silicon nitride is non-stoichiometric.

Table 6.5 Atomic percentage of the main elements with their corresponding binding energies in eV at different sputter etching time intervals for a sample with $\text{InO}_x/\text{PECVD SiN}_x$ layers deposited on a 36°YX LiTaO_3 substrate.

Sputtering Time (min.)		C	In	O (InO_x)	O ($\text{H}_2\text{O}_{\text{ads.}}$)	O (SiO_2)	Si (SiO_2)	Si (SiN)	N
0	At. %	10.6	44.1	42.1	3.2				
	B.E. (eV)	285.0	444.8	530.4	532.5				
40	At. %		54.4	45.6					
	B.E. (eV)		444.8	530.3					
160	At. %					57.8	42.2		
	B.E. (eV)					532.8	103.4		
230	At. %							53.5	46.5
	B.E. (eV)							102.0	398.0

Figure 6.5 presents the depth profile of a sample consisting of a r.f. magnetron sputtered SiN_x film on 36°YX LiTaO_3 substrate and a summary of the XPS elemental compositions can be seen in Table 6.6.

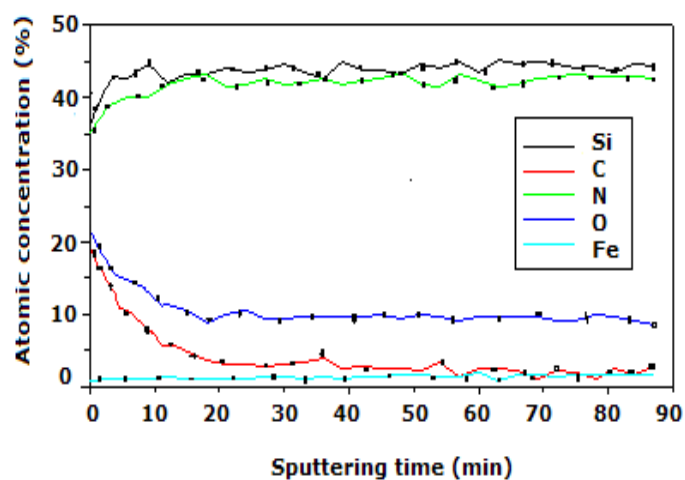


Figure 6.5 XPS depth profile of an r.f. magnetron sputtered SiN_x layer on 36°YX LiTaO_3 substrate

Table 6.6 XPS - Elemental composition of an r.f. magnetron sputtered SiN_x layer deposited on a 36°YX LiTaO_3 substrate showing the atomic percentage of the main elements.

(A) Before depth profiling (no etching)

Auger Peak	$\text{Si}_{2p3/2}$	C_{1s}	$\text{N}_{1s}(\%)$	$\text{O}_{1s}(\%)$
Atomic Concentration (%)	29.6	19.8	29.5	20.8
Binding Energy (eV)	101.9	285.0	397.8	532.5

(B) After etching for 78 minutes

Auger Peak	$\text{Si}_{2p3/2}$	C_{1s}	N_{1s}	O_{1s}
Atomic Concentration (%)	44.8	2.8	43.7	8.7
Binding Energy (eV)	102.0	285.0	397.9	532.4

The $\text{Si}_{2p_{3/2}}$ peak with BE of 102 eV and N_{1s} peak with BE of 397.8 eV correspond to the BE values for Si_3N_4 in the XPS Handbook [140]. The atomic ratio of Si/N is a 1.0 but the film has an atomic percentage of 21% oxygen (peak O_{1s}) as well as a contamination in form of carbon (C_{1s}). Therefore it can be stated that the film at the surface is silicon oxynitride (SiO_xN_y). Also from the XPS elemental composition data table (Table 6.6 B) it can be seen that after 78 minutes of ion sputtering the oxygen (O_{1s} peak) content has been reduced to 8.7% atomic percentage and the carbon (C_{1s}) has also been reduced significantly to less than 3%. Regarding the presence of carbon this was formed after the deposition when the samples were exposed to the atmosphere.

The XPS analysis (Table 6.7) indicates that the E-beam evaporated SiN_x layer has an atomic percentage of 94.7% silicon and only 5.1% of nitrogen. The dominant peak of for Si_{2p} occurs at the BE of 101.9 eV and for N_{1s} is at 398.9 eV. The surface contamination of carbon in this case is less than 2%.

Table 6.7 XPS – Elemental composition before depth profiling of an E-Beam evaporated SiN_x film deposited on a 36°YX LiTaO_3 substrate showing the atomic percentage of the main elements

Auger Peak	$\text{Si}_{2p_{3/2}}$	N_{1s}	C_{1s}
Atomic Concentration (%)	94.7	5.2	1.1
Binding Energy (eV)	101.9	398.9	294.0

6.1.2 Discussion

The chemical characterisation revealed that the 100 nm thick r.f. magnetron sputtered sensitive layers of indium oxide were non-stoichiometric. Indium oxide in non-stoichiometric form is a highly conductive n-type semiconductor and an excellent gas sensing material [89]. Chemical characterisation revealed that all r.f. magnetron sputtered InO_x films presented an atomic ratio of O/In between 0.95 and 1.12 (Table 6.1) at the surface, and between 0.84 and 1.04 in the bulk of the films (Table 6.2 and 6.3). Comparing these values to the atomic ratio of $\text{O/In} = 1.5$ for stoichiometric In_2O_3 , which has a 60% atomic concentration of oxygen and a 40% atomic concentration of indium, it appears that there is a 8-17% oxygen deficiency in the InO_x films formed. Also it was observed that the films presented some carbon contamination on the surface, formed after deposition due to handling the samples in air, but the carbon signal was much reduced in the bulk of the film.

Table 6.8 shows a summary of the XPS results for the films deposited as intermediate layers for SAW sensors using the three different deposition techniques (sputter coating, PECVD and E-beam evaporation). In a similar way as for the indium oxide sensitive layer (InO_x), for the non-stoichiometric silicon nitride, the notation SiN_x was used.

From this table it can be seen that the surfaces of the films deposited by the three different methods are non-stoichiometric silicon nitride (SiN_x). XPS depth profiling revealed the bulk was also non-stoichiometric. There are significant differences in the elemental composition of these layers formed by the three different techniques.

Table 6.8 XPS results of the SiN_x layers before depth profiling. The layers were deposited on 36° YX LiTaO_3 substrates and were utilised as intermediate layers for SAW based sensors.

PECVD method $\text{SiO}_2/\text{SiN}_x$ layers Atomic ratio $\text{Si/N} = 1.15$	Atomic concentration (%)	Si 43.2 (SiO_2) Si 53.5 (SiN_x)	N 46.5	C 11.3	O 57.8 (SiO_2)
	Binding Energy (eV)	103.4 ($\text{Si}_{2p\ 3/2}$) 102.0 ($\text{Si}_{2p\ 3/2}$)	398.0 (N_{1s})	285.0 (C_{1s})	532.8 (O_{1s})
R.f. magnetron sputtering method SiO_xN_y layer Atomic ratio $\text{Si/N} = 1.00$	Atomic concentration (%)	Si 29.3	N 29.4	C 19.6	O 20.8
	Binding Energy (eV)	102.0 ($\text{Si}_{2p\ 3/2}$)	397.9 (N_{1s})	285.0 (C_{1s})	532.5 (O_{1s})
E-beam evaporation method Si-rich layer $\text{Si/N} = 18.1$	Atomic concentration (%)	Si 94.1	N 5.2	C 1.5	
	Binding Energy (eV)	101.9 ($\text{Si}_{2p\ 3/2}$)	398.9 (N_{1s})	287.0 (C_{1s})	

The E-beam evaporated film was Si-rich, the r.f. magnetron sputtered films at the surface (~30-40 nm) were SiO_xN_y , and in the case of low temperature PECVD deposition, a thin (~20-30 nm) SiO_2 layer was formed between the InO_x and SiN_x layers. Underneath these layers the Si/N ratio was 1.0 for the r. f. magnetron sputtered films and for the PECVD film it was 1.15. These ratios are different to the value of 1.33 for stoichiometric Si_3N_4 . As was reported recently, the formation of a SiO_2 layer when the low temperature PECVD technique is employed is due to the exposure of the samples to environmental conditions when they are taken out of the PECVD chamber after deposition [137,143]. According to Jehanathan et al. [143] the structure and the properties of PECVD SiN_x thin films are sensitive to

environmental conditions such as humidity, atmospheric oxygen and temperature. When the samples are exposed to air, the oxygen in the atmosphere decomposes on the surface of the SiN_x forming SiO_2 , since the silicon-oxygen bond is more stable than the silicon-hydrogen bond. Furthermore Liu et al. in 2006 [137] reported the formation of a random mixed structure of SiO_2 in a matrix of non-stoichiometric SiN_x after low temperature PEVCD due to various environmental conditions such as atmospheric oxygen, elevated temperature and humidity in an oxidizing media.

6.2 Electron Concentration of the Indium Oxide Layers

To estimate the electron concentration, the first step was to determine the sheet resistance (R_{SH}) in Ω/\square of the non-stoichiometric indium oxide thin layer deposited on the SAW devices. The sheet resistance and hence resistivity (ρ) in $\Omega\cdot\text{cm}$ were calculated using equation 6.3 for the standard semiconductor “4-point probe” configuration [144] and equation (6. 4) for uniformly doped thin films:

$$R_{SH} = 4.532 \frac{V}{I} \quad (6.3)$$

$$\rho = R_{SH} t \quad (6.4)$$

where V is the voltage difference (drop) resulting from an input current I and thickness $t = 100 \text{ nm}$ was used. Results are shown in Table 6.9.

Table 6.9 Calculated sheet resistance, resistivity and conductivity values of the deposited 100 nm thin InO_x layers

Sample #	Intermediate layer	Sheet resistance $R_{SH} (\Omega/\square)$	Resistivity $\rho (\Omega.cm)$	Electrical conductivity $\sigma(\Omega^{-1}cm^{-1})$
(SAW) EF01	1 μ m PECVD SiO ₂ /SiN _x	1.20×10^5	0.12×10^1	5.00×10^{-1}
(SAW) EF05	2 μ m PECVD SiO ₂ /SiN _x	3.50×10^5	0.34×10^1	1.20×10^{-1}
(SAW) EF12	1 μ m Evaporated SiN _x	1.00×10^6	0.10×10^2	5.00×10^{-2}
(SAW) EF08	1 μ m r.f sputtered SiO _x N _y	1.70×10^6	0.17×10^2	2.90×10^{-2}

Table 6.10 Resistivity (ρ), conductivity (σ) and carrier concentrations of the doped and non-doped indium oxide films from the published literature [145-148]

Doped and non-doped indium oxide from the published literature [137-139]	Conductivity $\sigma (\Omega^{-1}cm^{-1})$	Carrier concentrations $n (cm^{-3})$	Resistivity ρ (Ωcm)
Non-doped indium oxide and annealed in air (InO1) [146]	0.11×10^1	1.00×10^{17}	9.09×10^{-1}
Non-doped indium oxide and annealed in N ₂ (InO2) [146]	0.65×10^1	3.40×10^{17}	1.54×10^{-1}
Tin doped (0.01 %) indium oxide and annealed in air (ITO1) [149]	0.75×10^1	3.10×10^{18}	1.33×10^{-2}
Non-doped indium oxide and annealed in CO-CO ₂ (InO3) [146]	5.88×10^2	4.20×10^{19}	1.70×10^{-3}
Tin doped (0.05 %) indium oxide and annealed in air (ITO2) [146]	3.33×10^2	1.55×10^{19}	3.00×10^{-3}
Tin doped (0.1 %) indium oxide and annealed in air (ITO3) [146]	1.38×10^2	3.10×10^{19}	1.82×10^{-3}
Tin doped indium oxide and annealed in air (ITO4) [149]	1.45×10^2	2.60×10^{20}	6.90×10^{-3}
Tin doped (5.5%) indium oxide and annealed in air (ITO5) [148]	5.00×10^3	9.50×10^{20}	2.00×10^{-4}
Tin doped (7.0%) indium oxide and annealed in air (ITO6) [148]	5.60×10^3	1.20×10^{21}	1.80×10^{-4}

In Table 6.10 the sheet resistance R_{SH} (Ω/\square), conductivity $\sigma = 1/\rho$ ($\Omega^{-1}\text{cm}^{-1}$) and carrier concentrations n (cm^{-3}) values are shown for the non-doped and the doped indium oxide (indium tin oxide - ITO) films reported in the published literature [145-148].

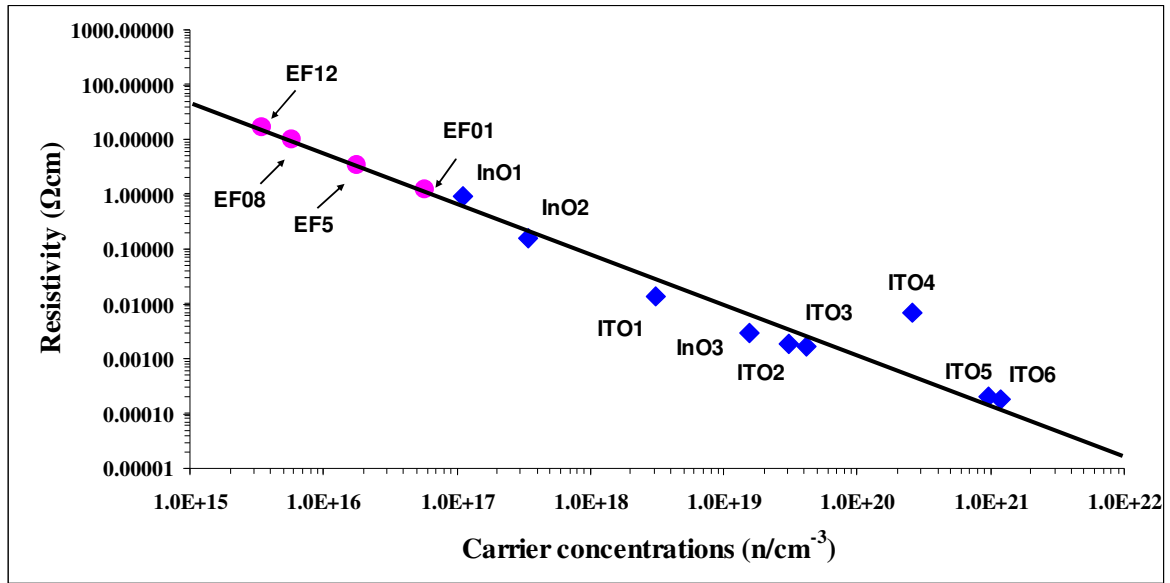


Figure 6.6 Extrapolation methods used to determine the carrier concentration of the non-doped indium oxide films deposited on the layered SAW devices

Figure 6.6 above demonstrates the approach for estimating the electron (charge carrier) concentrations of the non-doped indium oxide layers deposited on the layered SAW devices. First of all the carrier concentrations and resistivity of some of the doped and non-doped indium oxide films reported in the published literature (listed in Table 6.10) were plotted. This was followed using Microsoft Excel 2003 for the addition to the graph of the “Trendline”, which is based on the method of *least squares*, to determine by extrapolation the carrier concentrations using the calculated resistivity values.

Note:

- this extrapolation assumes a near-linear log-log relationship which is correct for semiconductors and can be assumed to be correct for InO_x
- the mobility of the carriers varies by only a factor of 2 or 3 as reported in published literature.

The trendline, shown in Fig 6.6, gives the approximate order of magnitude of the carrier concentrations for each of the four samples which are listed in table 6.9. The author used this method as a Hall Effect semiconductor measurement system was not available at RMIT University or any other accessible institution.

Table 6.11 Resistivity (ρ), conductivity (σ) and extrapolated carrier concentrations of the non-doped indium oxide films deposited on layered SAW devices

Non-doped indium oxide on Layered SAW devices	Conductivity σ ($\Omega^{-1}\text{cm}^{-1}$)	Extrapolated Carrier concentrations n (cm^{-3})	Resistivity ρ (Ωcm)
EF01	8.33×10^{-1}	5.80×10^{16}	0.12×10^1
EF05	2.90×10^{-1}	1.80×10^{16}	0.34×10^1
EF12	1.00×10^{-1}	5.80×10^{15}	0.10×10^2
EF08	5.85×10^{-2}	3.50×10^{15}	0.17×10^2

As it can be seen in Table 6.11, the carrier concentrations of the indium oxide films deposited on the SAW devices with PECVD intermediate layer (EF01 and EF05) have values in the order of 10^{16} cm^{-3} , compared to the other SAW devices' (EF12 and EF08) films which have values in the order of 10^{15} cm^{-3} . The devices with films having the higher carrier concentrations (hence higher conductivity) provided superior gas sensing performance in terms of response magnitude and response time (test results for O_3 and H_2 gases are shown in Chapter 7) compared with devices lower carrier concentrations.

6.3 Surface Morphology and Structural Characterisation

The author utilised SEM and FE-SEM to examine the surface morphology of the InO_x layers. XRD analyses were performed on the InO_x layers to identify the crystalline phases, the crystallographic structure and preferential orientation. TEM was used to investigate the SnO₂ nanorods dimensions and their orientation.

6.3.1 Scanning Electron Microscopy (SEM)

SEM is one of the most versatile instruments used for the examination of surface topography and the microstructure of materials. It provides a highly magnified image of the surface of the material with a typical lateral resolution of 1-50 nm. With an Energy Dispersive X-ray (EDX) Spectroscopy system, attached to a high resolution SEM, by monitoring the secondary X-rays produced by the electron-specimen interaction, a compositional analyses of the material may also be obtained. In the SEM, an electron beam is focused in vacuum into a probe and subsequently rastered over the surface of a specimen resulting in the emission of electrons and photons. A fraction of these emitted electrons can be collected by appropriate detectors and an image is formed on a monitor.

There are two classes of emission sources used to produce an electron beam: *thermionic emitter* and *field emitter*. The emitter type is the main difference between the SEM and the FE-SEM. The *thermionic emitters* in an SEM use electrical current to heat up a filament (which functions as a cathode). It is made of different materials, the most common one being Tungsten (W). In the case of a *field emitter* the emission is reached by placing a tungsten filament (field emission tip) in a large electrical potential gradient, obtaining a cleaner image with less electrostatic distortions and spatial resolution less than 2 nm, which results in it being 3 or 6 times better than an SEM. Throughout this research, three SEM instruments were

used. The first one was a high resolution Philips XL-30 SEM manufactured by Oxford Instruments. The second system was a LEO1530 FE-SEM, which can provide higher spatial resolution (1.5 nm at 15 kV) and can operate at low accelerating voltages (5 nm at 1 kV). Finally the SnO_2 nanostructures were investigated by a LEO1550 FE-SEM.

6.3.1.1 Planar Two-Dimensional (2-D) Nanostructures

The r.f. magnetron sputtered InO_x thin layers were found to be polycrystalline as indicated by the SEM and FE-SEM (Figure 6.7 and 6.8) micrographs and by the X-ray diffractograms obtained. The SEM micrographs of the r.f. magnetron sputtered InO_x thin films deposited on $\text{SiN}_x/36^\circ \text{ YX LiTaO}_3$ are shown in (Figure 6.7 a, b). It can be seen that the film has a columnar compact structure with uniformly distributed grains across the entire surface with a well defined orientation. The orientation obtained by XRD will be discussed in section 6.3.3.

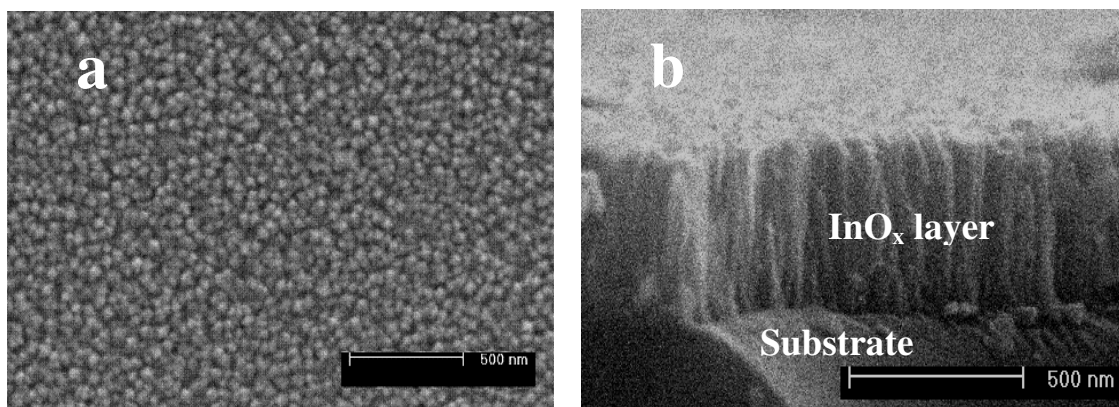


Figure 6.7 SEM micrographs of an r.f. magnetron sputtered InO_x layer on LiTaO_3 substrate: (a) top view and (b) cross-sectional view of this layer

To further examine the surface of the InO_x layer and to gather more information regarding the grain sizes, FE-SEM analyses was employed. The results are shown in Figure 6.8 (a) and 6.8 (b). It can be seen from these micrographs that the film has a polycrystalline structure and

is composed of nanosized crystallites with estimated grain sizes between 20 and 40 nm in diameter. From figure 6.8 (b) it can be seen in some parts, agglomerates of crystallites were also observed, which are typical occurrences when r.f. sputter deposition is employed for thin films.

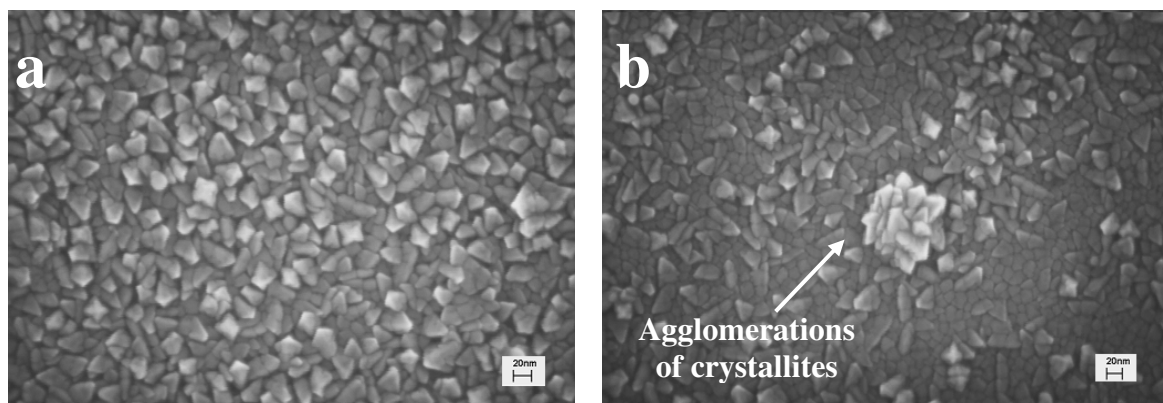


Figure 6.8 FE-SEM micrographs of a polycrystalline InO_x thin film with (a) uniform distribution of the nanosized crystallites and (b) in some parts agglomerations of crystallites occurred

6.3.1.2 One-Dimensional (1-D) Nanostructures

Quasi 1-D nanostructures of indium oxide nanobelts and nanowires were synthesized on silicon substrates by physical vapour deposition and tin oxide (SnO_2) nanorods were deposited by PECVD on 36° YX LiTaO_3 transducers..

Synthesis of Indium Oxide Nanobelts on Silicon Substrates

The author undertook an investigation into synthesising 1-D indium oxide nanostructures on blank silicon substrates. The elevated temperature required for the growth of these nanostructures [93,150] is a major obstacle as the high temperature obliterates the piezoelectric properties of the LiTaO_3 substrate, and hence it could not be used after

deposition. Therefore the author undertook the deposition of nanobelts and nanowires on silicon substrates with the objective to transfer these structures onto LiTaO_3 substrates for fabrication of SAW devices for gas sensing applications. The deposition method employed, described in Chapter 4, was the thermal evaporation of nanosized In_2O_3 powders through vapour–solid (VS) and vapour-liquid-solid (VLS) growth processes. Syntheses were conducted with and without the presence of a gold catalyst and nanostructures were obtained in the form of nanobelts and nanowires. The SEM examination revealed a sparse, random distribution of these nanostructures.

In order to transfer these structures onto LiTaO_3 substrates the samples were sonicated in ethanol for 20 to 60 minutes and drop-cast onto SAW transducers. Unfortunately due to the limited resources available these transfer approaches were not able to be successfully realised. In order to carry on with the investigation of 1-D nanostructures for gas sensing application the author has turned his attention towards the application of tin oxide (SnO_2) nanostructures. This material is also an excellent gas sensing material and it is possible to synthesize it at a lower temperature by employing a novel deposition method [138]. As a result the author has obtained thin layers of SnO_2 nanorods deposited at the low temperature of 90°C on 36° YX LiTaO_3 substrates at the Nanyang Technological University in Singapore. A LEO 1550 FE-SEM were used to obtain secondary electron images of the SnO_2 nanorods films and their dimensions was studied using a JEOL JEM-2100F TEM. A description of these nanostructures is presented in the next section and their application for gas sensing is outlined in Chapter 7.

SnO₂ Nanorods Deposited on 36°YXLiTaO₃ substrates

As described in Chapter 4, the deposition system was a custom designed PECVD reactor where an inductively coupled plasma (ICP) source was generated at the standard frequency of 13.56 MHz and with a power of 1.2 kW. The RF source was coupled via a copper tape circling the quartz deposition chamber. The growth of SnO₂ nanorods was accomplished by a “*sputtering redeposition*” growth process developed by H. Hui et al. [138,150] from Nanyang Technological University of Singapore. Using this novel method the SnO₂ nanorods were directly formed at the low temperature of 90°C from the as-deposited SnO₂ thin film during treatment by a plasma source without the assistance of a metal catalyst. Moreover no additional substrate heating was required. The SnO₂ nanorods grown on SAW transducers by this method resulted in the formation of nanorods wherein the bombardment of heavy ions such as Ar⁺ in the plasma releases film species which redeposit and grow preferentially to form nanorods. The continuous sputtering with the plasma will begin to separate the compact columnar grains of the as-deposited layer from each other after plasma treatment and as a result some are transported and redeposited to form nanorods with needle-like shapes. The described growth processes are controlled by parameters such as plasma power, duration of plasma treatment and by the gas composition. Huang et al. [138,150] have grown SnO₂ nanorods on a silicon substrate using the method described and obtained nanorods with similar needle-like shapes but with random orientations. On the 36° YX LiTaO₃ SAW transducers the nanorods grew uniformly presenting a preferential orientation, illustrated in the FEG-SEM micrographs of Figure 6.9. (a) and (b).

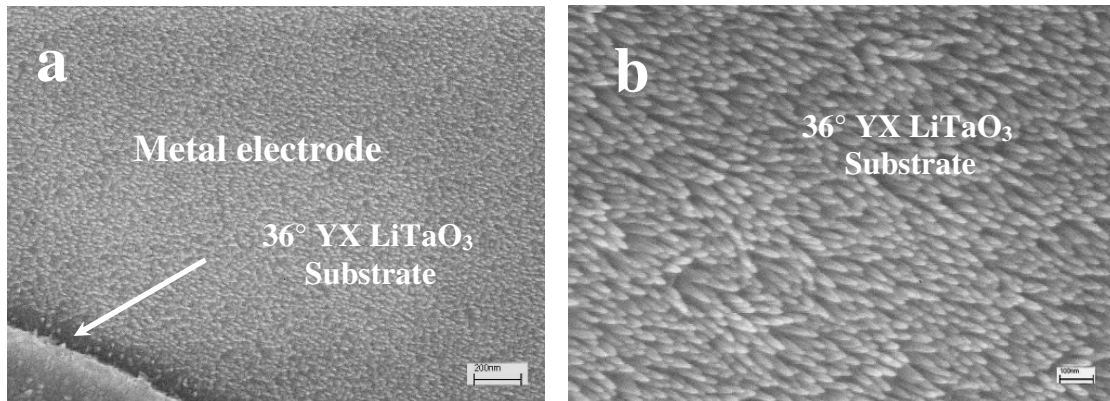


Figure 6.9 FEG-SEM micrographs of SnO_2 nanorods deposited on: (a) SAW transducer IDT and (b) a 36° YX LiTaO_3 substrate

A High Resolution TEM (HRTEM) determined the diameters of the nanorods to be 10-20 nm near the tip and 20-40 nm at the base, where the typical length of one nanorod was approximately 200 nm (Figure 6.10). The SnO_2 XTEM lattice image shown in Figure 6.11 confirms that the nanorods are single crystals. The Fourier reconstructed diffraction pattern corresponds to the tetragonal rutile crystal structure. The growth direction is determined to be $[10\bar{1}]$, which is different from the growth direction of $[110]$ reported previously for nanorods deposited on a silicon substrate [138,151].

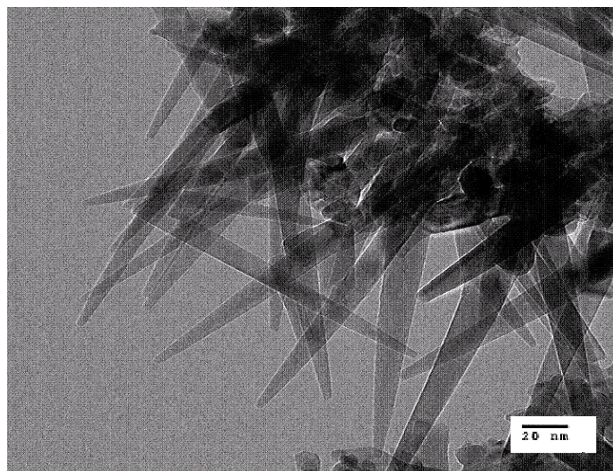


Figure 6.10 Bright field HRTEM image of a cluster of SnO_2 nanorods

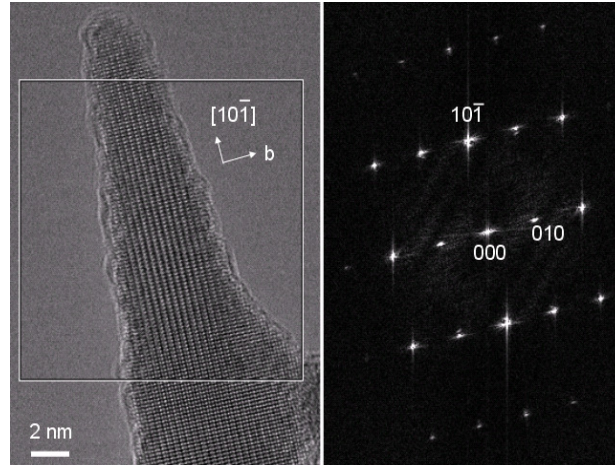


Figure 6.11 TEM lattice image and Fourier reconstructed diffraction pattern of the SnO₂ nanorods on a LiTaO₃ substrate

6.3.2 X-Ray Diffraction (XRD)

X-ray diffraction is a non-destructive efficient analytical technique for directly identifying the crystallographic structure and indirectly identifying chemical composition, and physical properties of materials and thin films. Monochromatic X-rays are directed at a crystalline material at varying angles to determine the interplanar spacings of the unknown material. The X-rays are diffracted by atomic planes. At a particular angle where there is constructive interference from X-rays diffracted from the atomic planes of the crystal, a X-ray diffraction peak is observed.

The condition for constructive interference from planes with spacing d_{hkl} is given by Bragg's law:

$$\lambda = 2d_{hkl} \sin \theta_{hkl} \quad (6.5)$$

where θ_{hkl} is the angle between the normal to the atomic planes and the incident and diffracted X-ray beams. By varying this angle, Bragg's Law conditions are satisfied for

different d_{hkl} spacings in crystalline and polycrystalline materials. By plotting the angular positions and intensities of the resultant diffracted peaks a diffraction pattern is produced, which is characteristic of the crystal sample. When a mixture of different phases is present, the resultant diffractogram is formed by the individual peak pattern. The diffractogram is compared with the powder diffraction pattern card of the particular material from the International Centre for Diffraction Data (ICDD) database. This includes the d_{hkl} spacings related to the angle of diffraction θ_{hkl} and relative intensities of observable diffraction peaks.

The structure of the InOx thin films was investigated using a Bruker-AXS D8 Discover with a General Area Detector Diffraction System (GADDS). The D8 Discover with GADDS illuminates samples with a tuned monochromatic and parallel X-ray beam. The spatially diffracted X-rays are then detected and counted using software from Bruker's GADDSPLUS suite. The operating conditions of the GADDS are given in Table 6.12. The peak positions were compared with the ICCD 6-416 card's X-ray diffraction peaks for standard In₂O₃ powder.

Table 6.12 Operating conditions of the GADDS

X-rays	Cu Kα
Voltage and Current	40 KV and 40 mA
Detector	2D area detector

6.3.2.1 Planar 2-D InO_x layer

The XRD diffractograms of as-deposited and annealed r.f. magnetron sputtered InOx thin films on a 36°YXLiTaO₃ substrate are shown in Figure 6.12. The as-deposited InO_x layer has

the highest intensity peak for the (521) plane in comparison with the annealed InO_x layer where the highest intensity peak is for the (400) plane. On silicon substrates the r.f. magnetron sputtered InO_x film presented the highest intensity peak along the (400) plane, shown in Figure 6.12. All diffraction peaks (shown in figure 6.12 and 6.13) are corresponding to the cubic structure of In₂O₃.

The lattice constant of InO_x was calculated from the highest intensity peak for the (521) plane for the as-deposited r.f. sputtered film. Using the X-ray wavelength of $\lambda = 0.154$ nm (Cu K_α) and the angle $2\theta = 49.25^\circ$ of the (521) plane, the distance between the adjacent planes can be calculated using equation 6.1. The calculated distance (d_{521}) was 1.848 Å which is in good agreement with the value of 1.85 Å given in the ICDD 6-416 card of standard In₂O₃ powder [152].

The lattice constant of α_0 for the cubic structure of In₂O₃ can be calculated by the equation [126]:

$$\frac{1}{d_{hkl}^2} = \frac{h^2 + k^2 + l^2}{\alpha_0^2} \quad (6.6)$$

Applying this equation for the (521) plane, the calculated lattice constant is $\alpha_0 = 1.0121$ nm which is very close to the of ICDD 6-416 value of $\alpha_0 = 1.012$ nm for the cubic structure of In₂O₃ [152].

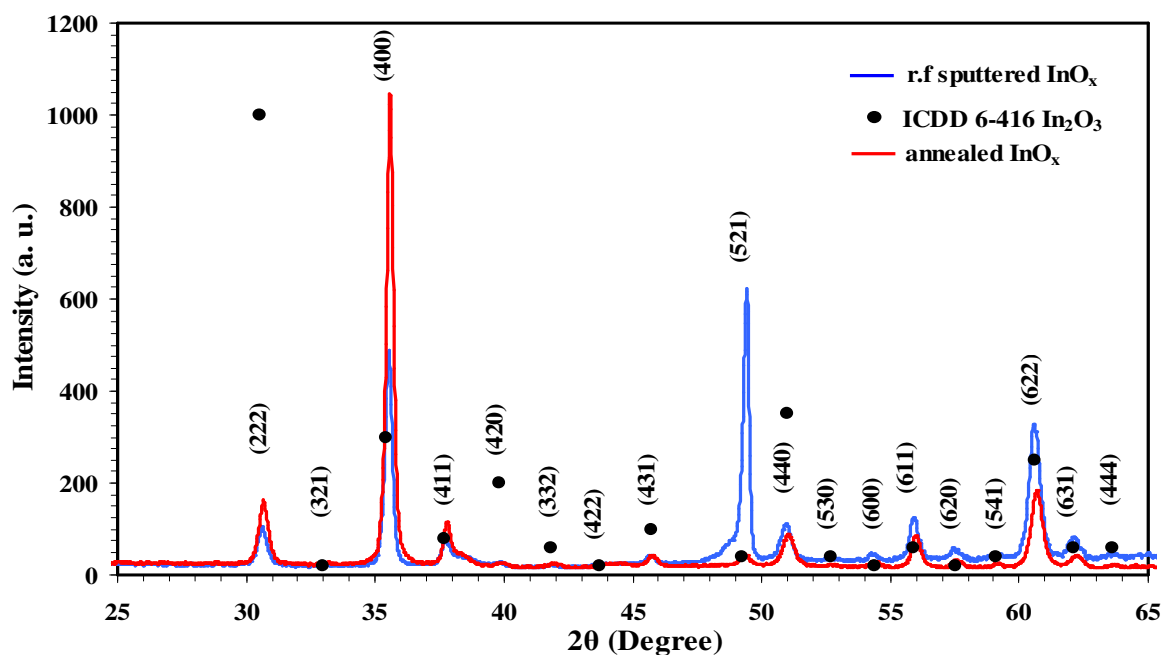


Figure 6.12 XRD diffractograms of as-deposited r.f. magnetron sputtered and annealed InO_x layers 36° YX LiTaO₃ substrate.

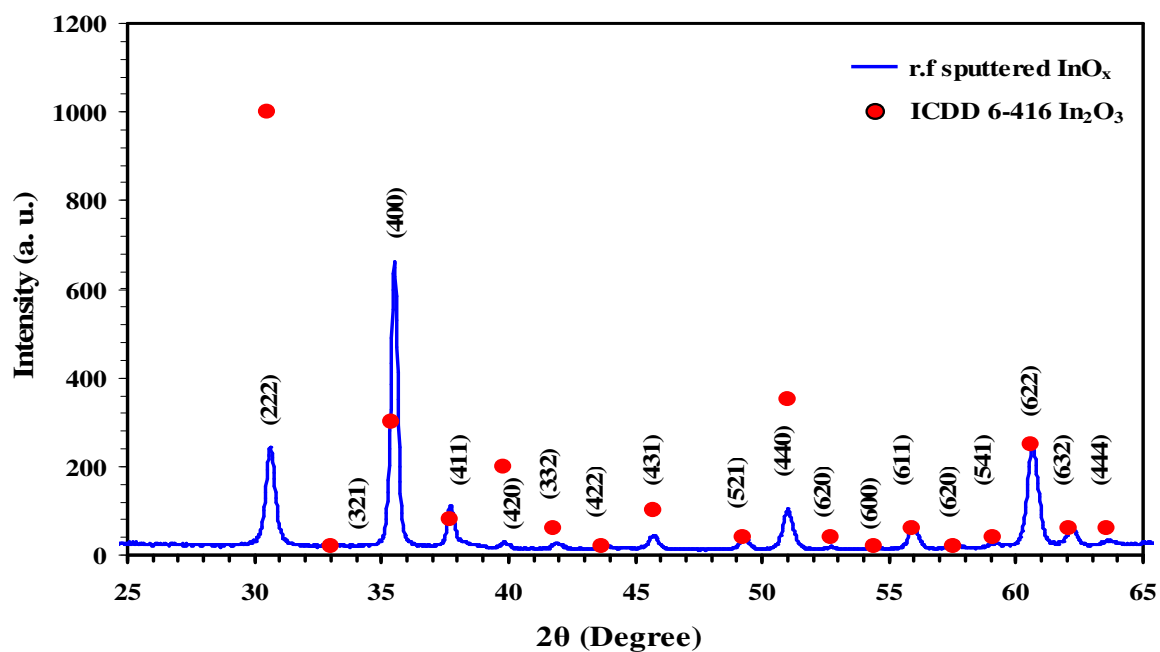


Figure 6.13 XRD diffractogram of the r.f. magnetron sputtered InO_x thin film on a silicon substrate

6.3.3 Discussion

In Chapter 3 the influence of grain sizes on gas sensing performance was presented. The morphology and grain (crystallite) sizes of the InO_x thin films are strongly dependent on the fabrication method and deposition conditions [89,126].

The SEM and FE-SEM analyses revealed a polycrystalline structure with nanosized grains for the InO_x thin films employed as sensitive layers in this research work. The estimated grain sizes from the FEG-SEM analyses of the polycrystalline InO_x films were around 20-40 nm.

The XRD diffraction patterns (diffractograms) (Fig. 6.11) showed that for the as-deposited InO_x films on LiTaO_3 substrates, the highest peak intensity occurs for the (521) planes with the (400) planes having the next highest intensity. For the annealed films the intensity of the (521) planes is relatively insignificant. For the annealed films the highest peak intensity occurs for (400) planes. Other peaks also occur in the XRD diffractogram of the annealed films; these are for (222) which had the second highest intensity, (440) and (621) planes. Meng and Santos [149] reported that their deposited ITO films had the highest peak intensities for (400) planes before and after annealing of their r.f. magnetron sputtered films. Their diffractograms show lower intensities for the (222), (440) and (621) planes in similar ratios to that of the annealed films investigated in this thesis. Meng and Santos did not record any peak for the (521) plane. On the films in this thesis the (521) plane practically disappears after annealing. Note, that no responses were recorded for the SAW sensors before annealing indicating that an indium oxide films with a (521) orientation are not suitable for gas sensing. 1-D nanostructures due to their high volume-surface-to ratio they have excellent potential for gas sensing applications. The XTEM confirmed that the SnO_2 nanorods deposited on LiTaO_3 transducers are single crystals with nanosized dimensions and needle-like shape.

The diffraction pattern revealed a tetragonal rutile crystal structure of the SnO_2 with the preferential growth direction along $[10\bar{1}]$, which is different from the growth direction of $[110]$ previously reported for the nanorods deposited on a silicon substrate [138,151].

6.3 Summary

The planar 2-D InO_x and the 1-D SnO_2 nanorod sensitive layers exhibited very promising microstructural characteristics for gas sensing. The intermediate layer deposited by the three different methods revealed a non-stoichiometric silicon nitride.

A summary of the microcharacterisation results are given below, their application for gas sensing is presented in the next chapter.

1. InO_x sensitive layer

- Polycrystalline compact structure with nanosized grains with diameters 20-40 nm
- Non-stoichiometric (oxygen deficient stoichiometry) films with an atomic ratio of $\text{In} / \text{O} \sim 1.0$
- Homogeneous and uniform interface between the InO_x and intermediate layers
- Thicknesses of approximately 100 nm
- A metal oxide with a low content of impurities (i.e. carbon impurities)
- A cubic structure of with the highest intensity peak for (521) plane for the as-deposited r.f. magnetron sputtered InO_x layer and (400) plane for the annealed layer
-

2. SnO_2 nanorod sensitive layer

- Nanorods grew uniformly on the LiTaO_3 substrate

- Composed of single crystals with diameters of 10-20 nm at the tip and 20-40 nm at the base, where the typical length of one nanorod was approximately 200 nm
- Single crystal orientation of $[10\bar{1}]$ on the LiTaO_3 substrate obtained from the Fourier reconstructed diffraction pattern of the SnO_2 nanorods

3. SiN_x intermediate layer

- Non-stoichiometric and amorphous layer deposited by r.f. magnetron sputtering, PECVD and E-beam evaporation deposition techniques
- Chemical composition of the layers was SiO_xN_y when r.f. magnetron sputtering was used, the PECVD method formed a $\text{SiO}_2/\text{SiN}_x$ matrix and the E-beam evaporated layer was very rich in Si
- Thicknesses of approximately 1 μm

Chapter 7

Results – Gas Sensing Performance

The micro-characterisation results, presented in Chapter 6 revealed that the deposited InO_x and Sn_2O nanorod layers are suitable to be used as gas sensitive layers. The InO_x layers were non-stoichiometric and have a polycrystalline structure with grain sizes less than 50 nm. The SnO_2 nanorod layers have dimensions of 10-20 nm in diameters at the top and 30-40 nm at the base.

In this chapter the gas sensing performance of the developed gas sensors will be presented. They were exposed to a pulse sequence of H_2 , O_3 , NO_2 and CO and important sensor parameters such as, response and recovery time, operational temperature range, repeatability (reproducibility) and response magnitude were obtained and analysed. The chapter presents the test results in two sections.

In section 7.1 the gas sensing performance of the layered SAW sensors tested against H_2 and O_3 gases are presented and in section 7.2 the SnO_2 nanorod conductometric sensor's test results for CO and NO_2 is presented.

7.1 Layered SAW Sensors

The advantages of using an intermediate layer in a SAW based gas sensor structure was outlined in Chapter 1 and 2 and the method used by the author to select the thickness of this layer was presented in Chapter 3. Therefore using the three previously mentioned deposition techniques a 1 μm thick intermediate layer was deposited and as sensing layer a 100 nm thin film of InO_x was used for all devices. To compare the gas sensing performance of the layered SAW structures with their non-layered counterparts another SAW device without an intermediate layer were also fabricated.

In this section the gas sensing performance of the following layered SAW structures are presented:

- **$InO_x/SiO_xN_y/36^\circ YXLiTaO_3$**
(with 100 nm InO_x and 1 μm r.f. magnetron sputtered intermediate layer)
- **$InO_x/SiO_2/SiN_x/36^\circ YXLiTaO_3$**
(two devices with 100 nm InO_x and 1 and 2 μm PECVD deposited intermediate layer)
- **$InO_x/SiN_x/36^\circ YXLiTaO_3$**
(with 100 nm InO_x and 1 μm E-Beam evaporated intermediate layer)

The sensors were placed in the measurement set-up described in detail in Chapter 5. Before exposure to the testing gases the operational temperature was increased gradually to 310°C. For a “break-in” the sensors were held at this temperature for at least 3 hours, prior to testing. Next they were exposed to the H₂ pulse sequence between 0.06% (600 ppm) and 1.0% H₂ (10000 ppm) in synthetic air and towards O₃ concentrations between 20 and 150 ppb. The testing sequence was repeated a few times at 310°C. This was followed by the decrease of the temperature in steps of 20-25°C until room temperature was reached, carrying out by repeating a few times the same testing cycle at each temperature. Synthetic air was used before the exposure towards different gases at each temperature, to allow the sensors to reach thermal equilibrium, as well as after each gas exposure to allow the sensors to recover.

The gas sensing performance of the developed sensors were investigated by examining their response magnitude (frequency shift $-\Delta f$) for SAW sensors and resistance in air for the conductometric sensor, response and recovery time as well as their static performance characteristics such as reversibility, repeatability and the baseline frequency stability of SAW sensors (definition of these parameters can be found in Appendix E).

7.1.1 Hydrogen Sensing Results

The layered SAW sensors were exposed repeatedly to sequential pulses of 0.06%, 0.12%, 0.25%, 0.50%, 1.00% H₂ concentrations in air. To investigate the repeatability of the sensor at the end of the above sequence, the 0.12% H₂ concentration was applied again. The gas exposure time was 240 seconds followed by 480 seconds of synthetic air for recovery (or purge time) was used. As was previously described in Chapter 5 the frequency measurement technique was employed, recording the frequency shifts induced by the exposure to different gas concentrations.

Indium oxide in non-stoichiometric (InO_x) form is an n-type semiconductor and can be employed as a gas sensing material for both oxidizing and reducing gases [81]. As outlined in Chapter 3 for a reducing gas such as H_2 a reverse chemisorption will take place on the surface of the device and electrons are injected into the InO_x thin film increasing the conductivity of this layer. Hence the acoustic wave velocity will decrease resulting in a decrease in the operational frequency.

7.1.1.1 Sensor with PECVD Intermediate Layer ($\text{InO}_x/\text{SiO}_2/\text{SiN}_x/36^\circ\text{YXLiTaO}_3$)

The sensors with the 1 and 2 μm thick PECVD SiN_x intermediate layers exhibited repeatable and reversible large magnitude responses, shown in Figure 7.1. Both sensors presented very stable (baseline frequency stability of approximative 790Hz/1hr.) responses in the operational temperature range of 165°C to 310°C .

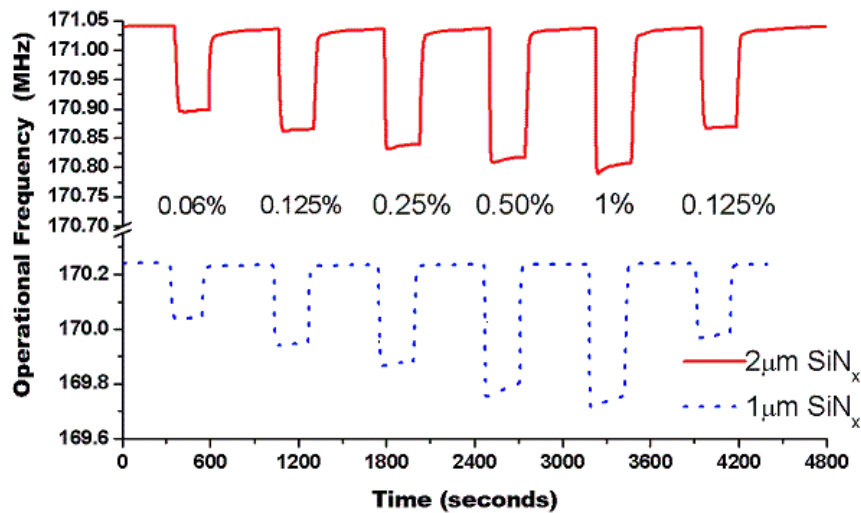
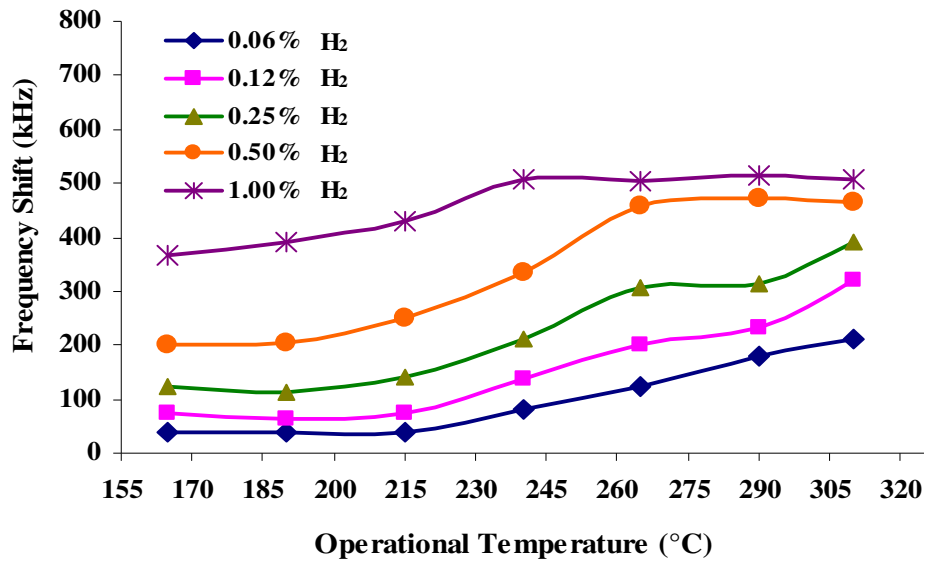
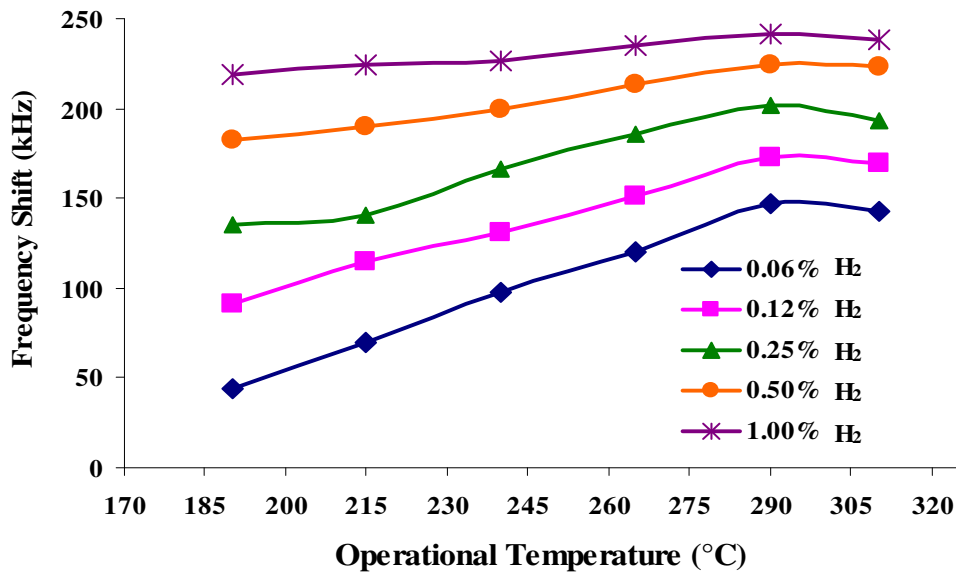


Figure 7.1 Dynamic responses of layered SAW sensors with 1 μm and 2 μm intermediate layers towards a sequence of pulses between 0.06% and 1.0% H_2 in synthetic air at 290°C

As can be seen in Figure 7.2 (a) and (b) the response magnitude increases with the temperature. The two sensors have different operational temperature ranges and present significant difference in their response magnitudes.



(a)



(b)

Figure 7.2 Frequency shift versus operational temperature for a layered SAW sensor with: (a) 1 μm and (b) 2 μm thick PECVD SiN_x intermediate layer

The operational temperature range of the SAW sensor with the 1 μm thick PECVD SiN_x is between 90°C to 310°C, and for the other sensor, is between 125°C and 310°C. However it was only between 165°C and 310°C that the sensors' responses returned back to the baseline well within the 480 seconds recovery time.

From Table 7.1 as it can be seen that the sensor with 1 μm SiN_x presents a higher response magnitude at 310°C than at 290°C for H_2 concentration less than 0.5 %. However the sensor suffers form poorer performance characteristics, such as stability and reversibility at this temperature.

Table 7.1 Frequency shifts at three consecutive operational temperatures for the SAW sensors with the 1 μm and 2 μm PECVD SiN_x intermediate layer at different H_2 concentrations

SAW Sensor with 1 μm PECVD SiN_x

Operational Temperature (°C)	Frequency Shift (kHz)				
265	122.9	201.9	307.6	457.5	503.3
290	179.6	232.7	315.1	471.2	516.0
310	212.5	319.9	391.5	466.2	506.8
Hydrogen Concentration (%)	0.06	0.12	0.25	0.50	1.00

SAW Sensor with 2 μm PECVD SiN_x

Operational Temperature (°C)	Frequency Shift (kHz)				
265	120.4	151.8	185.4	213.0	235.1
290	146.8	172.8	201.7	224.4	241.8
310	142.2	169.6	192.8	223.1	238.6
Hydrogen Concentration (%)	0.06	0.12	0.25	0.50	1.00

The response time was measured to be approximately 35 - 40 seconds for both sensors at 290°C. The sensor with the 1 μm SiN_x layer had a recovery time of 90 seconds in comparison with the other sensor, which has a longer recovery time of 115 seconds.

The sensor with 1 μm intermediate layer exhibited higher response magnitudes than the sensor with 2 μm intermediate layer shown in Figures 7.3, 7.4 and Table 7.1. At 290°C the measured response magnitudes for the sensor with the 1 μm SiN_x were more than twice than for those other sensor with 2 μm SiN_x for 1.00% H_2 concentrations.

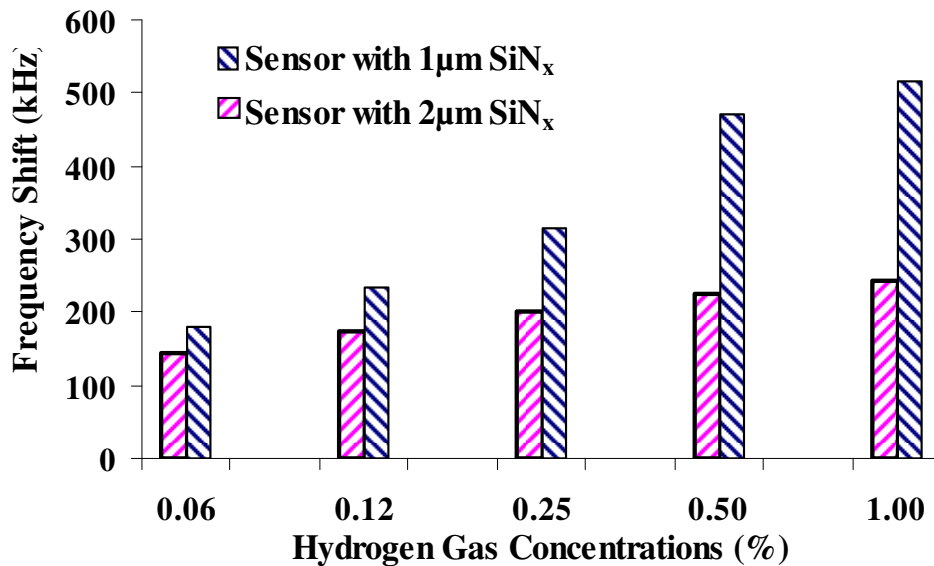


Figure 7.3 Hydrogen gas concentrations v. frequency shift for the layered SAW sensors with 1 and 2 μm PECVD SiN_x at 290°C

The recorded frequency shifts for 1% H_2 concentrations were 516 kHz for the sensor with 1 μm thick SiN_x layer, in comparison with 242 kHz for the other sensor. While still at the same temperature but at the lower concentration of 0.06% H_2 frequency shifts of 180 kHz and 145 kHz were recorded for the two sensors with 1 and 2 μm SiN_x , respectively.

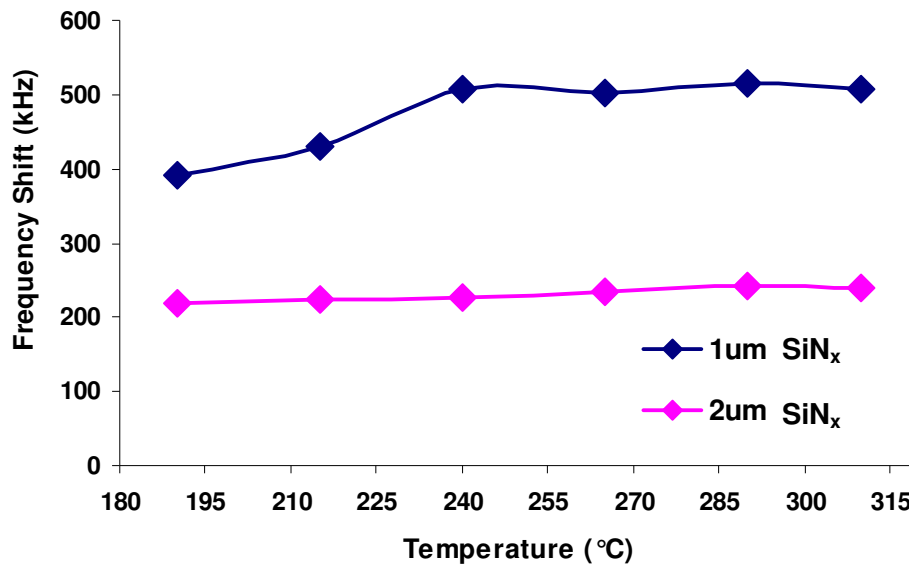


Figure 7.4 Frequency shift versus operational temperature of the layered SAW sensors with PECVD SiN_x intermediate layers for 1.00% H₂ concentrations in synthetic air

7.1.1.2 Sensor with a R.f. Sputtered Intermediate Layer (InO_x/SiN_xO_y/36°YXLiTaO₃)

Figure 7.5 shows the frequency shift versus the operating temperature of the SAW sensor with 1 μm r.f. magnetron sputtered intermediate layer. The sensor exhibits a decrease in the response magnitude with increasing temperature. The operational temperature range is between 145°C and 310°C, but the sensor presents stable, repeatable and reversible fast responses only above 215°C. At 240°C the sensor presents the fastest response and recovery of 30 and 70 seconds, respectively. The measured frequency shifts of 131 kHz for 0.06% H₂, 262 kHz for 0.25% H₂ and 290 kHz for 1.00% H₂ (Figure 7.6 a) were recorded.

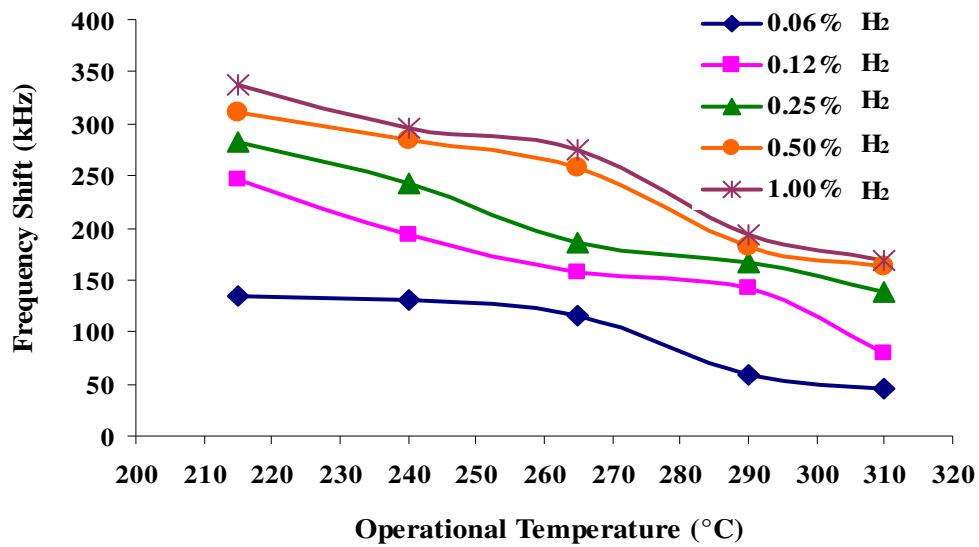
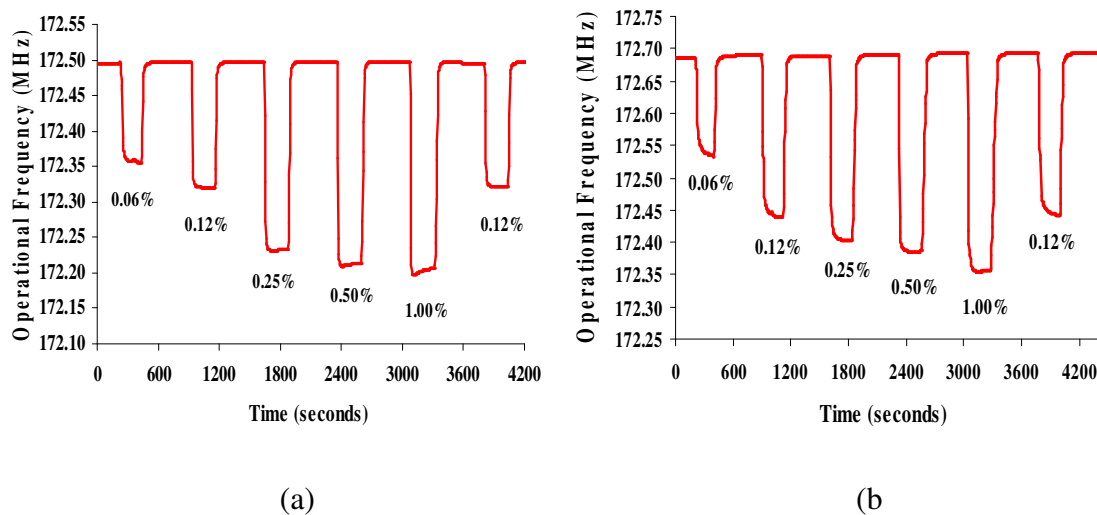
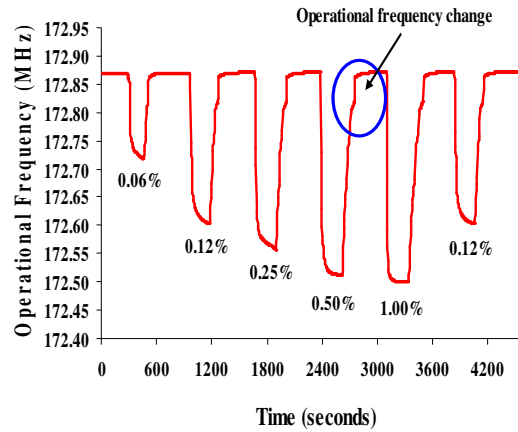


Figure 7.5 Frequency shift versus operating temperature for the layered SAW sensor with 1 μm r.f. magnetron sputtered intermediate layer

Although a larger response magnitude were observed at 215°C, the sensor suffers from poor reversibility and reproducibility at this temperature as well as having a longer response and recovery time, more than 120 seconds (Figure 7.6 b).

In addition unstable responses were observed below 215°C, which can be seen clearly at 190°C in Figure 7.6 c in the circled data point. Also it can be seen that the sensor is starting to saturate at concentrations above 0.25% at operational temperatures below 240°C.





(c)

Figure 7.6 Dynamic response of the SAW sensor with r.f. magnetron sputtered intermediate layer towards a H_2 pulse sequence at different operational temperatures at: (a) 240 °C, (b) 215°C and (c) 190°C

7.1.1.3 Sensor with E-beam Evaporated Intermediate Layer ($InO_x/SiN_x/36^\circ YLiTaO_3$)

When the SAW sensor was exposed to the H_2 pulse sequence the response magnitude increased linearly with the operating temperature until 290°C as shown in Figure 7.7. In the temperature range of between 190°C and 310°C the sensor exhibited stable, repeatable and reversible responses.

At the operational temperature of 290°C the largest frequency shifts of 360 kHz for 0.06% H_2 , 417 kHz for 0.25% H_2 and 465 kHz for 1.00% H_2 in air were recorded. Also the response and recovery of 60 and 70 seconds was observed at this temperature. As it can be seen from Figure 7.8 the sensor starts to saturate at concentrations greater than 0.12%

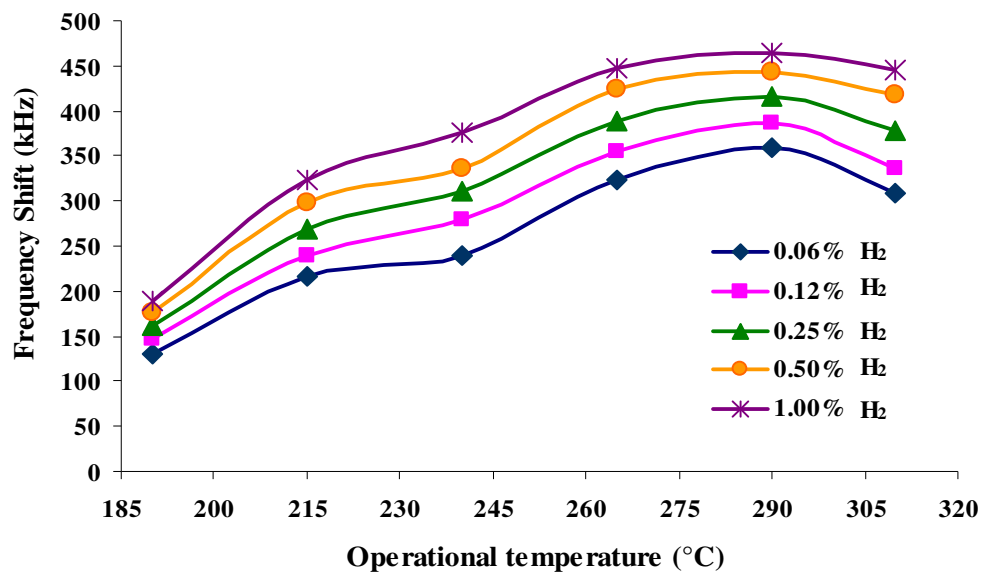


Figure 7.7 Frequency shift versus operational temperature for layered SAW sensor with E-beam evaporated 1 μm SiN_x intermediate layer

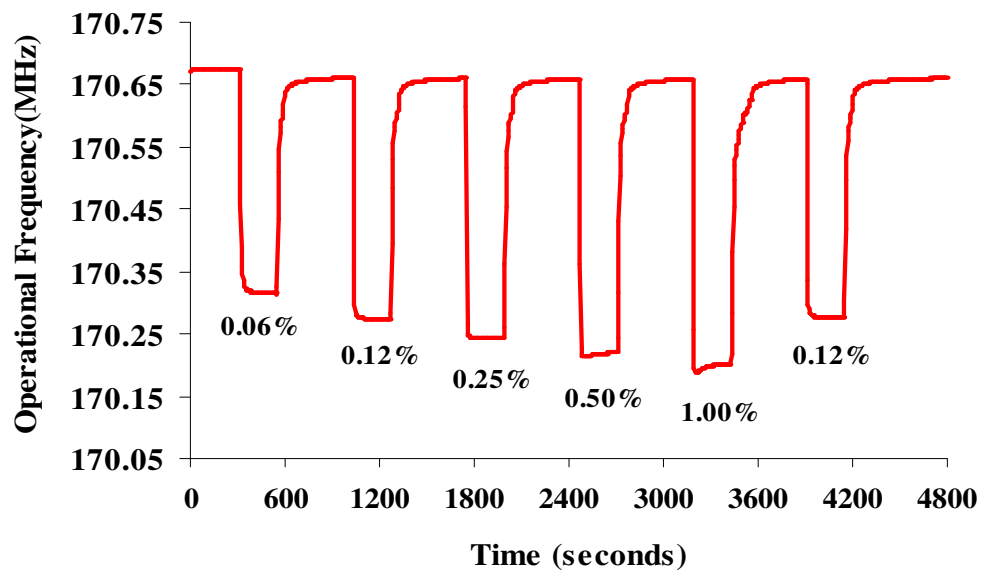


Figure 7.8 Dynamic response of the layered SAW sensor with E-beam evaporated 1 μm SiN_x intermediate layer towards a sequence of H₂ pulse at 290°C

7.1.1.4 Comparative Analyses of the H₂ Gas Sensing Results

The experimental test results show that the developed layered SAW gas sensors exhibit excellent static performances, e.g. repeatable, reversible and stable, large responses towards hydrogen. The XPS results presented in Chapter 6 revealed non-stoichiometric silicon nitride intermediate layers for all deposition techniques: SiO₂/SiN (PECVD), SiO_xN_y (r.f. magnetron sputtering) and Si-rich film (E-beam evaporation). Accordingly there is a difference in the response magnitude, operational temperature range as well in the response and recovery time of the sensors. The InO_x sensitive layers exhibited to some extent different oxygen deficiency as well as they have a slightly different carrier concentration (details can be found in section 6.12 of chapter 6 and Table 3.1 of Chapter 3). It is believed that the above mentioned gas sensing behavioural dissimilarities can be attributed mainly to the differences in the material properties of the intermediate layers (e.g. chemical composition, permittivity) and partially to the above mentioned difference in the level of carrier concentrations of the gas sensitive layers.

The test results of the SAW sensors with 1 and 2 μm SiN_x have shown a decrease in the response magnitude with the increase of the thickness of the intermediate layer (e.g. from 516 kHz to 242 kHz for 1% H₂) and an increase in the recovery time (from 90 to 120 seconds).

Table 7.2 shows a summary of experimental gas sensing results of the layered SAW sensors with 1 μm thick intermediate layers. Highlighted (with broken lines) are the frequency shifts at the temperature when the highest response magnitudes were recorded as well as the fastest response for each sensor. It can be seen that the largest response magnitudes were recorded by the sensor with the PECVD intermediate layer and it also had the largest operational

temperature range, between 125°C and 310°C. At the working temperature of 290°C large frequency shifts of 176.9 kHz were observed at 0.06% H₂ concentration and 516 kHz at 1.00% H₂. The micro-characterisation result revealed that this sensor has a very different: i) stoichiometry, ii) measured sheet conductivity (8.33×10^{-6}) and iii) carrier concentrations (5.80×10^{-16}) compared to the other two sensors. The simulations have also showed higher K^2 for this SAW sensor when the 1 µm PECVD Si₃N₄ intermediate layer was used.

In comparison, Jakubik et al. [153] have reported a SAW hydrogen sensor with a bilayer structure (thin metal-free phthalocyanine and palladium layers) with high resolution and a frequency shift of ~1.75 kHz in the concentration range of 1.5 – 4.0% H₂ in air. More recently Ippolito et al. [63] have reported a frequency shift of 514.7 kHz for 1.00% H₂ in synthetic air for a layered SAW based sensor with a 40 nm InO_x sensitive and ZnO intermediate layers on a XZ LiNbO₃ substrate at the working temperature of 308°C and a 319.4 kHz at the working temperature of 243°C. The same authors have reported also a layered SAW with a 200 nm thin InO_x sensing layer deposited on XZ LiNbO₃ as well as a 160 nm thin WO₃ deposited on ZnO/36°YX LiTaO₃ [154]. The measured frequency shifts for 1.00% H₂ were 61.3 kHz at 246°C for the sensor with InO_x sensing layer and 24.7 kHz at 186°C for the other sensor. A comparison of the response magnitudes of the layered SAW based gas sensors from the published literature with the sensors developed by the author can be found in Table 7.6 of section 7.4.

The sensor with the E-beam evaporated intermediate layer also had the largest response magnitudes at 290°C. For 1.00% H₂ 463.3 kHz frequency shift and for the 0.06% also large frequency shift of 359 kHz was recorded. It seems that this sensor exhibits an inclination to saturate at higher concentration than 0.12% H₂.

The third SAW sensor type (i.e. with the r.f. magnetron sputtered intermediate layer) is the only one which response magnitudes decreased with the increase of the operational temperature. However at 190°C still a large frequency shift was recorded (i.e. 360 kHz for 0.06% H₂).

Table 7.2 Summary of the H₂ sensing results for three layered SAW sensors with 1 µm thick intermediate layers

SAW Sensor with PECVD SiN _x							
Hydrogen Concentration (%)	Frequency Shift (kHz)						
0.06	37.8	38.3	39.1	79.9	122.9	179.6	212.5
0.25	112.7	123.4	140.7	210.2	307.6	315.1	391.5
1.00	365.1	390.8	429.4	507.0	503.3	516.0	506.8
Operational Temperature (°C)	165	190	215	240	265	290	310
SAW Sensor with RF Magnetron Sputtered SiN _x							
Hydrogen Concentration (%)	Frequency Shift (kHz)						
0.06		136.9	133.1	133.2	115.3	46.0	58.3
0.25		289.1	282.0	261.7	185.6	167.6	138.9
1.00		361.7	337.3	296.2	274.5	188.1	169.5
Operational Temperature (°C)	165	190	215	240	265	290	310
SAW Sensor with Electron Beam Evaporated SiN _x							
Hydrogen Concentration (%)	Frequency Shift (kHz)						
0.06	14.9	129.7	216.4	239.8	322.5	358.9	58.3
0.25	117.6	161.2	269.2	309.9	389.3	416.8	378.9
1.00	120.5	189.6	323.3	376.5	448.0	463.3	444.9
Operational Temperature (°C)	165	190	215	240	265	290	310

Table 7.3 Summary of the H₂ gas sensing results of a non-layered SAW sensor

SAW Sensor without intermediate layer							
Hydrogen Concentration (%)	Frequency Shift (kHz)						
0.06	14.3	18.4	17.4	The device is not operational			
0.25	64.9	72.4	51.7				
1.00	96.1	148.6	93.2				
Operational Temperature (°C)	160	182	200	240	265	290	310

Table 7.3 shows the response magnitudes of a SAW sensor without an intermediate layer. It is clear that the frequency shifts are considerably less for all concentrations as well as the operational temperature ranges being less compared with the layered SAW sensors where an intermediate layer is employed. In addition this SAW sensor was not operational when the working temperature was increased above 200°C. Repeatable and reversible responses were recorded between 130°C and 200°C but the sensor was unstable.

7.1.2 Ozone Sensing Results

The layered SAW sensors were exposed to O₃ concentrations between 20 and 150 ppb. The testing started at room temperature when the sensors were exposed to the highest available O₃ gas concentration. As the sensors did not respond, the heater temperature was increased up to 310°C and it was kept at this value for 3 hours before being exposed again to a few pulses of the highest O₃ concentrations. In comparison with H₂ testing the first responses for O₃ were recorded after three days of a “break-in period”, while the cycling of the sensors was carried out by exposing to O₃ concentrations every 3 hours.

When the SAW based sensor is exposed to an oxidizing gas such as O₃, the conductivity of the InO_x film decreases. Electrons are removed from the conduction band forming oxygen vacancies, which result in an increase of the acoustic wave velocity. Hence this change can be observed as an increase in the oscillation frequency (Figure 7.9) as opposed to a decrease in frequency for reducing gases like H₂.

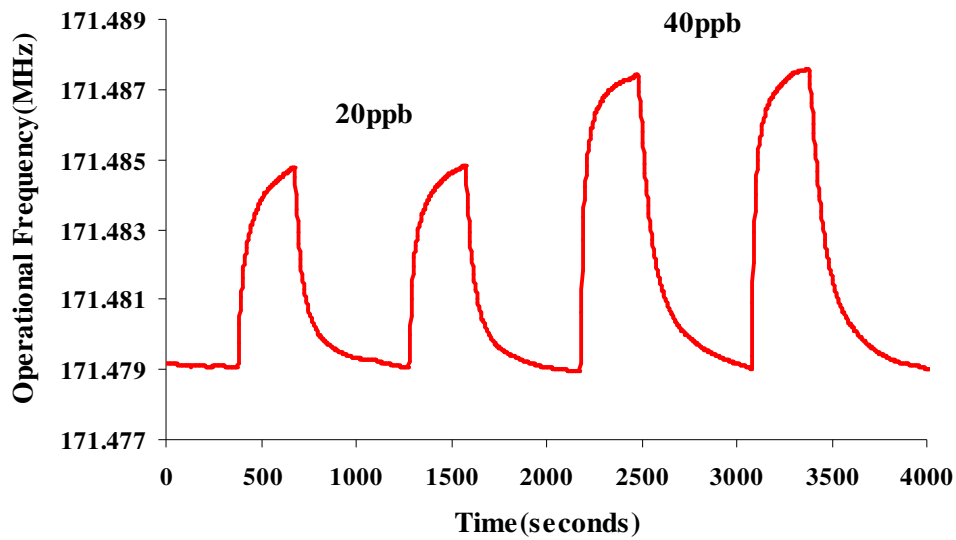


Figure 7.9 Dynamic response of a layered SAW sensor when it is exposed towards an oxidizing gas (O_3)

7.1.2.1 Sensor with PECVD Intermediate Layer ($SnO_x/SiO_2/SiN_x/36^\circ YLiTaO_3$)

A layered SAW sensor with $1\ \mu m$ SiN_x was tested towards O_3 concentrations by exposing it to a pulse sequence of 20 and 40 ppb using a computer controlled ozone generator. The responses were stable (baseline frequency stability was approximately 90-120 Hz) reversible and repeatable in the temperature range between $135^\circ C$ and $220^\circ C$. Figure 7.10 shows the frequency shifts recorded at different operating temperatures.

It can be seen that the response magnitudes increases with increase in temperature from $135^\circ C$ to $195^\circ C$, exhibiting the highest response magnitudes at $195^\circ C$ and with further increase of the temperature, above $200^\circ C$, there is a sudden decrease in the frequency shifts. The sensor was operational until $240^\circ C$ but the recorded responses were not repeatable and reversible and instability in the baseline frequency was observed.

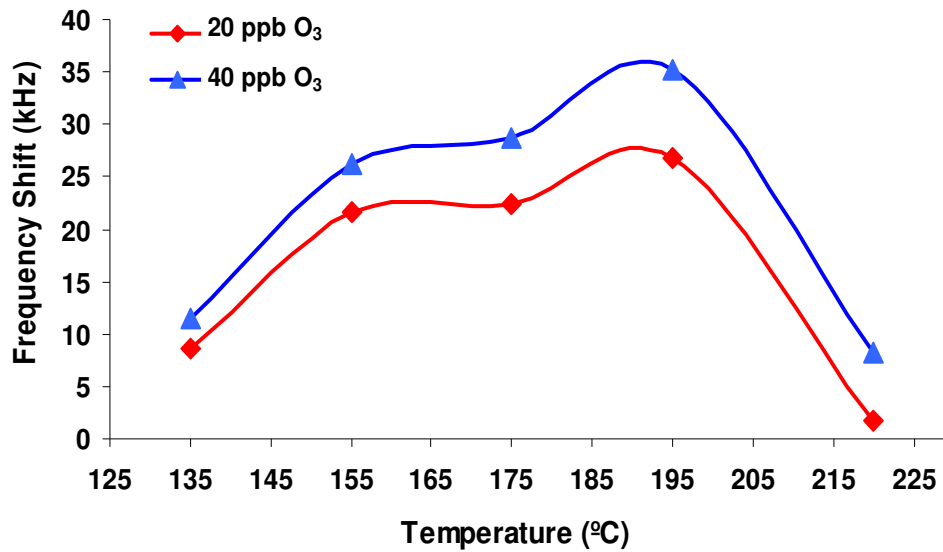


Figure 7.10 Frequency shift versus operational temperature for the layered SAW sensor with a PECVD SiN_x intermediate layer, towards different O₃ concentrations

Figure 7.11 shows the dynamic response of this sensor at the working temperature of 195°C, as well as at 220°C. The frequency shifts recorded at 195°C were 27 and 36 kHz for 20 and 40 ppb O₃ concentrations, and at 220°C at the same concentrations the obtained frequency shifts were 1.8 and 8.2 kHz, respectively. At 195°C the response time was around 3.5 minutes and the recovery time was less than 8 minutes. At 220°C the recovery time of the sensor increased to 10 minutes and at 135°C it was more than 30 minutes.

At the temperature of 195°C the sensor presented unstable responses. This can be seen clearly in Figure 7.11 (a) in the circled areas, on the recovery part of the graph, after the ozone gas was switched off. This is caused by a sudden change in the operational frequency of the sensor. Figure 4.6 from Chapter 4 showed the frequency response and the resonant peaks of this sensor at three stages of fabrication process. Figure 7.12 shows this frequency response and in circled area the influence of the Triple Transit Echo (TTE). The ripples of TTE are caused by the mechanical reflections and electrical regeneration of the IDTs. The author

believes that the TTE effect is the cause of the unstable responses as the operational frequency of the SAW device can change unexpectedly, or “jump“, from one peak of the ripple to the other (in close proximity of the resonant peak) when the ozone gas is switched off. TTL can be reduced by careful design; however a trade-off has to be applied between the removal of this effect and the insertion loss of the device.

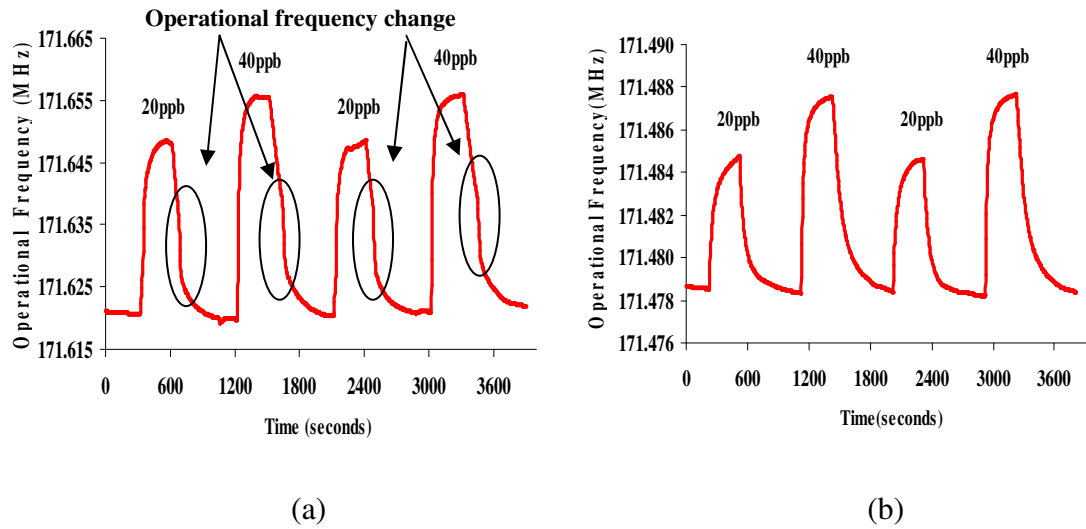


Figure 7.11 Dynamic response of a layered SAW sensor with a PEVCD SiN_x intermediate layer, towards O₃ at two different operational temperatures at: (a) 195°C and (b) 220°C

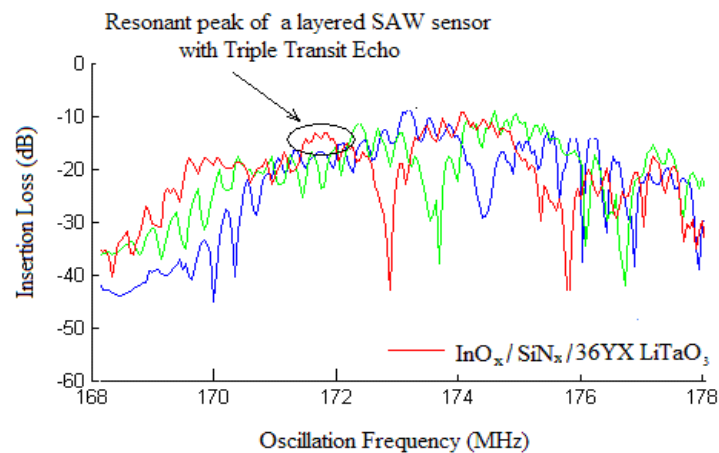


Figure 7.12 Frequency response of a SAW sensor (red line) showing the influence caused by the Triple Transient Echo (TTR)

7.1.2.2 Sensor with R.f. Sputtered Intermediate Layer ($\text{InO}_x/\text{SiO}_x\text{N}_y/36^\circ\text{YXLiTaO}_3$)

The sensor was exposed to O_3 concentration of 25 ppb and 50 ppb between room temperature and 310°C . The sensor exhibited reproducible, reversible and stable responses for the temperature range 185°C to 205°C . Figure 7.12 shows the frequency shift versus temperature at these concentrations. The SAW device's sensitivity (response magnitudes) decreases above 190°C (Figure 7.12) and a deterioration of the sensor performance characteristics was observed above 205°C . Poorer reversibility and reproducibility with longer response and recovery as well as the instability of the baseline frequency was observed above this temperature. Figure 7.13 (a) and (b) shows the frequency responses at these concentrations at the temperatures of 190°C and 195°C . At 195°C , frequency shifts of 3.7 kHz and 5.1 kHz for 25 ppb and 50 ppb O_3 were observed. However larger frequency shifts of 5.0 kHz and 6.5 kHz were recorded for the same concentrations at 190°C . The sensor displayed response and recovery time of around 4 minutes and 7 minutes, respectively.

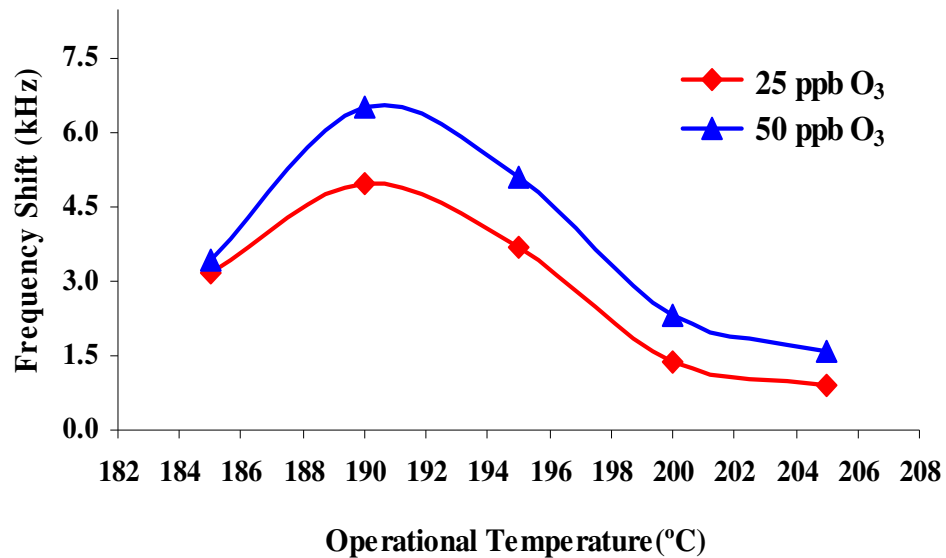


Figure 7.13 Frequency shift versus operational temperature for the layered SAW sensor, with r.f. magnetron sputtered intermediate layer, for two different O_3 concentrations.

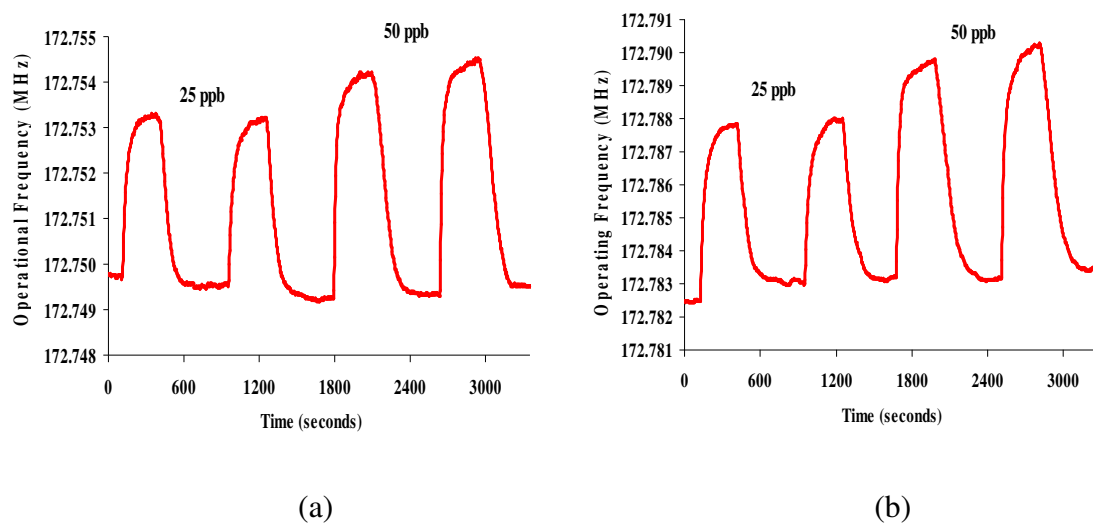


Figure 7.14 Dynamic response of a layered SAW sensor with a r.f. magnetron sputtered intermediate layer, towards O_3 at two operational temperatures: (a) 195°C and (b) 190°C

7.1.2.3 Sensor with E-beam Evaporated Intermediate Layer ($InO_x/SiN_x/36^\circ YXLiTaO_3$)

The first responses were observed around 160°C but repeatable, reversible and stable responses were recorded above 200°C. In Figure 7.14 it can be seen that response magnitudes decreases with increasing temperature and the highest frequency shift was obtained at 215°C. The sensor exhibits at this temperature, reversible, repeatable responses and frequency shifts of 56 kHz for 20 ppb and 92 kHz for 40 ppb O_3 (Figure 7.16 a) were recorded. As the temperature was increased to 240°C the responses reduced considerably and poorer reversibility and reproducibility were observed as shown in Figure 16 (b). As a comparison the frequency shifts 22.2 kHz for 20 ppb and 56.3 kHz for 40 ppb were recorded. As the results indicate this sensor would be suitable for sensing O_3 concentrations lower than 40 ppb when operating above 200°C. At 215°C the response time of approximately 13 minutes and the recovery time of 14 minutes were measured.

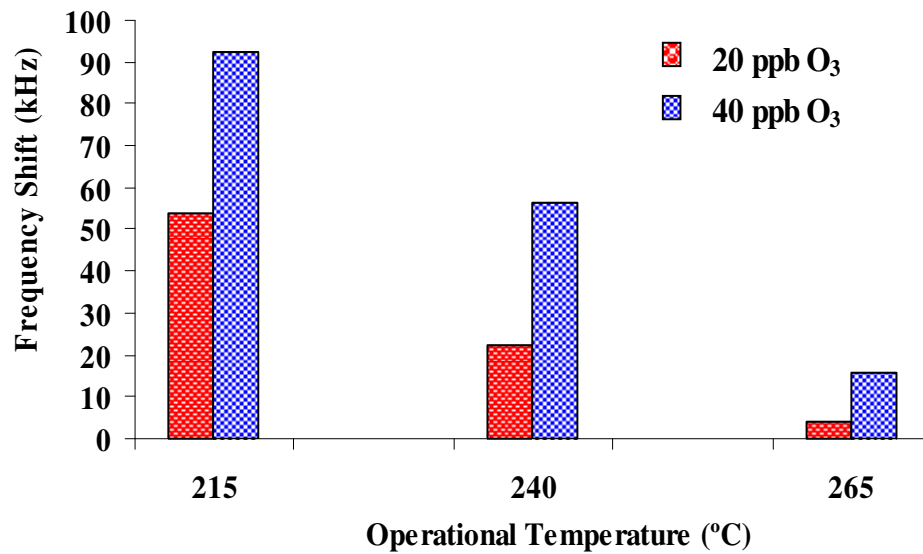


Figure 7.15 Frequency shift versus operational temperature for the layered SAW sensor with E-beam evaporated intermediate layer towards two different O₃ concentrations

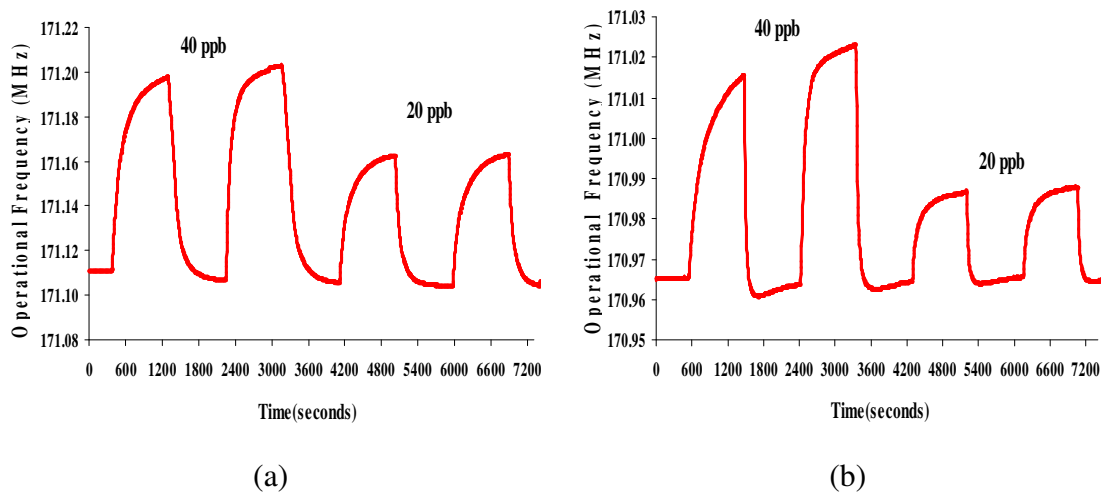


Figure 7.16 Dynamic response of a layered SAW sensor with E-beam intermediate layer towards O₃ at two operational temperatures: (a) 215°C and (b) 240°C

7.1.2.4 Comparative Analyses of the O₃ Gas Sensing Results

All developed sensors are capable of sensing ozone concentration as low as 20 ppb with repeatable, reversible and stable responses in the presented operational temperature range. The recorded frequency shifts are summarised in Table 7.2, which also shows the operational

temperature ranges of each SAW sensors, highlighting the temperatures (broken lines) when the largest responses were recorded. It can be seen clearly from this table that the sensors have different gas sensing characteristics such as are the operational temperature range , the response magnitudes as well as the response and recovery time of the sensors were also very different. This is not surprising taking into consideration that the previously presented test results for H₂ and the XPS results presented in Chapter 6, which point towards a different chemical composition for the intermediate layers. The discussion on the possible gas sensing mechanism related to these results is included in the next section.

Table.7.4 Summary of the O₃ gas sensing results of the layered SAW sensors

SAW Sensor with PECVD SiN _x						
Ozone Concentration (ppb)	Frequency Shift (kHz)					
20	8.6	21.6	22.5	26.8	1.8	-
40	11.5	26.2	28.7	35.3	8.2	4.2
Operational Temperature (°C)	135	155	175	195	220	240
SAW Sensor with RF Magnetron Sputtered SiN _x						
Ozone Concentration (ppb)	Frequency Shift (kHz)					
25	-	3.2	5.0	3.7	1.4	0.9
50	-	3.4	6.5	5.1	2.3	1.6
Operational Temperature (°C)	185	190	195	200	205	
SAW Sensor with Electron Beam Evaporated SiN _x						
Ozone Concentration (ppb)	Frequency Shift (kHz)					
20	-	-	-	53.7	22.2	3.8
40	-	-	-	92.4	56.3	15.7
Operational Temperature (°C)				220	240	265

7.1.3 Discussion

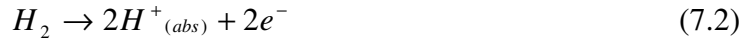
In Chapter 3 a general discussion on the SMO sensing mechanism was presented. Now the discussion will focus on the gas sensing mechanism related to the obtained test results.

The sensitivity of the InO_x can be attributed to the formation of oxygen vacancies in the films, which are correlated to the existence of oxygen deficiencies with respect to the stoichiometric composition. Thus by controlling the oxygen deficiency, the conductivity of InO_x films can be altered. In the case of the presented layered SAW gas sensors, with oxygen deficient InO_x sensitive layer, when they are exposed to a gas analyte a change in the conductivity of the InO_x layer takes place. This process of formation of doubly charged oxygen vacancies, which is responsible for the change in conductivity, can be described by the following equation [7]:

$$O_0 = V_0 + 2e^- + \frac{1}{2}O_2(gas) \quad (7.1)$$

where V_0 are the oxygen vacancies. From equation (7.1) it can be seen that the formation of oxygen vacancies will also lead to the formation of free electrons. The charged oxygen vacancies will become the electron trapping sites where electrons are available for conduction. Chemisorptions of the oxygen molecules take place on the surface of the layer during the interactions with the gas analytes. This can either increase or decrease the conductivity of the n-type InO_x layer depending on the nature of the gas species. If the gas analyte is an oxidizing gas such as O_3 an electron will be removed from the conduction band and the conductivity will decrease. This will result in the increase of the operational frequency of the SAW device. The opposite will take place in the case of a reducing gas such as H_2 ,

when electrons contributed increasing the conductivity of the InO_x film, and as a consequence the operational frequency of the SAW device will decrease. The dissociation of the H_2 molecules (in the case of a reducing gas) injecting electrons into the InO_x film surface can be written as [155,156]:



The conductivity of the InO_x is considered to be determined by the surface coverage of oxygen species (e.g. O^- , O_2^-) which acts as electron traps and the sensitivity is a function of the density of oxygen vacancies.

The sensitivity towards O_3 of the indium oxide occurs due to dissociation of O_3 molecules in the gas phase [156]. Takada et al. [9], for the first time, presumed that the decomposition of ozone into O_2 and O increases sensitivity towards ozone.

This mechanism can be written as:



The dissociated oxygen species of O^- , O_2^- remove electrons from the conduction band, which results in a decrease of the n-type InO_x film's conductivity:



As was presented above, for gas sensing applications an oxygen deficient non-stoichiometric InO_x is required. The XPS results presented in Chapter 6 confirmed that all InO_x films deposited by r.f. magnetron sputtering are non-stoichiometric with an 8-17% oxygen deficiency with an atomic ratio of $\text{O/In} \sim 1.0$. In fact Korotcenkov et al. [82] have reported that an increase of the deviation from stoichiometry will lead to an increase in the sensitivity towards O_3 . This facilitates the dissociation of the O_3 molecules and the presented test results prove the high sensitivity toward O_3 of the InO_x film.

There are a number of other factors which influences the sensitivity of the InO_x film such as surface morphology, crystallinity and film thickness. But one of the most important factors controlling the sensitivity of the metal oxide gas sensors is the grain size [118]. The grain-size effect models in conjunction with the space charge depth L_D was presented in Chapter 3. The models assume that the film is composed of a chain of uniform crystallites with size X_g connected with each other through necks and grain boundaries. When $X_g \gg 2L_D$ it was theoretically and experimentally shown that the resistance of the layer is dominated by the resistance of the grain boundaries (grain boundary control). The sensitivity of the polycrystalline material can be enhanced considerably when $X_g < 2L_D$. In this case the resistance of the necks between crystallites becomes important. Moreover the gas sensitivity of such layers can be further enhanced if $X_g \ll 2L_D$ resulting in the so called "flat band conditions". As a consequence, utilising a SMO sensitive layer with nanosized grains will produce highly sensitive devices. In fact an enhanced sensitivity toward the NO_2 was reported in the literature for the nanocrystalline InO_x thin films with grain sizes below 50 nm [133]. The InO_x films deposited by the author revealed (FE-SEM micrographs in Chapter 6) a polycrystalline compact layer with grain (crystallites) sizes between 20 and 40 nm.

As was stated at the beginning of this chapter the microcharacterisation results revealed that the InO_x thin films exhibit very promising gas sensing material features, (e.g. polycrystalline structure, chemical composition) which points towards a highly sensitive film for O_3 detection. This was confirmed by the experimental test results as the sensors are capable sensing O_3 concentrations as low as 20 ppb.

In contrast to the oxidising gases, with regard to the sensitivity of InO_x films for reducing gases the grain size is not a crucial factor [81]. This can be explained by the fact that the gas sensing mechanism of InO_x sensitivity include chemisorption, redox and catalytic effects involving the participation of the lattice oxygen ($\text{O}1s$ peak with $\text{BE} = 530.5\text{eV}$) with changes in stoichiometry [155]. The test results showed there are differences in the gas sensing behaviour (e.g. response magnitude, dynamic operating ranges) of the layered SAW sensors. These can be attributed again to the different chemical compositions of the intermediate layer.

The XPS results revealed a non-stoichiometric PECVD SiN_x layer as well on the top on this an approximately 30-40 nm thin film of SiO_2 was formed (the possible reason for this was explained in Chapter 4). The SAW sensor with the E-beam evaporated Si-rich intermediate layer has the same operating temperature range as the SAW with PECVD layers and also its response magnitudes increased with the increase of the temperature. In contrast, the SAW sensor with the r.f. magnetron sputtered intermediate layer (SiO_xN_y composition) with the increase of the temperature exhibits sensitivity decrease. The author's opinion is this gas sensing behaviour can be attributed to the presence of O_2 in the intermediate layer (SiO_xN_y). With the increase of the operational temperature, through the interaction of H_2 molecules with the SiN_xO_y layer the oxygen vacancies of the InO_x film will be changed. Hence a conductivity change will decrease the response magnitude.

Tables 7.1 and 7.2 clearly show the importance of the intermediate layer. The non-layered SAW device was not operational above 200°C and also presented smaller response magnitudes. The author's opinion is that with the increase of the operational temperature the sensitive layer of InO_x inhibits the operation (oscillation) of the SAW device due to conductive loading resulting in electrical shorting the metal electrodes of the IDTs.

7.2 Conductometric Sensor with SnO_2 Nanorods Sensitive Layer

As mentioned previously (in Chapter 2) the author has initiated the investigation of the synthesis of 1-D nanostructures and their application for gas sensing. The novel method of “sputter redeposition” (described in detail in chapter 6) was employed to deposit SnO_2 nanorod layers on LiTaO_3 transducers. In this section the gas sensing performance of the developed conductometric sensor will be presented. The sensor was tested towards an oxidizing (NO_2) gas as well as towards a reducing gas (CO).

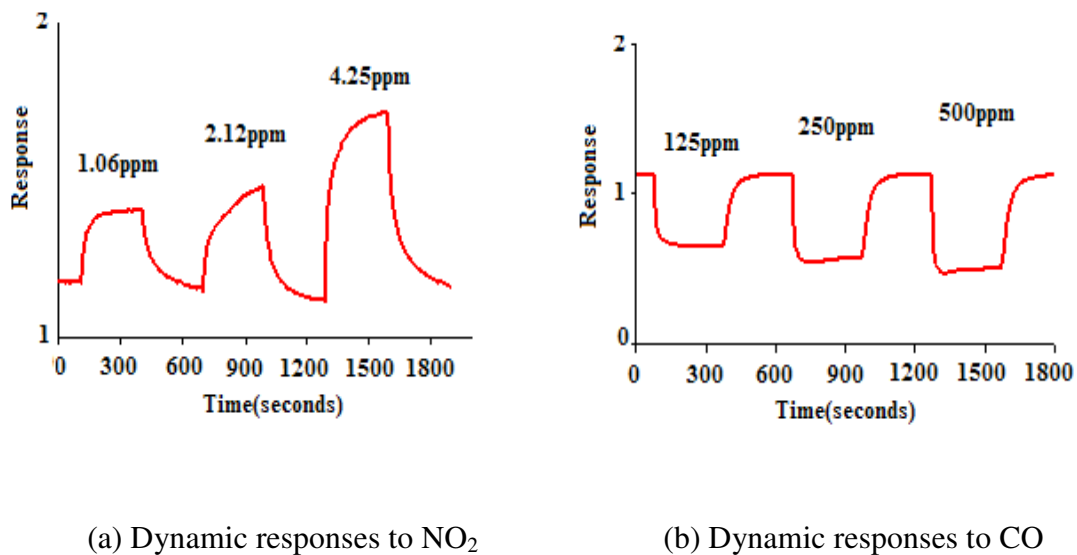


Figure 7.17 Dynamic responses for the conductometric sensor at 280°C towards: (a) oxidizing (NO_2) and (b) reducing (CO) gas

The time response of a conductometric sensor can be defined for an n-type semiconductor material such as SnO₂ using differential expressions as follows:

- *Reducing gas*

$$S_R = \frac{d}{d_{crg}} \left(\frac{R_{gas}}{R_{air}} \right), \quad (7.6)$$

- *Oxidizing gas*

$$S_O = \frac{d}{d_{cog}} \left(\frac{R_{gas}}{R_{air}} \right) \quad (7.7)$$

where R_{gas} is the resistance in reducing or oxidizing gas, R_{air} is the resistance in air, d_{crg} and d_{cog} stands for concentration of reducing gas and oxidizing gas, respectively.

The sensor was tested towards the gas analytes from room temperature to 300°C. As SnO₂ is an n-type semiconductor material, the CO reducing gas was found to increase conductivity, while the opposite occurred for NO₂, shown in Figures 7.17 (a) and (b). Reversible, repeatable stable responses were recorded in the temperature range of 200 – 300°C for 125 - 500 ppm CO and 1.06 - 4.25 ppm NO₂, respectively. The response time increased with the operational temperature until 280°C, where the highest response was recorded. The response time for CO was less than 50 seconds.

7.2.1 Discussion

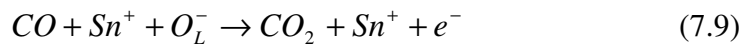
The results obtained for CO can be attributed to the surface morphology of the deposited SnO₂ nanorod thin film which was presented in the previous chapter. The FE-SEM micrograph showed needle-like shape nanorod with dense distribution on the entire surface

(substrate and metal electrodes). The XTEM lattice and HRTEM images confirmed that the nanorods are composed of single crystals with nanosized dimensions. In addition the nanorods presented a preferential orientation and the XRD analyses revealed a rutile-type structure.

Regarding the gas sensing mechanism, in the case of CO and NO₂ the dominant mechanism is chemisorption. For NO₂ the direct chemisorption reaction that occurs [156] is:



The NO₂ molecule removes an electron from the conduction band resulting in a decrease in the SnO₂ film conductivity. In the case of CO sensing the redox mechanism with the consumption of lattice oxygen takes place. Oxygen vacancies partially are formed in the oxide lattice (O_L^-) with the interaction of CO. For SnO₂ this process can be written as [156]:



The CO can react with the absorbed oxygen species O^- , O_2^- on the surface of the SnO₂ film such that [156]:



In both cases in the presence of CO, one electron is injected in the conduction band increasing the film's conductivity [157]. It seems that on the surface of the SnO₂ thin layer, there are

oxygen vacancies for chemisorption sites as well a crystalline structure (single crystals with preferential orientation) which assists a fast interaction of the CO molecules with the absorbed oxygen species. Thus the sensor has a fast response facilitated by the nanostructured SnO₂ sensing layer morphology formed by single crystals where the gas molecules can have a fast diffusion rate. As was mentioned, this is the first approach to employ a nanorod layer of SnO₂ deposited on transducers with LiTaO₃ substrate and the preliminary test results are promising. Although additional work needed to optimize the thickness of the SnO₂ nanorod film to further increase the gas sensitivity of the device.

7.3 Concluding Remarks

Table 7.5 shows the non-layered SAW based gas sensors and Table 7.6 (updated from [158]) the layered SAW gas sensors, highlighted in bold characters are the sensors developed by the author.

Table 7.5 Non-layered SAW based Gas Sensors (updated from [158])

Non-layered SAW based Gas Sensors				
Gas Sensitive Layer	Substrate	Analyte Gas	Frequency Shift (Hz)	Reference
WO ₃ :Ru	24°Y Quartz	3 ppm NO	50,000	[159]
Doped WO ₃	YZ LiNbO ₃	30 ppm H ₂ S	10,000	[160]
WO ₃ :Au	YZ LiNbO ₃	100 ppm H ₂ S	5,000	[41]
Metal-phthalocyanine	-	1.4 ppm NO ₂	8	[161]
Lead phthalocyanine	YZ LiNbO ₃	10 ppm NO ₂	154	[11]
Catalysed lead phthalocyanine	YZ LiNbO ₃	10 ppm NO ₂	330	[11]
Tetra-4-tert butyl silicon phthalocyanine dichloride	ST quartz	100 ppm NO ₂	420	[162]
Lead phthalocyanine	YZ LiNbO ₃	3.1 ppm of NO ₂	9,500	[163]
WO ₃	27° Quartz	10 ppm of H ₂ S	4,000	[164]
WO ₃	YZ LiNbO ₃	27 ppm of H ₂ S	9,900	[160]
Pt/WO ₃	langasite	1000 ppm H ₂ S	6,000	[165]
InO_x	36°YXLiTaO₃	600 ppm H₂	18,400	N/A

From these tables it can be seen that the developed layered SAW sensors for a reducing gas such as hydrogen have at least 7 times higher response magnitudes than for a non-layered SAW sensor for 600 ppm H₂ (17.4 to 136.9kHz) and 3.8 times more for 10,000 ppm H₂ (361.7 to 93 kHz) at an approximate 200°C working temperature. The operating temperature ranges of the layered SAW sensor are also higher than those of the non-layered SAW sensor, which was not operational above 200°C.

Table 7.6 Layered SAW based Gas Sensors (updated from [159])

Layered SAW based Gas Sensors				
Gas Sensitive Layer	Intermediate layer/ Substrate	Analyte gas	Frequency shift (Hz)	Reference
TiO ₂	SiO ₂ / ST quartz	10000 ppm O ₂ \	45,000	[166]
ZnO	ZnO/90° ST quartz	50 ppm O ₂	11,000	[167]
ZnO	ZnO/90° rotated ST quartz	100 ppm C ₂ H ₈	11,000	[167]
Palladium	copper phthalocyanine/ YZ LiNbO ₃	2.00 % H ₂	1,000*	[61]
Palladium	phthalocyanine/ YZ LiNbO ₃	2.00 % H ₂	5,000*	[62]
Copper phthalocyanine	SiO ₂ /90° ST quartz	1ppm NO ₂	1,400	[168]
WO ₃	ZnO/36° YX LiTaO ₃	500 ppm ethanol	119,000	[169]
WO ₃	ZnO/36° YX LiTaO ₃	1% H ₂	24,700	[170]
Au-WO ₃	ZnO/36° YX LiTaO ₃	1% H ₂	755,000	[171]
SWCNTs	SiO ₂ /ST X Quartz	50ppm of Isopropanol	8,000	[172]
40 nm thin InO _x	ZnO/36° YX LiTaO ₃	10,000 ppm H ₂ 600 ppm H ₂	514,700 338,700	[63]
200 nm thin InO _x	ZnO/36° YX LiTaO ₃	10,000 ppm H ₂ 600 ppm H ₂	61,300 5,700	[63]
100 nm thin InO _x	SiO ₂ /SiN _x /36° YX LiTaO ₃	10,000 ppm H ₂ 600 ppm H ₂	516,000 179,600	
100 nm thin InO _x	SiO _x N _y /36° YX LiTaO ₃	10,000 ppm H ₂ 600 ppm H ₂	463,300 358,900	Reducing Gas
100 nm thin InO _x	SiN _x /36° YX LiTaO ₃	10,000 ppm H ₂ 600 ppm H ₂	361,700 136,900	
100 nm thin InO _x	SiO ₂ /SiN _x /36° YX LiTaO ₃	20 ppb O ₃ 40 ppb O ₃	26,800 35,300	
100 nm thin InO _x	SiO _y N _x /36° YX LiTaO ₃	25 ppb O ₃ 50 ppb O ₃	5,000 6,500	Oxidizing Gas
100 nm thin InO _x	SiN _x /36° YX LiTaO ₃	20 ppb O ₃ 40 ppb O ₃	53,700 92,400	

To the author's best knowledge that there are no layered SAW sensors in the published literature for O_3 sensing applications. The sensor with $InO_x/SiO_2/SiN_x/36^\circ YXLiTaO_3$ structure has a response time similar for ozone (3.5 minutes) that of the portable OZONE HUNTER PLUS (AET-030P) ozone monitoring device (recently developed by New Electric Cosmos Ltd [173]) which has an approximately 3 minutes response time.

As it was outlined in Chapter 1, a layered SAW sensor can present a number advantages over the non-layered SAW counterparts. An appropriate intermediate layer (e.g. thickness, choice of material) deposited between the substrate and the gas sensitive layer can result in increased response magnitudes (sensitivity), and can provide a protective role for the IDTs. In Chapter 2 it was presented the proposed layered SAW structure and in Chapter 3 was followed by the presentation of the author's method in the selection of the intermediate and gas sensitive layer thicknesses. Unexpectedly the microcharacterisation results revealed a non- stoichiometric composition of the intermediate layers deposited by r.f magnetron sputtering and a desirable non-stoichiometric gas sensitive indium oxide layer.

The simulation were performed with the stoichiometric material constants, since consistently the microcharacterisation results showed a similar non- stoichiometric composition (SiO_xN_y) the author used a trade-off between the simulation and experimental results to determine the thickness of the intermediate layer. The obtained gas sensing results justifies that the design method used by the author was correct; the developed layered SAW sensors are capable to sense ozone concentration in the low ppb range (less than 20 ppb).

7.4 Summary

In this chapter the experimental test results of the $\text{InO}_x/\text{SiO}_2/\text{SiN}_x/36^\circ\text{YXLiTaO}_3$, $\text{InO}_x/\text{SiN}_x\text{O}_y/36^\circ\text{YXLiTaO}_3$ and $\text{InO}_x/\text{SiN}_x/36^\circ\text{YXLiTaO}_3$ layered SAW structures and of the $\text{SnO}_2/36^\circ\text{YXLiTaO}_3$ nanorod based conductometric sensor were presented. Previously the microcharacterisation results showed promising gas sensing material features of the deposited sensitive layers InO_x thin film which were confirmed by the obtained test results. The layered SAW sensors presented repeatable, reversible and stable responses when they were exposed to H_2 and O_3 . Regarding their sensitivity all sensors are capable to sense 20 ppb of O_3 and 600 ppm of H_2 .

The key experimental gas sensing performance characteristics for the three layered SAW and a non-layered SAW structures can be summarised in the following:

1. $\text{InO}_x/\text{SiO}_2/\text{SiN}_x/36^\circ\text{YXLiTaO}_3$ (with PECVD intermediate layer)

(a) H_2 sensing

- largest response magnitude when compared with the three sensors and e.g. 516 kHz for 1.00% H_2 at 290°C
- largest operating temperature ranges of 135°C to 310°C compared with the other three SAW sensors,
- response and recovery of 35 seconds and of 70 seconds
- the response magnitudes increased linearly with the increase of the temperature
- the sensor with 1 μm intermediate layer presented more than twice higher frequency shift than the sensor with 2 μm intermediate layer, e.g. for 0.5% and 1.00% H_2 concentrations

(b) O₃ sensing

- largest operating temperature ranges of 135°C to 240°C compared with the other two layered SAW sensors
- the structure with 1 μm intermediate layer exhibited 35 kHz frequency shift for O₃ at 195°C
- fastest response time, less 3.5 minutes and a recovery time of 7 minutes

2. InO_x/SiO_xN_y/36°YXLiTaO₃ (with r.f. magnetron sputtered intermediate layer)

(a) H₂ sensing

- operational temperature ranges of 190°C to 310°C
- lowest frequency shift for H₂ and when compared with the other two layered structures (e.g. 362 kHz at 190°C)
- response and recovery time of 30 and 70 seconds
- the response magnitudes decreased with the increase of working temperature

(b) O₃ sensing

- operational temperature ranges between 185°C and 205°C
- lowest frequency shifts for O₃ when compared with the other two layered structures
- response and recovery of 4 and 8 minutes

3. InO_x/SiN_x/ 36°YXLiTaO₃ (with E-beam evaporated intermediate layer)

(a) H₂ sensing

- operational temperature ranges between 165°C and 310°C
- frequency shift of 461 kHz at 290°C for 1.00 % H₂
- recovery and response time of 60 and 70 seconds

- the response magnitude increased with the increase of operational temperature

(b) O_3 sensing

- operational temperature ranges 200°C and 240°C
- the highest frequency shift was measured of 92 kHz for 40 ppb O_3 at 220°C when compared with the other two layered structures
- response and recovery time were of 13 and 14 minutes

4. $InO_x/36^\circ YXLiTaO_3$

(a) H_2 sensing

- less than half frequency shifts were recorded in comparison with the presented layered SAW sensors, e.g. 93 kHz at 200°C for 1.00% H_2 , in comparison frequency at 190°C the frequency shift of 189 kHz were recorded for the sensors with $36^\circ YXLiTaO_3/SiN_x/InO_x$ structure
- above 200°C the device was not operational

(b) O_3 sensing

- no responses were recorded

The experimental test results provide strong evidence that using these structures high sensitivity can be achieved for gas sensing applications, primarily for sensing low concentrations of O_3 .

To the best knowledge of the author, this is the first time when a layered SAW based gas sensor was developed with $InO_x/SiN_x/36^\circ YXLiTaO_3$, $InO_x/SiO_2/SiN_x/36^\circ YXLiTaO_3$ and $InO_x/SiO_xN_y/36^\circ YXLiTaO_3$ structures.

Chapter 8

Conclusions and Future Work

This research program commenced with the aim to develop a novel layered SAW based ozone and hydrogen sensors. Three layered SAW structures: $\text{InO}_x/\text{SiO}_2/\text{SiN}_x/36^\circ\text{YXLiTaO}_3$, $\text{InO}_x/\text{SiN}_x\text{O}_y/36^\circ\text{YXLiTaO}_3$ and $\text{InO}_x/\text{SiN}_x/36^\circ\text{YXLiTaO}_3$ were fabricated by employing the PECVD, r.f. magnetron sputtering and E-Beam evaporation techniques for the intermediate layer deposition and r.f. magnetron sputtering was used for the deposition of the indium oxide gas sensitive layer. Additionally a conductometric sensor with a thin layer of SnO_2 nanorods was produced for CO and NO_2 . This thesis presents the gas sensing performance of the developed gas sensors.

The gas sensing results showed that the layered SAW and conductometric sensors exhibited very stable, repeatable, reversible and fast responses. Furthermore the layered SAW sensors have the potential to sense concentrations as low as 20 ppb of O₃ and 600 ppm of H₂. Hence the author has demonstrated that the objectives outlined in Chapter 1, section 1.2 have been accomplished.

This thesis presents the evolution of the author's research which can be summarised by the following points:

1. reviewing the literature and proposing the InO_x/Si₃N₄/36°YXLiTaO₃ layered SAW based sensor
2. fabrication of layered SAW transducers on LiTaO₃ substrate and establishing the deposition parameters for the intermediate and gas sensitive layers
3. establishing of the appropriate thickness of the intermediate layer utilising simulation results and experimental verification
4. microstructural characterisation of the deposited sensors' layers to examine their chemical composition, structural and surface morphology for gas sensing applications followed by testing the layered SAW and conductometric devices towards different reducing (e.g. H₂, CO) and oxidising (e.g. O₃, NO₂) gas analytes

In the following two sections, the author will summaries the major findings of this research (section 8.1) and will present his suggestions for future work (section 8.2).

8.1 Conclusions

This research resulted in several outcomes which can be summarised in the following points:

Layered SAW Sensors

- The novel layered SAW based sensors exhibited very stable, reversible, repeatable (reproducible) responses for H_2 and O_3 . Higher response magnitudes were obtained for the SAW sensor with $InO_x/SiO_2/SiN_x/36^\circ YLiTaO_3$ structure compared with responses reported in the literature for other layered SAW device (see chapter 7, Table 7.5). This sensor has an operational temperature range of $135^\circ C$ and $310^\circ C$ for H_2 and between $135^\circ C$ and $240^\circ C$ for O_3 . The sensor responded in less than 3.5 minutes. In comparison the portable OZONE HUNTER PLUS (AET-030P) ozone monitoring device, which was recently developed by New Electric Cosmos Ltd [173] has a response time of approximately 3 minutes. In addition this sensor exhibits long term stability, e.g. the sensor produced the same response magnitudes when it was tested after one year.
- A trade-off between the SAW device's K^2 and intermediate layer thickness resulted in the selection of a $1\text{ }\mu m$ thick silicon nitride intermediate layer. It was found that the response magnitudes of the SAW based sensor's without an intermediate layer were less than half those of layered SAW based sensors. Furthermore at higher than $200^\circ C$ temperature, in the absence of an intermediate layer the device was not operational (Table 7.3).
- The stoichiometry of the intermediate layer influences the response magnitudes of the sensors' (Table 7.2 and 7.4) as well the gas sensitive layer's carrier

concentration (or conductivity). All three sensors presented different gas sensing performance, e.g. response magnitudes (Table 7.2) of the sensor with the $\text{InO}_x/\text{SiN}_x\text{O}_y/36^\circ\text{YXLiTaO}_3$ structure for H_2 decreased with increase of the working temperature.

Conductometric Sensor

- The SnO_2 nanorods deposited on 36°YXLiTaO_3 substrate have needle-like shapes. The length of one typical nanorod, determined by HRTEM, was approximately 200 nm, with diameters of 10-20 nm at the tip and 20-40 nm at the base. They presented a growth direction of $[10\bar{1}]$, which is different from the growth direction of $[110]$ reported previously for nanorods deposited on a silicon substrate [138].
- Reversible, repeatable and stable responses were recorded in the temperature range of 200 – 300°C for CO for the concentrations between 125 and 500 ppm and for NO_2 between 1.06 and 4.25 ppm. The responses increased with the operational temperature until 280°C, where the highest response was recorded.

In summary this PhD work resulted in a number of novel and significant contributions to the field of layered SAW based gas sensors.

To the author's best knowledge this is the first time that layered SAW sensors with the following structures: $\text{InO}_x/\text{SiO}_2/\text{SiN}_x/36^\circ\text{YXLiTaO}_3$, $\text{InO}_x/\text{SiN}_x\text{O}_y/36^\circ\text{YXLiTaO}_3$ and $\text{InO}_x/\text{SiN}_x/36^\circ\text{YXLiTaO}_3$ have been proposed and presented for H_2 and O_3 sensing applications.

Research papers resulting from this PhD program have been published in refereed journals and presented at various international conferences. These include six first author refereed manuscripts and four international conference proceedings, published in: *Sensors & Actuators: B Chemical*, *IEEE Sensors*, *SPIE*, *Journal of Rare Metal Materials and Engineering* and *Chiang Mai Journal of Science*. A complete list of the author's publications can be found in Chapter 1, Section 1.3. In addition the author was asked for numerous occasions to be a reviewer for the journal of *Sensors & Actuators: B Chemical*.

8.2 Suggestions for Further Work

Throughout the course of this PhD program, several areas of interest with research potential were identified by the author. The continuation of this research can be the application of novel 1-D nanostructured thin films as gas sensitive layers. As was discussed in this thesis, the author has conducted an investigation into the synthesis and deposition of indium oxide nanostructures such as nanowires and nanobelts on silicon substrate using thermal evaporation of nanosized metal oxide powders. Unfortunately this method is not suitable for deposition on LiTaO_3 as it requires elevated temperatures which this substrate cannot withstand. The author believes this work can be extended by investigating different deposition techniques to synthesize a layer of indium oxide nanowires on $\text{SiN}_x/\text{36}^\circ\text{YXLiTaO}_3$. For instance one suitable method, which the author would have liked to investigate but was not possible due to resource restraints, is the use of the Aqueous Chemical Growth (ACG) method, which can be conducted below 100°C . Results from the literature suggest that this method has been successfully employed for the deposition of a ZnO nanorod thin layer on LiNbO_3 SAW transducers for H_2 sensing [69].

Furthermore another extension to the author's work can be the investigation of the application of a catalyst activated (e.g. Au) indium oxide thin film as a gas sensitive layer which will increase the response magnitude of the layered SAW based sensor. In addition the investigation of SnO₂ nanorods layer for gas sensing applications should be continued with the optimisation of the nanorods dimensions and the layer's thickness. An optimised SnO₂ nanorod thin film could be also a very suitable gas sensing layer for a layered SAW based sensors. Another interesting proposition would be the investigation the applications of other materials, such as graphene, as gas sensitive layers for a SAW based device.

Another area of interest for investigation can be the use of SAW resonators for gas sensing applications. In addition other piezoelectric substrates could be utilised (e.g. langasite), which can withstand the high temperature up to 1450°C required for synthesis of indium oxide nanowires by thermal evaporation.

Several suggestions and recommendation have been made. The novel layered SAW based sensors presented in this thesis have shown promising gas sensing performance. The author strongly believes if these structures were further optimised their performance could lead them to be commercialised as O₃ sensors and they could be included in a portable ozone monitor

Appendix A

SH-SAW Substrate Material Data

Table A. 1 Properties of piezoelectric Leaky SAWs. The propagation direction is along the X-direction [45].

Material	Cut	Phase velocity (m/s)	K^2	Attenuation (db/λ)	TCD (ppm/$^{\circ}$C)
LiNbO ₃	41° Y	4792.2f 4379.7m	0.172	0 0.0438	78 80
LiNbO ₃	64° Y	4742.3f 4474.8m	0.113	~0 ~0	79 81
LiTaO ₃	36° Y	4212f 4112m	0.047	~0 ~0	45 32
Quartz	15.7° LST	3848f	0.0011	0.0003	0

f- free surface, m- metallised surface

Appendix B

SH-SAW Propagation Characteristics

The propagation of acoustic waves in an anisotropic piezoelectric crystal can be described by six linear equations in tensor notation [45]:

1. Equation of motions:

$$\frac{\partial T_{ij}}{\partial x_i} = \rho \frac{\partial^2 u_j}{\partial t^2} \quad (\text{B.1})$$

2. From Maxwell's equations for quasi-static approximation:

$$\frac{\partial D_i}{\partial x_i} = 0 \quad (\text{B.2})$$

3. Electric field intensity:

$$E_i = -\frac{\partial \phi}{\partial x_i} \quad (\text{B.3})$$

4. Piezoelectric mechanical stress:
$$T_{ij} = c_{ijkl} S_{kl} - e_{nj} E_n \quad (\text{B.4})$$

5. Piezoelectric displacement density:
$$D_m = c_{ijkl} S_{kl} + \epsilon_{mn} E_n \quad (\text{B.5})$$

6. Linear strain displacement;
$$S_{kl} = \frac{1}{2} \frac{\partial u_k}{\partial x_l} + \frac{1}{2} \frac{\partial u_l}{\partial x_k} \quad (\text{B.6})$$

Where S is strain, T is stress, ρ is mass density, u is mechanical displacement, D is displacement density, E is electric field and ϕ is electric potential. Solutions for equations (B1) and (B6) are related to the electric potential ϕ (in volts) and mechanical displacement u (in meters) assumed to be a complex wave type [45].

Equations (B.4) and (B.5) from above are the piezoelectric constitutive relations, which are the end result of the combination of the material equations with the stress and electrical field equations written in tensor notation. A discussion on the interactions in a non-piezoelectric (elastic constitutive relations) and piezoelectric material (piezoelectric constitutive relations) is included in the following subsections.

B.1 Stress and Strain in Non-piezoelectric Elastic Solid

In a solid medium, mechanical forces are described by the stress field components T_{ij} (stress tensor) and mechanical deformations by the strain field components S_{ij} (strain tensor), which are classed as second-order tensors.

Appendix B

For small static deformations of a non-piezoelectric elastic solid, Hooke's Law for elastic deformation can be applied. This law states that strain is linearly proportional to stress and can be mathematically written in tensor notation as:

$$T_{ij} = \sum_{kl} c_{ijkl} S_{kl} \quad (\text{B.7})$$

where c_{ijkl} are fourth-order tensors, called the *elastic stiffness constants* (in units of $[\text{N/m}^2]$).

Equation (B.7) , with all possible combinations of the subscript ij , gives 81 elastic constants.

However the tensor equation B7 can be reduced to the matrix equation of:

$$[T] = [c][S], \quad (\text{B.8})$$

and when the stress components are symmetric:

$$T_{ij} = T_{ji}$$
$$c_{ijkl} = c_{jikl} = c_{ijlk} = c_{jilk} .$$

This reduces the stiffness constants to a 6×6 matrix $[c]$ with the number of independent values of 36 relating the six reduced components of stress to the six reduced components of strain. These constants can be further reduced to 21 from energy and symmetry considerations, which is the maximum for any medium. Moreover further reduction is possible by choosing an appropriate choice of reference coordinate in relation to the crystal axes. For example the number of elastic coefficients reduces to five when the z -reference coordinate is chosen along the z -axis of a hexagonal crystal (e.g. for ZnO).

Then again the strain can be also expressed as general linear functions for all stresses:

$$S_{ij} = \sum_{kl} c_{ijkl} T_{kl} \quad (\text{B.9})$$

In this case s_{ijkl} are called *compliance constants* (in units of $[\text{m}^2/\text{N}]$). These quantify the deformability of a medium and have large values for easily deformed materials and small values for rigid materials. Equation (B.7) and B.9) are the *elastic constitutive relations*.

B.2 Piezoelectric Interactions

For piezoelectric materials, equation (B.7) is no longer valid. In this case the coupling between electrical and mechanical parameters, by applying an electric field, will give rise to mechanical deformations. This interaction can be written mathematically in terms of the piezoelectric constant matrix $[e]$ (C/m^2). The electric displacement density D , and mechanical stress T for piezoelectric materials can be written in matrix notation as:

$$D = [\varepsilon]E + [e][S] \quad (\text{B.10})$$

$$T = [c][S] - [e'] [E], \quad (\text{B.11})$$

where E is the *electric field* and ε is the *dielectric permittivity* measured at zero or constant strain. These equations represent the *piezoelectric constitutive relations*, which are the end result of the combination of the material equations with the stress and electrical field equations.

B.3 SH-SAW (LSAW) Propagation

To investigate the SH-SAW (LSAW) propagation we consider a rotated Y-cut of lithium tantalate substrate shown in Figure D1, where (X, Y, Z) are the crystallographic coordinates and (x1, x2, x3) are coordinates rotated by θ about the X-axis.

The displacement components, u_i (i=1, 2, 3), and the electric potential ϕ for the leaky wave propagating along the X (x1) axis can be written as follows [104]:

$$u_i = \sum_{n=1}^4 A_n \alpha_{in} e^{jk[\beta_n x_2 + (1+\delta)x_1 - vt]} \quad (\text{B.12})$$

$$\phi = \sum_{n=1}^4 A_n \alpha_{4n} e^{jk[\beta_n x_2 + (1+\delta)x_1 - vt]} \quad (\text{B.13})$$

where v is the propagation velocity, k is the wavenumber, β is the phase constant (rad/m) and δk is the decay constant along the propagation direction,

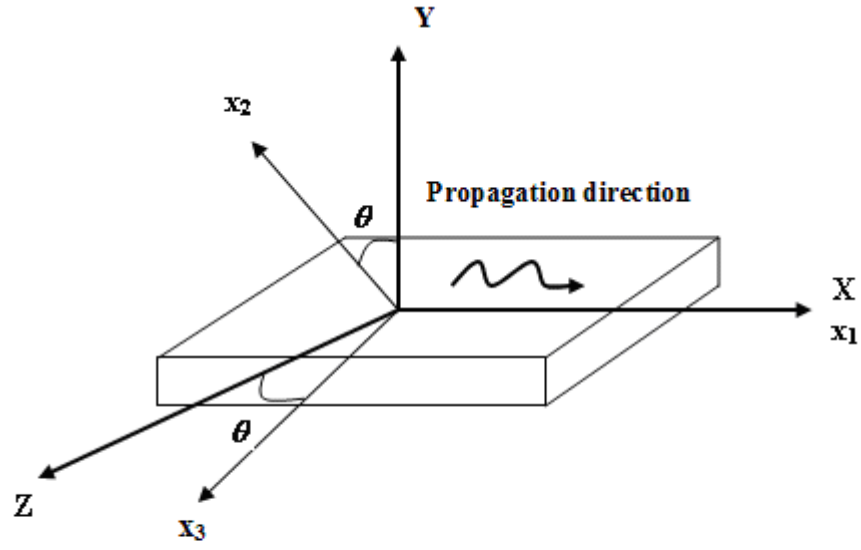


Figure B.1 SH-SAW propagating along the X-axis and rotated by about θ the Y-axis

The boundary condition which needs to be satisfied for the elastic quantities is [176]:

$$T_{2j} \Big|_{x_2=0} = 0 \quad (\text{B.14})$$

And the boundary conditions for the electric quantities are:

$$\phi \Big|_{x_2=0} = 0 \quad \text{for metallised surface} \quad (\text{B.15})$$

$$D_2 \Big|_{x_2=0} = -\epsilon_0 \frac{\partial \phi^e}{\partial X_2} \Big|_{x_2=0} \quad \text{for free surface} \quad (\text{B.16})$$

Considering these boundary conditions and substituting equations (B.12) and (B.13) into the equations of motions (B.1), Maxwell's equation (B.2) as well as in the piezoelectric constitutive (B.3 and B4) equations will result in a set of linear equations in the form:

$$[H] \cdot \begin{bmatrix} A_1 \\ A_2 \\ A_3 \\ A_4 \end{bmatrix} = 0 \quad (B.17)$$

where $[H]$ is a 4×4 matrix. The exact solution for a SH-SAW (such as a leaky SAW) can be obtained by finding the propagating wave velocity v as well the decay constant δk , which satisfy the equation $|H| = 0$. In the case when $\delta = 0$ a perfect surface wave is generated.

B.4 SH-SAW (LSAW) Generation

Figure 1 shows a single delay SAW device (top and side view) used to generate SH-SAW (e.g. a LSAW) with the IDTs formed by a uniform single thin film metal electrodes with equal width and spacing, where W is the aperture (or constant finger overlap) and L is the center-to-center spacing (or time delay) between the two IDTs. The latter one defines the distance travelled by the acoustic wave and it is an important parameter in the design of the SH-SAW based sensor.

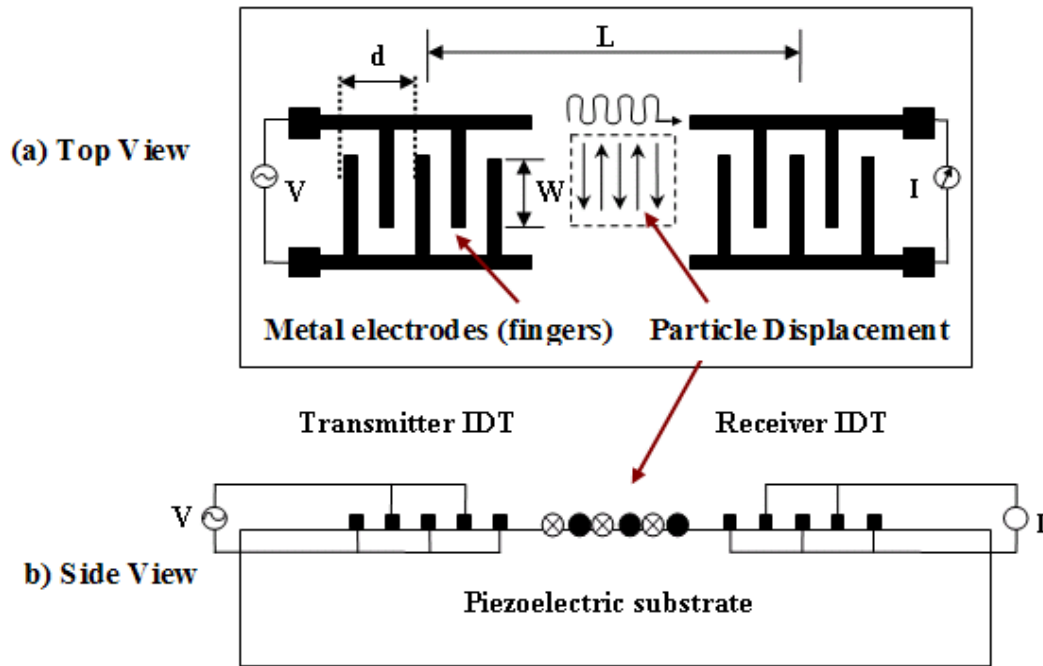


Figure B.2 Delay line SH-SAW device composed of an input and output IDT formed by metal electrodes patterned on a piezoelectric crystal: (a) Top view and (b) Side view, (redrawn and modified from [104]).

Application of an alternating voltage to the input IDT will induce a periodic electric field as the electrodes will become alternately negatively and positively polarised. The electric field distribution induces strains in the piezoelectric substrate generating a standing SAW. This wave will propagate away from the input IDT in both directions at the velocity of the particular acoustic wave generated (e.g. for SH-SAW $v_m = 4112$ m/s on LiTaO_3 substrate). The mechanical wave energy at the output IDT is transformed back into an electrical energy. The transducer operates most efficiently (converting electrical energy to acoustic energy) when the SAW wavelength λ_0 matches the IDT periodicity, d [104].

This occurs when the device is excited at the synchronous (centre) frequency defined by:

$$f_0 = \frac{v_0}{d} \quad (\text{B.18})$$

The propagation of a mechanical wave in a piezoelectric medium is related to the electric potential (ϕ) and this induces a current flow in each electrode when the wave is incident on a receiving output transducer as shown in Figure B.2 b. These currents combine to produce a current flow in the external circuit. The additions of current contributions are optimised in the receiving IDT when the transducer periodicity (d) matches the SAW's λ_0 .

Equation (B.18) shows that the frequency response is related to the geometry of the IDT structure. To investigate the IDT transducer frequency response each transducer finger will be considered to be a discrete source (discrete source model) for the generation of surface waves in a piezoelectric medium.

In this case a transfer function can be written as [104]:

$$\phi^{\pm} = \mu_s V_1, \quad (\text{B.19})$$

where μ_s is a substrate dependent constant but is frequency independent, V_1 is the continuous wave voltage applied to a finger and ϕ^+ is the rightward propagating SAW, while ϕ^- is the leftward propagating SAW.

When the fingers are excited the ϕ^+ at position z can be written as a vector sum of each finger contributions [104]:

$$\phi^+ = \mu_s \sum_{n=0}^{N_f-1} V_n e^{jk(z-z_n)} \quad , \quad (\text{B.20})$$

where z_n is the position of n^{th} finger excited with voltage V_n and N_f is the total number of fingers. This equation has the form of a *discrete Fourier transform* of sequence V_n , so the frequency response of the delay line device is the Fourier transform of the transducer finger contributions.

For N_f fingers with period d excited with alternating voltages $V_n = (-1)^n V_0$, equation (B.20) will become:

$$\phi^+(0) = \mu_s V_0 \sum_{n=0}^{N_f-1} (-1)^n e^{-jkn d / 2} \quad (\text{B.21})$$

The frequency response of the delay line device can be find out from this equation by addition of components form individual fingers form each IDTs. At frequencies close to the synchronous (centre) frequency the delay line response can be approximated by a sinc(X) function (Figure 3.4) as [178]:

$$\left| \phi^+(f)_{\text{delay-line}} \right| = \sin c \left| \frac{N_p \pi (f - f_0)}{f_0} \right| \quad (\text{B.22})$$

Where $\text{sinc}(X) = \sin(X)/X$ and $N_p = N_f / 2$ is the number of IDTs period.

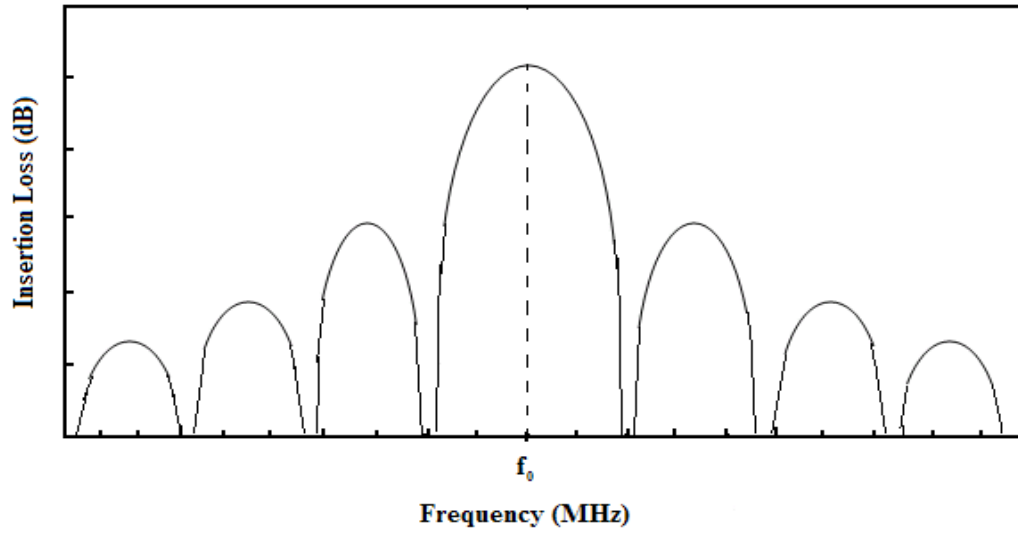


Figure B.3 Frequency response of a SAW delay line can be approximated to a $\text{sinc}(X)$ function [177].

Appendix C

Material Constants

Table C.1 Material constants

Material	Symmetry class	Elastic constants (10^{10} N/m ²)		Density (kg/m ³)	Permittivity* (ϵ^{11}/ϵ_0)	Reference
		c_{11}	c_{44}			
Si ₃ N ₄	isotropic	38.53	12.26	3184	7.5	[117]
PECVD Si ₃ N ₄	isotropic	14.74	5.16	2500	7.5	[118]
In ₂ O ₃	cubic	26.99 23.43	7.05 6.27	7190	9.0	[174]
LiTaO ₃	3m	23.80	9.49	7454	40.9 42.5	[175]

* Permittivity was normalised to the permittivity of free space $\epsilon_0 = 8.854 \cdot 10^{-12}$ F/M

Appendix D

SAW Testing System

A custom built SAW testing system was developed in the Sensor Technology Laboratory at RMIT University. This includes a Teflon gas chamber and an RF amplifier assembly shown in figure 5.2 on page 93 (Chapter 5 of the thesis). These were placed in a thermally shielded steel box to keep away from electromagnetic interference (EMI). During testing for stability, an environmental chamber was used in order to hold the ambient temperature at 22° C.

RF Amplifier Assembly

The high gain RF amplifier was designed and simulated by using Agilent Advanced Design Systems (ADS) computer software. The amplifier consists of three stages as shown in figure D.1 (from reference [29]).

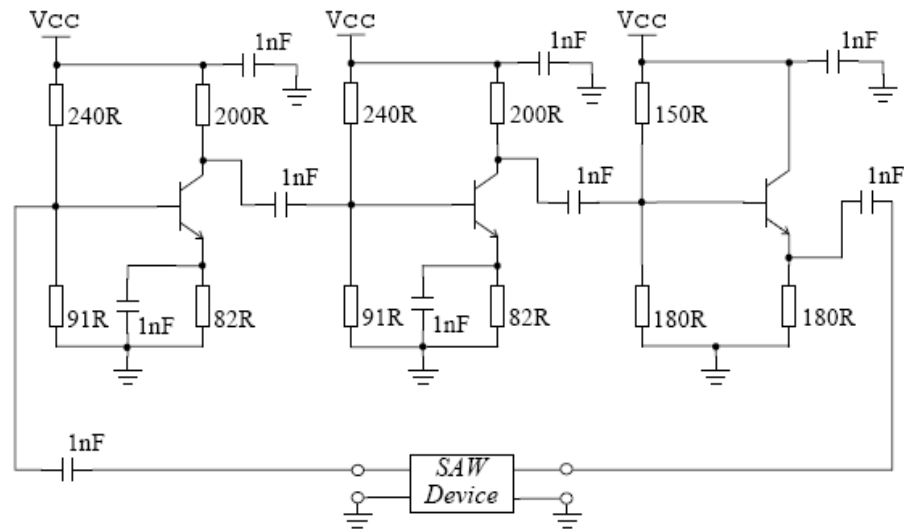
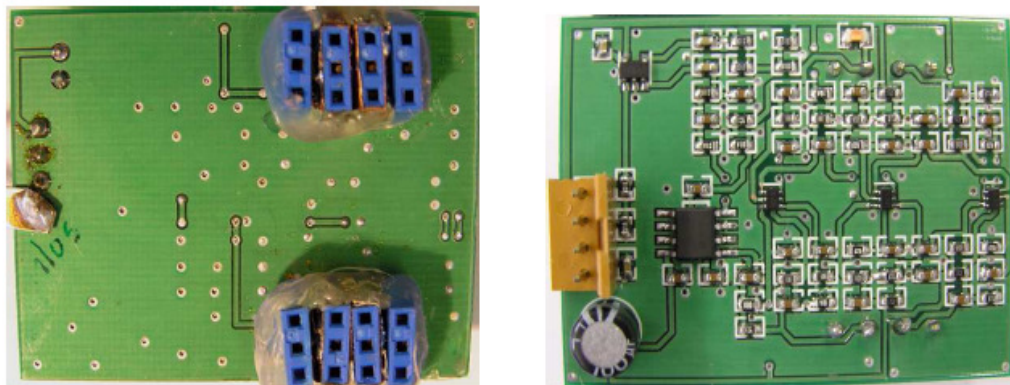


Figure D.1 Three stage R.F. amplifier schematic (from [29]).

The first two stages provide the forward power gain (between 25 and 30 dB) and the last stage is used to increase the overall stability factor calculated by the Agilent ADS software. Low noise, high gain bipolar NPN transistors (Infineon BFS841) is used for each stage. The BFS841 package contains two balanced pair transistors of which one IC package is used for each stage. A common emitter arrangement is used to bias the two power gain stages and a common collector (emitter follower) for the unity gain stage. The remaining transistor in each IC packages is used to form an identical amplifier circuit to allow differential measurements.



(a) Front

(b) Back

Figure D.2 R.F. amplifier printed circuit board (from [29])

Appendix D

The amplifier PCB (back and front sides) is shown in figure D.2 (a) and (b). The blue connectors on the front side of the PCB (figure D.2 (a)) provide the electrical connection between the SAW sensor and amplifier circuit. The three small ICs (Infineon packages) shown on the right hand side of figure D.2 (b) are the voltage regulator and differential frequency mixer.

The measured and simulated transmission responses (or S_{21} parameter) of the amplifier were in good agreement between 100 and 200 MHz range. A carrier PCB provided the electrical connection between the network analyser (Rohde & Schwarz, ZVRE) and the amplifier PCB.

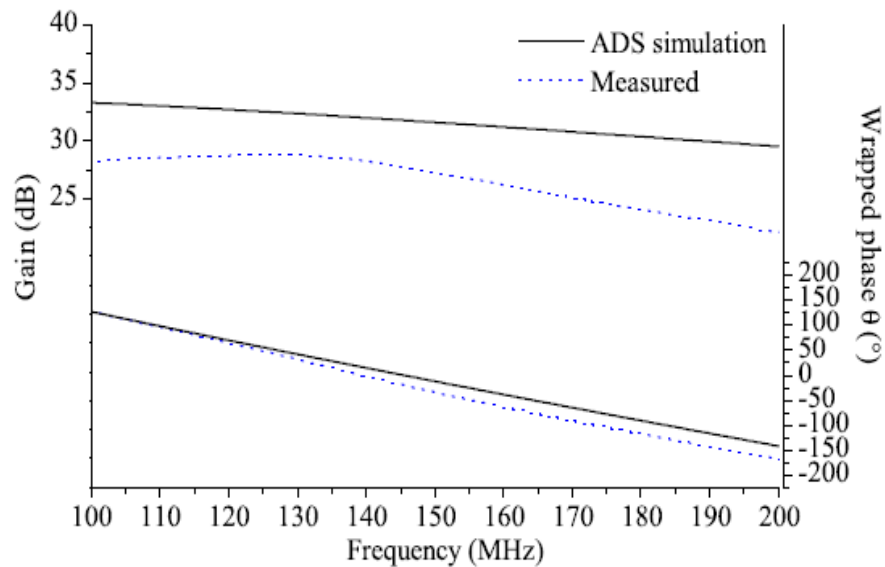


Figure D.3 Comparison of the simulated and measured S_{21} parameter of the amplifier (from [29]).

Appendix E

Static Performance Characteristics

The static performance characteristics used in this thesis can be described as follows:

Stability – refers to the change in baseline frequency of the SAW sensors over a given period of time. In this thesis this was measured over a one hour period of time.

Reversibility - sensor response is considered to be reversible if its response returns (or recovers) to the original baseline frequency after a given recovery time.

Repeatability - sensor response is repeatable if the sensor has the same response and recovery time when to the same concentration of target gas analyte was exposed.

Response and recovery time- defined as the time taken by the sensor to reach 90% of the saturation level after applying or switching off the respective target gas analyte.

Bibliography

- [1] University of Michigan, “Pollution and society” [WWW document] URL, <http://www.umich.edu/~gs265/society/pollution>.

- [2] Australian Government website page, “State of the environment - issue: air quality - pressures and responses”, [WWW document], URL, <http://www.environment.gov.au/soe/2006/publications/drs/atmosphere/issue/18/index.html>.

- [3] National Environmental Technology Centre (UK), “The chemistry of atmospheric pollutants” [WWW document], URL, <http://www.aeat.co.uk/netcen/airqual/kinetics>.

- [4] The World Health Organisation, “Estimated deaths & Daly’s attributable to selected environmental risk factors, WHO Member State, 2002” , Department of Public Health & Environment, January 2007, URL, [WWW document], http://www.who.int/quantifying_ehimpacts/countryprofilesebd.xls.

Bibliography

- [5] P. T. Moseley and B. C. Tofield, "Solid state gas sensors", Adam Hilger Publishing, Bristol, UK, 1987.
- [6] G. Muller and G. Krotz, "SiC for sensors and high-temperature electronics", *Sensors and Actuators*, vol. 56, pp. 259-268, 1994.
- [7] P. Kofstad, "Nonstoichiometry diffusion and electrical conductivity in binary metal oxides", Wiley, New York NY, USA, 1983.
- [8] T. Seiyama, A. Kato, K. Fujishi and M. Nagatani, "A new detector for gaseous components using semiconductor thin films", *Analytical Chemistry*, vol. 34, pp. 1502-1507, 1962.
- [9] T. Takada, K. Suzuki and M. Nakane, "Highly sensitive sensor", *Sensors and Actuators*, vol.13, pp. 404-407, 1993.
- [10] M. J. Vellekoop, "Acoustic wave sensors and their technology", *Ultrasonics*, vol.36, pp. 7-14, 1998.
- [11] A. J. Ricco, S. J. Martin, and T. E. Zipperian, "Surface acoustic wave gas sensor based on film conductivity changes", *Sensors and Actuators*, vol. 8, pp. 319-333, 1985.
- [12] EnviroTool website, "A guide to toxic air pollutants", [WWW document], URL, <http://www.envirotools.org/factsheets/contaminants/ozone>.

Bibliography

- [13] World Health Organisation - Europe, “Health aspect of air pollution – answers to follow up questions for CAFÉ”, [WWW document], URL, <http://www.euro.who.int/document/E82790.pdf>.
- [14] J. Billingsley, “Studies confirm ozone’s health risks”, [WWW document], URL, http://news.yahoo.com/s/hsn/20050617/hl_hsn.
- [15] U.S National Ambient Air Quality Standard, [WWW document], URL, <http://www.epa.gov/air/criteria.html>.
- [16] Assembly Bill No. 2276 for the state of California (USA), [WWW document], URL, http://www.arb.ca.gov/research/indoor/aircleaners/_ab2276-bill.pdf.
- [17] World Health Organisation webpage, [WWW document], URL <http://www.who.int/mediacentre/factsheets/fs313/en>
- [18] D. Sauter, U. Weimar, G. Noetzel, J. Mitrovics and W. Gopel, “Development of modular ozone sensor system for application in practical use”, Sensors and Actuators, vol.64, pp.1-9, 2000.
- [19] B. Stark, G. Sonnemann, L. Martini, B. Fichtelmann, “Method for highly sensitive detection of ozone using UV ionization and measuring ionization current”, Technical Report DD 294097 A5910919, 1988.

- [20] D. E. Heard, "Analytical techniques for atmospheric measurement", Atmospheric Analysis Handbook from C.H.I.P.S., 2006.
- [21] H. Dwayne, "Analytical techniques for atmospheric measurement", Lavoisier Library, France, 2006.
- [22] D. C. Thorton and N. Niazy, "Sources of background current in the ECC ozone sonde implications for total ozone measurement" J. Geophys. Res., vol 87, pp. 8943-8950, 1982.
- [23] L. C. Feldman and J. W. Mayer, "Fundamentals of surface and thin film Analysis", Prentice-Hall, Englewood Cliffs, NJ, 1986.
- [24] Health Organisation – Europe, "Health aspects of air pollution with particulate matter, ozone and nitrogen dioxide", [WWW document], URL, <http://www.euro.who.int/document/e79097.pdf>.
- [25] S. T. Omaye, "Metabolic modulation of carbon monoxide toxicity", Toxicology, vol. 180, pp. 139-150, 2002.
- [26] C. Christofides and A. Mandelis, "Solid-state sensors for trace hydrogen gas detection", Journal of Applied Physics, vol. 68, pp. R1-R30, 1990.
- [27] H. Wohltjen, "Surface acoustic wave microsensors", Transducers '87, pp. 471-477, 1987.

- [28] E. Comini, “Metal oxide nano-crystals for gas sensing”, *Analytica Chimica Acta*, vol. 568, pp. 28-40, 2006.
- [29] S. J. Ippolito, “Investigation of multilayered surface acoustic wave devices for gas sensing applications”, PhD Thesis, RMIT University, Australia, 2006.
- [30] D. A. Powell, K. Kalantar-Zadeh, W. Wlodarski, and S. J. Ippolito, “Layered surface acoustic wave chemical and bio-sensors”, in *Encyclopaedia of Sensors*, C. A. Grimes, E. C. Dickey, and M. V. Pishko, Eds., vol. 5, pp. 245-262. American Scientific Publishers, 25650 North Lewis Way, Stevenson Ranch, California 91381-1439, USA, 2006.
- [31] G. Kiriakidis, H. Ouacha and N. Katsarakis, “InO_x nanostructured thin films: electrical and sensing characterization”, *Rev. Adv. Mater. Sci.*, vol. 4, pp. 32-40, 2003.
- [32] T. S. Hickernell, F. M. Fliegel, F. S. Hickernell, “The elastic properties of thin-film silicon nitride”, *Proceedings of Ultrasonic Symposium*, pp. 445-448, 1990.
- [33] C. Baratto, E. Comini, G. Faglia, G. Sberveglieri, M. Zha and A. Zappettini “Metal oxide nanocrystals for gas sensing”, *Sensors and Actuators*, vol. 109, pp. 2-6, 2005.
- [34] B. Drafts, “Acoustic wave technology sensors”, *IEEE Transactions on Microwave Theory and Techniques*, vol.49, pp. 795-802, 2001.

Bibliography

- [35] D. P. Morgan, "History of SAW devices", IEEE International Frequency Control Symposium, pp. 439-460, 1998.
- [36] D. P. Morgan, "Surface-wave devices for signal processing", Studies in Electrical and Electronic Engineering, vol. 19, Elsevier Science Publishers, New York, 1985.
- [37] R. M. White and F. W. Voltmer, "Direct piezoelectric coupling to surface elastic waves", Applied Physics Letters., vol. 7, pp. 314-316, 1965.
- [38] H. Wohltjen and R. Dessy, "Surface acoustic wave probe for chemical analysis. Part II: Gas chromatography detector", Analytical Chemistry, vol. 51, pp. 1465-1470, 1979.
- [39] A. D'Amico, A. Palma, and E. Verona, "Hydrogen sensor using a palladium coated surface acoustic wave delay-line", Proceedings of the IEEE Ultrasonics Symposium, pp. 308-311, 1982.
- [40] M. Penza and L. Vasanelli, "SAW NO_x gas sensor using WO₃ thin-film sensitive coating", Sensors and Actuators, vol. 41, pp. 31-36, 1997.
- [41] J. D. Galipeau, R. S. Falconer, J. F. Vetelino, J. J. Caron, E. L. Wittman, M. G. Schweyer, and J. C. Andle, "Theory, design and operation of a surface acoustic wave hydrogen sulfide microsensor", Sensors and Actuators, vol. 24-25, pp. 49-53, 1995.

Bibliography

- [42] J. W. Grate, S. J. Martin, and R. M. White, "Acoustic wave microsensors", *Analytical Chemistry*, vol. 65, pp. 940A-948A, 1993.
- [43] K. Hashimoto, "Surface acoustic wave devices in telecommunications: modelling and simulation", Springer, 2000.
- [44] K. Nakamura, M. Kazumi and H. Shimizu, "SH-type surface wave rotated Y-cut LiTaO₃", *IEEE Ultrasonics Symposium Proceedings*, pp. 819-822, 1977.
- [45] Colin K. Campbell, "Surface acoustic wave devices for mobile and wireless communications", Academic Press, San Diego, 1998.
- [46] A. Takayanagi, K. Yamanouchi and K. Shibayama, "Piezoelectric leaky surface wave in LiNbO₃", *Applied. Physics Letters*. vol. 17, pp. 225-230, 1970.
- [47] H. Meier, P. Russer, "Analysis of leaky surface wave in LiTaO₃ substrate", *IEEE Frequency Control Symposium*, pp.378-383, 1992.
- [48] T. Moriizumi., Y. Unno and S. Shiokawa, "New sensor in liquid using leaky SAW", *Proceedings of the IEEE Ultrasonics Symposium*, pp. 579-582, 1987.
- [49] R. L. Baer and C.A Flory, "Some limitations on the use of leaky SAW mode sensors in liquids", *Proceedings of the IEEE Ultrasonics Symposium*, pp. 279-2842, 1991.

Bibliography

- [50] A. P. Campitelli, W. Wlodarski and M. Hoummady, “Identification of natural spring water using shear horizontal SAW based sensors”, *Sensors and Actuators*, vol. 49, pp. 195-201, 1998.
- [51] S. J. Ippolito, A. Ponzoni, K. Kalantar-zadeh, W. Wlodarski, E. Comini, G. Faglia, and G. Sberveglieri, “Layered $\text{WO}_3/\text{ZnO}/36^\circ \text{LiTaO}_3$ SAW gas sensor sensitive towards ethanol vapour and humidity”, *Sensors and Actuators*, vol. 117, pp. 442-450, 2006.
- [52] A. E. H. Love, “A treatise on the mathematical theory of elasticity”, Cambridge: Dover, 1967.
- [53] G. Kovacs, M. J. Vellekoop, R. Haueis, G. W. Lubking, and A. Venema, “A Love wave sensor for (bio)chemical sensing in liquids”, *Sensors and Actuators A: Physical*, vol. 43, pp. 38-43, 1994.
- [54] E. Gizeli, N. J. Goddard, C. R. Lowe, and A. C. Stevenson, “A Love plate biosensor utilising a polymer layer”, *Sensors and Actuators B: Chemical*, vol. 6, pp. 131–137, 1992.
- [55] B. Jakoby, G. M. Ismail, M. P. Byfield, and M. J. Vellekoop, “A novel molecularly imprinted thin film applied to a Love wave gas sensor”, *Sensors and Actuators A: Physical*, vol. 76, pp. 93-97, 1999.

- [56] C. Zimmermann, D. Reiere, C. Dejous, J. Pistre, E. Chastaing, and R. Planade, “A love wave gas sensor coated with functionalized polysiloxane for sensing organophosphorus compounds”, *Sensors and Actuators B: Chemical*, vol. 76, pp.86-94, 2001.
- [57] G. Kovacs, G. W. Lubking, M. J. Vellekoop, and A. Venema, “Love waves for (bio)chemical sensing in liquids”, *Proceedings of the of the IEEE Ultrasonics Symposium*, pp. 281–285,1992.
- [58] K. Kalantar-Zadeh, “Investigation of a love mode acoustic wave transducer for bio-sensing applications”, Ph.D. thesis, RMIT University, 2001.
- [59] J. Du, G. L. Harding, J. A. Ogilvy, P. R. Dencher, and M. Lake, “A study of Love wave acoustic sensors”, *Sensors and Actuators A: Physical.*, vol. 56, pp. 211–219, 1996.
- [60] M. S. Nieuwenhuizen and A. J. Nederlof, “A silicon-based SAW chemical sensor for NO₂ by applying a silicon nitride passivation layer”, *Sensors and Actuators B: Chemical*, vol. 9, pp. 171-176, 1992.
- [61] W. P. Jakubik, M. W. Urbanczyk, S. Kochowski, and J. Bodzenta, “Bilayer structure for hydrogen detection in a surface acoustic wave sensor system”, *Sensors and Actuators B: Chemical*, vol. 82, pp. 265-271, 2002.

- [62] W. P. Jakubik, M. W. Urbanczyk, S. Kochowski, and J. Bodzenta, "Palladium and phthalocyanine bilayer films for hydrogen detection in a surface acoustic wave sensor system", *Sensors and Actuators B: Chemical*, vol. 96, pp. 321-328, 2003.
- [63] S. J. Ippolito, S. Kandasamy, K. Kalantar-zadeh, W. Wlodarski, K. Galatsis, G. Kiriakidis, N. Katsarakis, and M. Suche, "Highly sensitive layered ZnO/LiNbO₃ SAW device with InO_x selective layer for NO₂ and H₂ gas sensing", *Sensors and Actuators B: Chemical*, vol. 111-112, pp. 207-212, 2005.
- [64] A. D'Amico and E. Verona, "SAW sensors", *Sensors and Actuators*, vol. 17, pp. 55-66, 1989.
- [65] D. S. Ballantine and H. Wohltjen, "Surface acoustic wave devices for chemical analysis", *Analytical Chemistry*, vol. 61, pp. 704A-715A, 1989.
- [66] J. D. N. Cheeke and Z. Wang, "Acoustic wave gas sensors", *Sensors and Actuators B: Chemical*, vol. 59, pp. 146-153, 1999.
- [67] B. Drafts, "Acoustic Wave Technology Sensors", *IEEE Transactions on Microwave Theory and Techniques*, vol.49, pp. 795-802, 2001.
- [68] V. I. Anisimkin, Yu. V. Gulyaev, "Surface acoustic waves method: New analytical capabilities", *Surface Investigation*, vol. 16, pp. 1213-1224, 2001.

- [69] A. Z. Sadek, W. Wlodarski, Y. X. Li , W. Yu, X. Li, X. Yu, K. Kalantar-zadeh, "A ZnO nanorod based layered ZnO/64°YXLiNbO₃ SAW hydrogen gas sensor", *Thin Solid Films*, vol. 515 pp. 8705–8708, 2007.
- [70] M. Penza, F. Antolini, and M. Vittori-Antisari, "Carbon nanotubes as SAW chemical sensors materials", *Sensors and Actuators B: Chemical*, vol. 100, pp. 47-59, 2004.
- [71] T. Alizadeh and S. Zeynali, "Electronic nose based on the polymer coated SAW sensors array for the warfare agent simulants classification", *Sensors and Actuators B: Chemical*, vol 129, pp. 412-423, 2008
- [72] M.J. Fernández, J, L. Fontecha, I. Sayago, M. Aleixandre, J. Lozano, J. Gutiérrez, I. Gràcia, C. Cané and M. Horrillo, "Discrimination of volatile compounds through an electronic nose based on ZnO SAW sensors", *Sensors and Actuators B: Chemical*, vol. 127, pp. 277-283, 2007.
- [73] A. Chiba, "Development of the TGS Gas Sensor", in *Chemical Sensor Technology* Vol. 4, S. Yamauchi (Ed.), Elsevier, Amsterdam, The Netherlands 1992.
- [74] K. Takahata, "Tin dioxide sensors – development and applications", *Chemical Sensor Technology*, T. Seiyama, Ed. vol 1, Elsevier, 1988.
- [75] Y. Nakamura, "Stability of the sensitivity of SnO₂-based elements in the field" *Chemical Sensor Technology*, T. Seiyama, Ed. vol 2, Elsevier, 1989.

- [76] A. Chiorina, F. Boccuzzi and G. Ghiotti, “Surface chemistry and electronic effects of O₂, NO and NO/O₂ on SnO₂”, *Sensors and Actuators B: Chemical*, vol. 1, pp. 177-175, 1990.
- [77] New Cosmos Electrical Ltd. Co., New Cosmos home page”, [WWW document] URL, <http://www.new-cosmos.co.jp/en/index>.
- [78] Figaro Engineering Inc., Figaro home page, [WWW document] URL, <http://www.figaro.co.jp>.
- [79] C. Xu, J. Tamaki, N. Miura and N. Yamazoe , “Grain size effects on gas sensitivity of porous SnO₂-based elements” , *Sensors and Actuators B: Chemical*, vol. 3, pp. 147-155, 1991.
- [80] Y. Xia , P. Yang, Y. Sun, Y. Wu , B. Mayers, B. Gates, Y. Yin, F. Kim and H. Yan, “One-dimensional nanostructures: synthesis, characterization, and applications”, *Advanced Materials* , vol. 15, pp. 353 – 389, 2003.
- [81] G. Korotcenkov, V. Brinzari., A. Cerneavski, M. Ivanov, A. Cornet, J. Morante, A. Cabot, and J. Arbiol, “In₂O₃ films deposited by spray pyrolyses: gas response to reducing (CO, H₂) gases”, *Sensors and Actuators B: Chemical*, vol. 98, pp. 122-129 , 2004.

- [82] G. Korotcenkov, A. Cerneavski, V. Brinzari, A. Vasiliev, M. Ivanov, A. Cornet, J. Morante, A. Cabot and J. Arbiol, "In₂O₃ films deposited by spray pyrolysis as a material for ozone gas sensors", *Sensors and Actuators B: Chemical*, vol. 99, pp. 297-303, 2004.
- [83] W. Y. Chung, G. Sakai, K. Shimanoe, N. Miura, D.D. Lee and N. Yamazoe, "Preparation of indium oxide thin film by spin-coating method and its gas-sensing properties", *Sensors and Actuators B: Chemical*, vol. 46, pp. 139-145, 1998.
- [84] A. Gurlo, M. Ivanovskaya, A. Pfau, U. Weimar, W. Göpel, "Sol-gel prepared In₂O₃ thin films", *Thin Solid Films*, vol. 307, pp. 288 - 293, 1997.
- [85] E. Gagaoudakis, M. Bender, E. Douloufakis, N. Katsarakis, E. Natsakou, V. Cimalla and G. Kiriakidis, "The influence of deposition parameters on room temperature ozone sensing properties of InO_x films", *Sensors and Actuators B: Chemical*, vol. 80, pp. 155-161, 2001
- [86] M. Ivanovskaya, A. Gurlo, P. Bogdanov, "Mechanism of O₃ and NO₂ detection and selectivity of In₂O₃ sensors", *Sensors and Actuators B: Chemical*, vol. 77, pp. 264-267, 2001.
- [87] A. Gurlo, M. Ivanovskaya, N. Bârsan, M. Schweizer-Berberich, U. Weimar, W. Göpel and A. Diéguez, "Grain size control in nanocrystalline In₂O₃ semiconductor gas sensors", *Sensors and Actuators B: Chemical*, vol. 44, pp. 327-333, 1997.

- [88] G. Faglia, B. Allieri, E. Comini, L. E. Depero, L. Sangaletti and G. Sberveglieri, “Electrical and structural properties of RGTO-In₂O₃ sensors for ozone detection”, *Sensors and Actuators B: Chemical*, vol. 57, pp.188-191, 1999.
- [89] G. Kiriakidis, N. Katsarakis, M. Bender, E. Gagaoudakis, V. Cimalla, “InO_x thin films, candidates for novel chemical and optoelectronic applications”, *Mater. Phys. Mech.*, vol.1, pp. 83-97, 2000.
- [90] M. Sueha, N. Katsarakis, S. Christoulakis, S. Nikolopoulou and G. Kiriakidis, “Low temperature indium oxide gas sensors”, *Sensors and Actuators B: Chemical*, vol. 118, pp.135-141, 2006.
- [91] C. Li, D. H. Zhang, X. L. Liu, S. Han, T. Tang, J. Han, C. Zhou, “In₂O₃ nanowires as chemical sensors” , *Applied Physics Letters*, vol. 82, pp. 1613-1615, 2003.
- [92] D. Zhang, C. Li, Z. Liu, S. Han, T. Tang, B. Lei, C. Zhou, “Detection of NO₂ down to ppb levels using individual and multiple In₂O₃ nanowire devices”, *Nano Letters.*, vol 4, pp. 1919-1924, 2004.
- [93] E. Comini, S. Bianchi, M. Ferroni, G. Faglia, A. Vomiero and G. Sberveglieri “Indium oxide quasi-monodimensional low temperature gas sensor”, *Sensors and Actuators B: Chemical*, vol. 118, pp. 204-207, 2006.

- [94] M. Epifani, E. Comini, J. Arbiol, R. Díaz, N. Sergent, T. Pagnier, P. Siciliano, G. Faglia and J. R. Morante, “Chemical synthesis of In_2O_3 nanocrystals and their application in highly performing ozone-sensing devices”, *Sensors and Actuators B: Chemical*, vol. 130, pp 483-487, 2008.
- [95] K. Ihokura and J. Watson, “The stannic oxide gas sensor – Principles and application”, CRC Press, Boca Raton, FL, 1994.
- [96] W. Göpel, K. D. Schierbaum, “ SnO_2 sensors: current status and future prospects”, *Sensors and Actuators B: Chemical*, vol. 26-27, pp. 1-12, 1995.
- [97] N. Murakami, S. Yasunage and K. Ihokura, “Sensitivity and sintering temperature of SnO_2 gas sensors”, *Anal. Chem. Symp.*, vol 17, p. 18, 1983.
- [98] M. Law, H. Kind, B. Messer, F. Kim and P. Yang, ”Photochemical sensing of NO_2 with SnO_2 nanoribbon nanosensors at room temperature”, *Angew. Chem. International Ed.* 41, pp. 2405–2407, 2002.
- [99] Y. Zhang, A. Kolmakov, S. Chretien, H. Metiu, M. Moskovitz, “Control of catalytic reactions at the surface of a metal oxide nanowire by manipulating electron density inside it” *Nanoletters*, vol. 4, pp. 403-407, 2004.
- [100] E. Comini, G. Faglia, G. Sberveglieri, D. Calestani, L. Zanotti and M. Zha, “Tin oxide nanobelts electrical and sensing properties”, *Sensors and Actuators B: Chemical*, vol. 111-112, pp. 2-6, 2005.

Bibliography

- [101] J. H. Hines, D.C. Maloucha, K. B. Sundaram, K. J. Casey and K. R. Lee, "Deposition parameter studies and surface acoustic wave characterisation on PECVD silicon nitride on lithium niobate", IEEE Transaction on Ultrasonics, Ferroelectric and Frequency Control, vol. 42, no. 3, 1995.
- [102] P.A. Banda Rueda, "Investigation on surface acoustic wave was sensors. Application to ozone sensors", Ph.D. Thesis, RMIT University, 1995.
- [103] A. J. Ricco and S. J. Martin, "Thin metal film characterization and chemical sensors: monitoring electronic conductivity, mass loading and mechanical properties with surface acoustic wave devices", Thin Solid Films, vol. 206, pp. 94-101, 1991.
- [104] D. S Ballantine, R. M. White, S. J. Martin, A. J. Ricco, E. T. Zellers, G. C. Frye and M. Wohltjen, "Acoustic Wave Sensors : Theory , Design , and Physico-Chemical Applications", Academic Press ,San Diego ,1997
- [105] B. A. Auld, "Acoustic fields and waves in solids", vols. 1 and 2, Wiley Inter- science, New York, 1973.
- [106] M. Thompson and D. C. Stone; edited by J. D. Winefordner, "Surface-launched acoustic wave sensors. Chemical sensing and thin-film characterization", vol. 144 in Chemical Analysis: A series of monographs on analytical chemistry and its applications, Wiley Interscience, New York, 1997.

- [107] D. W. Galipeau, P. R. Story, K. A. Vetelino and R. D. Mileham, “Surface acoustic wave microsensors and applications”, in Smart Materials Structure, Brookings, Microconversion Technologies Company, vol. 6, pp. 658-667, IOP Publishing Ltd. , SD 57006 US, 1997.

- [108] J. D. N. Cheeke, “Fundamentals and applications of ultrasonic waves”, Series: Pure and Applied Physics, vol: 3, CRC Press LLC, USA, 2002.

- [109] S. J. Martin, G. C. Frye and S.D. Senturia, “Dynamics and response of polymer coated surface acoustic wave devices: effect of viscoelastic properties and film resonance “, Anal. Chem., vol. 66, pp. 2201, 1994.

- [110] H. F. Tristan, B. K. Sinha, “A perturbation analysis of the attenuation and dispersion of surface waves”, Journal of Applied Physics, vol. 49, pp. 87, 1978.

- [111] M. Rapp, D. Binz, I. Kabbe, M. Von Schikkus, S. Hunklinger, H. Fuchs, W. Schrepp and B. Fleischmann , “A new high-frequency high-sensitivity SAW device for NO₂ gas detection in the sub-ppm range” Sensors and Actuators B: Chemical , vol.4, pp. 103-108, 1991.

- [112] E. L. Adler, J. K. Slaboszewicz, G. W. Farnell and C. K. Jen, “PC software for SAW propagation in anisotropic multilayers”, IEEE Transactions on Ultrasonics Ferroelectric and Frequency Control, vol 37, pp. 215-223, 1990.

- [113] E. L. Adler, "SAW and pseudo-SAW properties using matrix-methods", IEEE Transactions on Ultrasonics Ferroelectric and Frequency Control, vol 41, pp. 876-882, 1994.
- [114] D. A. Powell, K. Kalantar-zadeh and W. Wlodarski, "Comprehensive analysis of SAW sensor performance in liquid media by Green's function method", in Proc. of IEEE Ultrasonics Symposium, pp. 146-149, 2003.
- [115] D. A. Powell, K. Kalantar-zadeh and W. Wlodarski, "Numerical calculation of SAW sensitivity: Application to ZnO/LiTaO₃ transducers". Sensors and Actuators A: Physical, vol 115, pp 456-461, 2004.
- [116] D. A. Powell, "Modelling of layered surface acoustic wave resonators for liquid media sensing applications", Ph.D. Thesis, RMIT University, Australia, 2006.
- [117] J. F. Shackelford, W. Alexander, "CRC materials science and engineering handbook", Ed. 3, CRC Press, 2000.
- [118] T.S. Hickernell and F.S. Hickernell, "The elastic properties of PECVD silicon oxynitride films on gallium arsenide", Ultrasonics Symposium, pp. 51-54, 1991.
- [119] G. Korotcenkov, V. Brinzari, A. Cernavinski, M. Ivanov, A. Cornet, J. Morante, A. Cabot, J. Arbiol, V. Golovanov, "The role of structural factor in In₂O₃ gas response", Proceedings of IEEE Sensors, pp. 1214-1218, 2002.

- [120] G. Korotcenkov, M. Ivanov, I. Blinov and J. R. Stetter, “Kinetics of indium oxide based thin film gas sensor response: The role of redox and adsorption/desorption processes in gas sensing effects”, *Thin Solid Films*, vol. 515, pp. 3987-3996, 2007.
- [121] K. Bløtekjær, K Ingebrigsten. and H. Skeie, “Method for analysing waves in structures consisting of metal strips on dispersive media”, *IEEE Transactions on Electron Devices*, Ed. 20, no. 12, pp.1133-1138, 1973.
- [122] A. Mandelis and C. Christofides, “Physics, chemistry and technology of solid state gas sensor devices”, *Chemical Analyses*, vol. 125, 1993.
- [123] M. J. Jaycock and G. D. Parfitt, “Chemistry of Interfaces”, Ellis Harwood, Chichester, pp. 12-13, 1981.
- [124] M. E. Franke, T. J. Koplin, and U. Simon, “Metal and metal oxide nanoparticles in chemiresistors: Does the nanoscale matter?”, vol. 2, pp. 36 – 50, 2006.
- [125] Y. Min, “Properties and sensor performance of zinc oxide thin films”, Ph.D. Thesis, Massachusetts Institute of Technology , USA, 2003.
- [126] C. X. Pedersen, “Growth and characterisation of indium oxide films”, Ph.D. Thesis, University of Crete, Greece, 1998.
- [127] J. H. W. de Wit, “The high temperature behaviour of In_2O_3 ”, *J. Sol. Stat. Chem.*, vol 13, pp. 192-200, 1975.

- [128] N. Barsan and U. Wiemar, “Conduction model of metal oxide gas sensors”, *Journal of Electroceramics*, vol. 7, pp. 143–167, 2001.
- [129] M. Schweizer-Berberich, Ph.D. Thesis, University of Tübingen, Germany, 1998.
- [130] N. Yamazoe, “New approaches for improving semiconductor gas sensors”, *Sensors and Actuators B: Chemical*, vol.3, pp.7-19, 1991.
- [131] N. Yamazoe and N. Miura, “Environmental gas sensing”, *Sensors and Actuators B: Chemical*, vol. 20, pp. 95-102, 1994.
- [132] K. Galatsis, “Investigation of nanosized molybdenum oxide-titanium oxide and tungsten trioxide thin film for gas sensing”, Ph.D. thesis, RMIT University, 2002.
- [133] A. Gurlo, N. Barsan, M. Ivanoskaya, U. Weimar and W. Göpel, “ In_2O_3 and MoO_3 - In_2O_3 thin film semiconductor sensors: interaction with NO_2 and O_3 ”, *Sensors and Actuators B: Chemical*, vol 47, pp. 92-99, 1998.
- [134] S. A. Campbell, “The science and engineering of microelectronic fabrication”, Oxford University Press, New York, 2001.
- [135] D. M. Mattox, “Handbook of physical vapour deposition (PVD) processing: film formation, adhesion, surface preparation and contamination control”, Published William Andrew, ISBN 0815514220, 9780815514220, 1998.

Bibliography

- [136] Y. Hirohata, N. Shimamoto, T. Hino, T. Yaamashima and K. Yabe, "Properties of silicon nitride films prepared by magnetron sputtering", *Thin solid Films*, vol. 253, pp. 425-429, 1994.
- [137] Y. Liu, N. Jehanathan, B. Walmsley, J. Dell and M. Saunders, "Effect of oxidation on the chemical bonding structure of PECVD SiN_x thin films", *Journal of Applied Physics.*, vol.100, pp.123516-123523, 2006.
- [138] H. Hui, O. K. Tan, Y. C. Lee, M. S. Tse, J. Guo and T. White, "In situ growth of SnO_2 nanorods by plasma treatment of SnO_2 thin films", *Nanotechnology*, vol. 17, pp. 3668-3672, 2006.
- [139] M. Lewis, "The surface acoustic wave oscillator – a natural and timely development of the quartz crystal oscillator", *Proceedings of the 28th Annual Frequency Control Symposium*, pp. 304-314, 1974.
- [140] J. Chastain, J. F. Moulder, R King, "Handbook of x-ray photoelectron spectroscopy", Eden Prairie, Minn, Physical Electronics Division, Perkin-Elmer Corp., 1995.
- [141] NIST X-ray Photoelectron Spectroscopy Database, "NIST XPS principal photoelectron line result", [WWW document], URL, <http://srdata.nist.gov/xps/bind>.
- [142] A. W. C. Lin, N. R. Armstrong, T. Kuwana, *Journal of Anal. Chem.*, vol 49, pp. 1228-1233, 1977.

- [143] N. Jehanathan, B. Walmsley, Y. Liu, J. Dell, “Oxidation of PECVD thin films”, *Journal of Alloys and Compounds*, vol. 437, pp. 332-338, 2007.
- [144] D. K. Schroeder, “Semiconductor material and device characterisation”, 3rd Ed., Wiley-Interscience, New York, 2006
- [145] Y. Ohya, T. Yamamoto and T. Ban, “Equilibrium dependence of the conductivity of pure and tin-doped indium oxide on oxygen partial pressure and formation of an intrinsic defect cluster”, *Journal of the American Ceramic Society*, vol.91, pp. 240 – 245, 2008.
- [146] B. L. C. Jimenez, P. H. A Mendez, S. B. A. Paez, O. M. E. Ramirez and H. H. Rodriguez, “Production and characterization of indium oxide and indium nitride”, *Brazilian Journal of Physics*, vol. 36, no. 3B, pp. 1017-1020, 2006.
- [147] W. Siefert, “Properties of thin In_2O_3 and SnO_2 films prepared by corona spray pyrolysis and a discussion of the spray pyrolyses process”, *Thin Solid Films*, vol. 121, pp. 215-282, 1984.
- [148] L. Meng and M. P. Santos, “Structure effect on electrical properties of ITO films prepared by RF reactive magnetron sputtering”, *Thin Solid Films*, vol. 289, pp. 65-69, 1996.

- [149] Y. Xia, P. Yang, Y. Sun, Y. Wu, B. Mayers, B. Gates, Y. Yin, F. Kim and H. Yan, "One-dimensional nanostructures: synthesis, characterisation, and applications", *Advances Materials*, vol. 15, pp. 353-389, 2003
- [150] H. Hui, Y. C. Lee, O. K. Tan and M. S. Tse, "Preparation and characterization of nanocrystalline SnO₂ thin films by PECVD", *Journal of Crystal Growth*, pp. 70-74, vol. 288, 2006.
- [151] H. Hui, O. K. Tan, Y. C. Lee, T. D. Tran, M. S. Tse and X. Yan, "Semiconductor gas sensor based on tin oxide nanorods prepared by plasma-enhanced chemical vapour deposition with post plasma treatment", *Applied. Physics Letters*, vol. 87, pp. 163123-163125, 2005.
- [152] The International Centre for Diffraction Data (ICDD) database ICDD, ICDD 6-416 card, <http://www.icdd.com>.
- [153] W.P. Jakubik and M.W. Urbanczyk, "SAW hydrogen sensor with a bilayer structure based on interaction speed", *Sensors and Actuators B: Chemical*, vol. 106, pp. 602-608, 2005.
- [154] S. J. Ippolito, A. Ponzoni, K. Kalantar-zadeh, W. Wlodarski, E. Comini, G. Faglia and G. Sberveglieri, "Layered WO₃/ZnO/36° LiTaO₃ SAW gas sensor sensitive towards ethanol vapour and humidity", *Sensors and Actuators B: Chemical*, vol. 117, pp. 442-450, 2006.

- [155] S. R. Morrison, “Chemical sensors”, in Chemical Sensors, S.M. Sze, Ed. J. Wiley, New York, 1994.
- [156] M.J. Madou, S. R. Morrison, “Chemical sensing with solid state devices“, Academic Press, New York, 1989.
- [157] K. K. Makhija, A. Ray, R. M. Patel, U. B. Trivedi and H. N. Kapse, “Indium oxide thin film based ammonia gas and ethanol vapour sensor”, Bull. Mater. Sci., vol. 28, pp. 9–17, 2005
- [158] E. Comini (Editor), G. Faglia (Editor), G. Sberveglieri (Editor), “Solid State Gas Sensing”, Springer , 2009.
- [159] J. J. Caron, T. D. Kenny, L. J. LeGore, G. Libby, C. J. Freeman and J. F. Vetelino, “A surface acoustic wave nitric oxide sensor”, Proceedings of the IEEE Frequency Control Symposium, pp. 156-162, 1997.
- [160] R. Lec, J. F. Vetelino, R. S. Falconer and A Xu, “Macroscopic theory of surface acoustic wave gas microsensors”, Proceedings of the IEEE Ultrasonics Symposium, pp. 585-589, vol.581, 1988.
- [161] M. Rapp, R Stanzel, M Vonschickfus ,S. Hunklinger, H, Fuchs, W. Schrepp et al. , “Gas-detection in the ppb-range with a high-frequency, high-sensitivity surface acoustic-wave device”, Thin Solid Films, vol. 210, pp. 474-476,1992.

- [162] B. Holcroft and G. G. Roberts, "Surface acoustic-wave sensors incorporating Langmuir-Blodgett films", *Thin Solid Films*, vol. 160, pp.445-452, 1988.
- [163] W. Jakubik, M Urbanczyk and A Opilski, "Sensor properties of lead phthalocyanine in a surface acoustic wave system", *Ultrasonics*, vol. 39, pp. 227-232, 2001.
- [164] J. D. Galipeau, L. J. LeGore, K. Snow, J. J. Caron J. F. Vetelino and J. C. Andle, "The integration of a chemiresistive film overlay with a surface acoustic wave microsensor", *Sensors and Actuators B: Chemical*, vol. 35, pp. 158-163,1996.
- [165] J. A. Thiele and M Pereira da Cunha, "High temperature LGS SAW devices with Pt/WO₃ and Pd sensing films", *Proceedings of the IEEE Ultrasonics Symposium*, vol.1752, pp. 1750-1753, 2003.
- [166] K. Kalantar-zadeh, Y. X. Li, W. Wlodarski and F. Brennan, "A layered structure surface acoustic wave for oxygen sensing", *Proceedings of the Conference on Optoelectronic and Microelectronic Materials and Devices*, pp. 202-205, 2000.
- [167] K. Kalantar-zadeh, A. Trinchì, W. Wlodarski, A Holland and M. Z. Atashbar, "A novel love mode device with nanocrystalline ZnO film for gas sensing applications", *Proceedings of the IEEE Nanotechnology Conference*, pp 556-561, 2001.
- [168] S. J. Ippolito, K. Kalantar-zadeh, W. Wlodarski, K. Galatsis, W. J. Fischer , O. Berger et al., "A layered SAW based NO₂ sensor with a copper phthalocyanine

- selective layer”, Proc. of the Conference on Optoelectronic and Microelectronic Materials and Devices, pp. 165-168, 2002.
- [169] S. J. Ippolito, A. Ponzoni, K. Kalantar-zadeh, W. Wlodarski, E. Comini, G. Faglia et al., “Ethanol sensor based on layered $\text{WO}_3/\text{ZnO}/36^\circ\text{YX LiTaO}_3$ SAW Devices”, Proc. of Transducers '05, pp. 1915-1918, 2005.
- [170] S. J. Ippolito, S. Kandasamy, K. Kalantar-zadeh, A. Trinchì and W. Wlodarski, “A layered surface acoustic wave $\text{ZnO}/\text{LiTaO}_3$ structure with a WO_3 selective layer for hydrogen sensing”, Sensors Letters, vol. 1:pp.33-36, 2003
- [171] S. J. Ippolito, S. Kandasamy, K. Kalantar-zadeh, and W. Wlodarski, “Layered SAW hydrogen sensor with modified tungsten trioxide selective layer”, Sensors and Actuators: B Chemical, vol. 108, pp. 553-557, 2005.
- [172] M. Penza, M. A. Tagliente, P. Aversa, M. Re and G. Cassano, “The effect of purification of single-walled carbon nanotube bundles on the alcohol sensitivity of nanocomposite Langmuir-Blodgett films for SAW sensing applications”, Nanotechnology , vol.18, 2007.
- [173] New Cosmos Electrical Ltd. Co., “New Cosmos home page”, [WWW document] ,URL, <http://itraders.biz/cosmos/aet-030p.html>.

- [174] Y. Hongzhi, O. Lizhi and C. Wai-Yim, “Ab initio calculation of elastic constants of ceramic crystals”, *Journal of American Ceramics Society*, vol. 90, pp. 3194-4204, 2007.

- [175] G. Kovacs, M. Anhorn, H. E. Engan, G. Visintini, and C. W. Ruppel, “Improved material constants for LiNbO_3 and LiTaO_3 ”, in *Proc. IEEE Ultrasonics Symposium*, pp. 435–438, 1990.

- [176] K. Yamanouchi and M. Takeuchi, “Applications for piezoelectric leaky surface waves”, *Proceedings of the IEEE Ultrasonics Symposium*, pp. 11-18, 1990.

- [177] K. B. Pfeifer, S. J. Martin, A.J. Ricco, “Surface acoustic wave sensing of VOCs in harsh chemical environments “, Sandia report, SAN93-0070, 1993.